Investigation of Induced Seismicity in Southern Kansas

By Keith A. Nolte © 2020

M.S., Geology, The University of Kansas, 2017
B.S., Geology, The University of Kansas, 2015
B.S., Physics, The University of Kansas, 2015

Submitted to the graduate degree program in Geology and the Graduate Faculty of the University of Kansas in partial fulfillment of the requirements for the degree of Doctor of Philosophy.

Chair: George Tsoflias, PhD

Doug Walker, PhD

Mary Hill, PhD

Franciszek Hasiuk, PhD

Cornelis Van Der Veen, PhD

Tandis Bidgoli, PhD

Date Defended:
December 14, 2020

The dissertation committee for Keith A. Nolte certifies that this is the
approved version of the following dissertation:

Investigation of Induced Seismicity in Southern Kansas

Chair: George Tsoflias, PhD

Date Approved:
December 14, 2020

Abstract

The US midcontinent has experienced an unprecedented increase in seismic activity over the last decade attributed to increased wastewater injection into the Arbuckle Group, directly above the Precambrian igneous and metamorphic basement. This dissertation presents local earthquake monitoring from 2015 to 2020 at Wellington field in Sumner County, south-central Kansas, which generated a catalog of approximately 4,000 events with a magnitude of completeness of Mw 1.6. This catalog is particularly unique in that it shows the entire cycle of induced seismicity from increasing earthquake frequency to returning towards baseline. Seismicity is shown to progress northward over time, in response to a presumed northward advancing pressure front from distant large-volume wastewater injections to the south of the monitoring area. Cluster analysis on the entire earthquake catalog identified previously unknown reactivating faults trending NW and NE. Those faults align with known basement structures along the Nemaha Ridge and this work is the first direct evidence of their existence. Individual spatial earthquake clusters revealed swarm temporal behavior of induced seismicity, with earthquake activity along a fault segment lasting from several hours to a few weeks. An S to P direct converted wave was identified for the first time in local induced earthquakes and a new method was developed to employ S to P direct converted waves to constrain earthquake depth, improving accuracy of local networks. This is particularly useful in temporary networks that are established to monitor industrial activities. Novel automated shear wave anisotropy analysis codes were developed and used to evaluate very local induced earthquake shear wave splitting parameters, resulting in a deeper understanding of sources of anisotropy in south-central Kansas. This work reveals observations of temporal change in anisotropy and it examines mechanisms of how changes in pore fluid pressure can impact

anisotropy. Lastly, undertaking this research involved all aspects of local earthquake monitoring: from planning a network, to field installation, to compiling the earthquake catalog, and finally analyzing the observations. This work resulted in the development of practical guidelines for establishing and maintaining local earthquake monitoring networks. The methods and analyses presented in this dissertation advance the understanding of monitoring and evaluating induced local earthquakes.

Acknowledgements

I would like to acknowledge the mentorship and support of my advisor George Tsoflias who has mentored me since undergraduate coursework, guiding me through graduate school and encouraging me to complete this PhD. Through his help, this dissertation benefited from the collaboration with experts around the world. Without George's constant support, this dissertation would not have been possible.

I would like to thank my committee for their revisions and assistance with this dissertation. I appreciate the assistance of many dedicated undergraduate researchers throughout the course of my PhD, in particular, Zelma Molina, who has been on the project for over four years. Additionally, I want to thank my fellow graduate students for their friendship and fellowship.

My work here would not be possible without the assistance of my wife and family who have supported me through my entire academic career.

Table of Contents

Table of Figures

Chapter 1 Introduction and Background

1.1 Induced Seismicity

Induced seismicity is a problem around the world caused by a variety of anthropogenic activities, including energy resource development (hydrocarbon, geothermal), disposal of waste fluids, CO_2 sequestration, mining and the impoundment of water (Grigoli, 2017). Public fear and the risk to society from induced earthquakes poses a large challenge to industrial operations around the world, requiring advanced solutions to monitor and understand earthquakes that may be anthropogenic. While induced seismicity refers broadly to *seismic events caused by human activities*, there is a distinction between "purely induced" seismicity and "triggered" seismicity. Triggered earthquakes result from a stress change caused by human activities. Triggered earthquakes are those in which the natural tectonic stress is the primary factor, with human activities contributing only a small percentage of the change (Dahm et al., 2015). Human activities may trigger the event, but because the tectonic features are primarily responsible, these earthquakes would have likely occurred at a geologically later date. "Pure induced" are earthquakes where human activity caused the entire stress change, and the earthquake would not have occurred without this anthropogenic change. Triggered earthquakes are likely to be larger than purely induced due to the greater strain produced by tectonic stresses (Grigoli et al., 2017). Nearly all of the earthquakes that have occurred in Kansas and Oklahoma during the last decade have been triggered events. Colloquially, and throughout this dissertation, no distinction will be made between purely induced and triggered earthquakes; they will together be referred to as induced earthquakes.

While there is undisputed evidence that earthquakes can be caused by anthropogenic activity at sites like the Rocky Mountain Arsenal and Rangeley, both in Colorado (Evans, 1966; Raleigh et al., 1976), it is often difficult to link an earthquake to a particular activity. The 2012 Mw 6.0 Emilia, Italy, earthquake sequence is an example of earthquakes that occur close to industrial activities without evidence of anthropogenic induction (Cesca et al., 2013). Although this earthquake sequence occurred in a seismically active area, the magnitude and number of events in the sequence raised public speculation that as local gas extraction was responsible, despite probabilistic studies indicating that the Emilia sequence was likely not induced (Dahm et al., 2013). Even without evidence, these events strongly color public perception and necessitate a further evaluation of other sites of potentially induced earthquakes. Over 700 engineering and geological projects have been identified as potential sources of induced seismic activity (Foulger et al., 2018), although some cases are quite plausibly natural in origin (e.g., Emilia). Higher density monitoring networks and advanced analysis techniques allow researchers to answer this fundamental question concerning earthquakes near industrial zones: natural or anthropogenic (Hornbach et al., 2015).

1.1.1. Causes of Induced Seismicity

Mining operations have been linked to induced seismicity since the early 1900s (McGarr et al., 2002). Oil and gas industry-linked seismicity has been observed since the 1920s (Pratt and Johnson 1926). However, it was not until modern techniques for saltwater re-injection emerged with the advent of unconventional drilling techniques in the early 2010's that significant seismicity linked to oil and gas exploration was observed (Ellsworth, 2013; Langenbruch and Zoback 2016). Additional industrial activities associated with induced seismicity include hydraulic fracturing, geothermal energy exploitation, CO_2 sequestration, and water impoundment behind dams (Grigoli et. al, 2017). These activities share an ability to act in the shallow crust and alter the stress field, causing seismic events. Typically, there is a greater risk of such activities in porous and permeable units allowing for pore fluid pressure transfer along fault and fracture zones (Ellsworth, 2013).

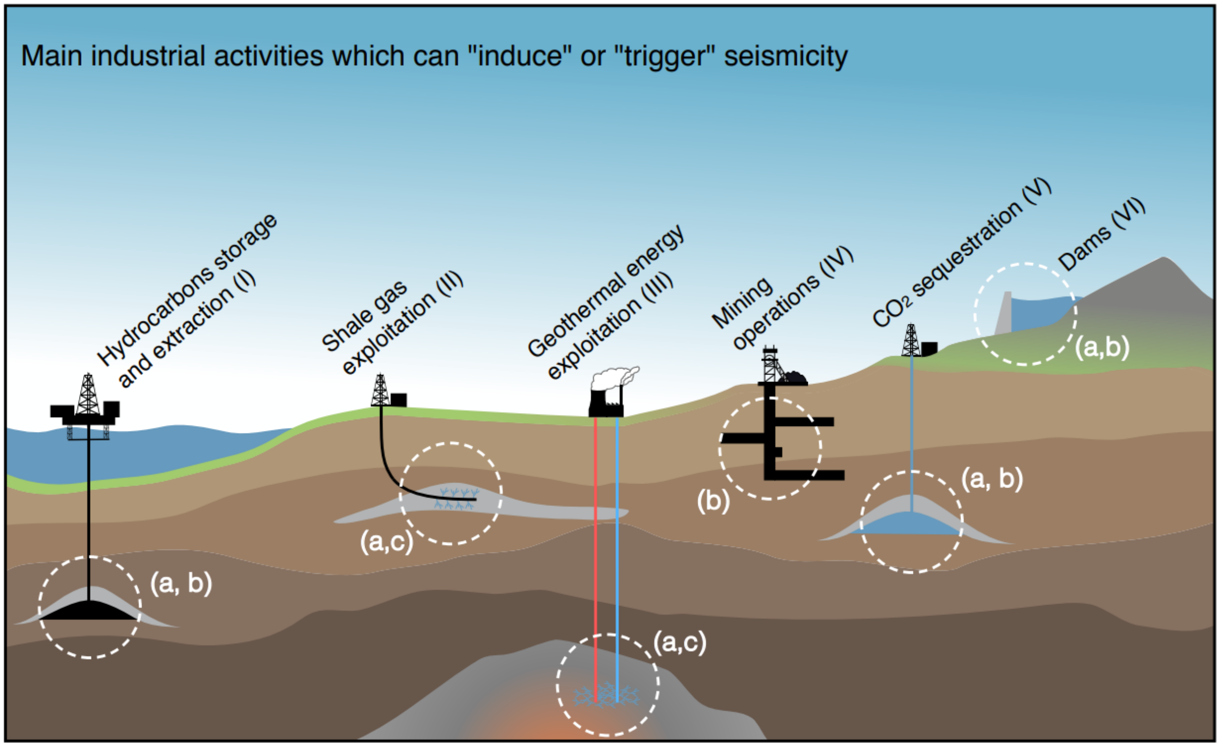

Figure 1-1: Industrial activities can "induce" or "trigger" seismicity (Grigol et. ali, 2017).
In parenthesis are mechanisms of induced seismicity for each activity. Mechanism a is increased pore fluid pressure on the fault, mechanism b is change in mass or volume above the fault, and mechanism c is hydraulic fracturing of the rock.

The Rocky Mountain Arsenal, a ~15,000-acre wildlife refuge north of Denver, previously a chemical weapons facility which is the source of the waste, is the earliest and most well-documented case of induced seismicity (Evans, 1966). As part of a program to remove hazardous waste, deep chemical injections were done, triggering a swarm of earthquakes between 1962 and 1967, culminating in a MW 4.1 earthquake in 1967. Earthquakes continued for ~18 months after injections ended; the rate and size of earthquakes was closely correlated to injection timing and volumes (Evans, 1966).

Based on the earthquakes at the Rocky Mountain Arsenal, many groups hypothesized that changes in pore pressure due to the fluid injection triggered the seismic events. At Rangeley, Colorado, fluid was intentionally injected to cause earthquakes, confirming this hypothesis (Raleigh, 1976). Since then, many studies have supported that changes in pore fluid pressure, often from wastewater injection, can trigger seismic activity.

The understanding of induced seismicity is strongly affected by its proximity to people and, therefore, public interest (Wendel 2016). As induced seismicity has occurred in more populated areas, public interest has grown and scientists have increased monitoring of microseismic events (M<2, colloquially earthquakes that aren't felt), often creating extensive catalogs with a significantly lower magnitude of completeness than previously available. This has led to the development of many automatic, real-time data analysis procedures (Cesca and Grigoli 2015; Skoumal, Brudzinski, and Currie 2015). Unfortunately, different protocols often give significantly different results, leading to difficulty in interpreting data and comparing with other studies (Cesca et al., 2014).

The number of felt earthquakes across the US Midcontinent has risen significantly since 2010 (Ellsworth, 2013; Rubinstein et al., 2018). In particular, felt earthquakes near population centers have captured national attention in the public and academic sphere. Academic interest began increasing significantly after the 2011 Central Oklahoma Earthquake, a M5.7 earthquake (Ellsworth, 2013). Public anxiety about induced earthquakes was exacerbated by early lack of information on the earthquakes, especially in the media. The tie between these felt earthquakes and national interest is clear in internet search terms analytics; after felt events near populations centers, searches for terms like “fracking earthquakes” and “drilling” can increase by orders of magnitude (Grigoli et al., 2017).

1.2 Geological Background

1.2.1. U.S. Midcontinent

The US Great Plains is a geomorphic region that consists of much of the colloquial "Midwestern" United States, from the Dakotas to northern Texas. The Canadian Shield forms the bulk of the continent’s substructure. The Canadian Shield is formed of Precambrian igneous and metamorphic rock and is the oldest known rock mass in the North American continent. Much of the geological features of this region were formed through the welding of multiple small continents during the Precambrian (Whitmeyer and Karlstrom 2007). These igneous and metamorphic Precambrian rocks comprise the geologic "basement" of the US Midcontinent.

On average, the North American plate is 36.7 km thick, growing thicker at the Midcontinent Rift, under the Great Plains, to 40 km (Chulick and Mooney, 2002). There is little to no deep seismic activity in the Midcontinent, given its intraplate setting. Most research in the region is constrained to the shallow sedimentary units (upper ~1.5 km) for energy resources development, and recently to the upper granitic basement (~1.5-5 km) due to the occurrence of seismicity at these depths. In the Midcontinent, the Arbuckle Group, the primary geologic unit used for disposal of wastewater in Kansas and Oklahoma, is in many places in direct contact with the basement, and it is believed to be in fluid communication with the basement through faults and fracture zones (Keranen, 2014). Because of this fluid connection, increases in fluid pressure in the Arbuckle can cause increased pore fluid pressure within the fractured granitic basement, resulting in reactivation of critically stressed fault systems that are near failure.

Many faults in the Midcontinent are remnants of the failed Midcontinental Rift system which extends hundreds of kilometers from the Great Lakes region into eastern Kansas. (Baars, 1995).

1.2.2. Kansas

Structurally, less is known about the subsurface features of Kansas compared with surrounding states due to the patterns of drilling and completion of petroleum wells, which have targeted shallower intervals. Due to the early development of Kansas oil production, the log information available was often not collected using modern methods or suitable for modern evaluation (Franseen et al., 2004).

Stratigraphic mapping of Kansas has been done primarily through electric and radioactivity logs as well as outcrop correlation to the subsurface (Jewett and Merriam, 1959). The sedimentary strata of Kansas are relatively thin when compared regionally, reaching their deepest at the Hugoton Embayment in SW Kansas at 9,500 feet (~2.9 km). The thin, multilayered appearance of the sediments has been compared to a layer cake, and the dip does not exceed 10° (Jewett and Merriam, 1959).

The Cenozoic layers, built from thin deposits of sand, gravel, silt, clay, and ash, are valuable to the Kansas economy due to groundwater production. Alluvial fill is ~80 feet deep due to glacial deposits in northeastern Kansas (Merriam, 1954).

Mesozoic rocks underlay the Cenozoic layers. In the early 20th century, considerable interest was paid to the possible commercial resources in these layers, including coal (Survey and Schoewe 1952), oil (Runnels et al., 1952), glass sand (Nixon, Runnels, and Kulstad, 1950), and chalk (Runnels and Dubins, 1949). However, clay is the only mineral extensively produced (Plummer and Romary, 1947). Most Mesozoic rocks in Kansas are marine deposits that include shale, sandstone, and limestone. Many of these are limited to Western Kansas due to erosion.

Paleozoic rocks have been extensively studied in comparison to other structures in Kansas because of the extensive oil and gas plays discovered in the past century. Beyond oil, Paleozoic rocks are large producers of groundwater (Hilpman and Inves, 1958). In southeastern Kansas, lead and zinc deposits were extensively produced. From 1850 to 1950, 10% of all of the lead produced in the United States came from this region (Sawin, 2001).

Paleozoic rocks in Kansas included the Permian, Pennsylvanian, Mississippian, Devonian, Silurian, Ordovician, and Cambrian Systems. Permian rocks, which exist only in the western four-fifths of the state, and Pennsylvanian rocks, which cover the state, are composed of marine and non-marine deposits in thin, alternating layers. The Permian contains four series, three of which are present in Kansas (Moore, 1951) containing shale, siltstone, and sandstone. The Pennsylvanian is composed of five series (Moore, 1949). Mississippian layers of Silurian and Denovian age are present only in the northeast regions of Kansas and are thinner than other layers. The Cambrian and Ordovician rocks make up the base layer of the Paleozoic rocks and nonconformably overlie Precambrian rocks throughout the state.

The Lansing Group (Missourian series) comprises limestone and black radioactive shale in alternating beds. The limestone beds can be components of the petroleum system (Harbaugh, 1959), making them important units for the oil industry (Moore, 1929).

The Lansing group sits conformably on the Kansas City group, which has 27 units spanning ~350 feet (~110m) alternating between marine and non-marine units. Like the Lansing, the Kansas City layer is important for oil production (Parkhurst, 1959; Moore, 1929). In eastern Kansas, the Mississippian group is of particular economic value for oil, lead, and zinc deposits (Lee, 1940).

The Cambrian-Ordovician units consist of dolomite with limestone, sandstone, and shale interspersed. The Arbuckle Group, the largest group, is composed of Late Cambrian rocks with a total thickness of approximately 1,500 feet in some areas (~450m). The Arbuckle is absent from the Nemaha Ridge, Central Kansas Uplift, and Cambridge Arch at the higher points in the structures (Watney, 1980). The Simpson Group unconformably overlies the Arbuckle Group at a thickness of 10-84 feet (3-25m) (Leatherock, 1945). The Arbuckle Group is composed of five units from the Late Cambrian and Early Ordovician (Lee and Merriam, 1954).

Precambrian rocks compose the basement in Kansas. Four thousand wells have penetrated the basement rock, giving data on its composition despite the lack of exposure. The basement is 600 feet at its shallowest over the Nemaha Ridge in NE Kansas and 9,500 feet at its deepest in the Hugoton Embayment in SW Kansas. Igneous, primarily granite, with some metamorphic rocks, primarily quartzite and schist, are the main lithologies present in the basement (Merriam, Cole, and Hambleton, 1961).

The Paleozoic stratigraphy of Kansas is easy to seismically model through 1-dimenisonal velocity models due to the simple layered formations. Alternating layers of marine limestones and shales are the predominant features (Merriam, 1963; Johnson, 2008)

1.2.3. The Wellington oil Field

Wellington, Kansas, is located in Sumner County in south-central Kansas. In Wellington, the key units are the Mississippian, the main unit of oil production, the Arbuckle, the main unit in the region for local wastewater disposal, and the granitic basement, where earthquakes have occurred.

Wellington, Kansas, is located at the southern tip of the Midcontinent Rift, east of the Nemaha uplift. These features control the primary geology of the region. Wrench fault zones borne of the Midcontintent Rift created fault blocks in Sumner County (Baars, 1995) in the Precambrian, granitic basement (Baars, 1995; Johnson, 2008),

1.3 Induced Seismicity in Kansas and Oklahoma

An average of 21 earthquakes per year were M>3 in Oklahoma from 1967 to 2000. In Kansas, from 1977 to 2012, 197 earthquakes were recorded, with only 15 being larger than an M3. However, seismicity has increased drastically in the region, with 300 M > 3 earthquakes between 2010 and 2012 (Ellsworth, 2013) in Oklahoma. In 2015, more than 900 M > 3 earthquakes were recorded in Oklahoma. The largest earthquake recorded in Kansas, M4.9, occurred in 2014 near Milan in Sumner County (Choy et al., 2016).

Water cuts in Oklahoma plays can be as high as 90% across the region, resulting in a higher volume of saltwater disposal (SWD). In Harper and Sumner County KS, SWD well counts have tripled since 2005. The injection was at its highest point from July 2014 to December 2014, before new rules from the Kansas Corporation Commission (KCC), the oil and gas regulatory agency in Kansas, that reduced injections on March 29, 2015 (Rubinstein, Ellsworth, and Dougherty, 2018b). Injection volumes through Oklahoma and southern Kansas correlate closely to the overall seismicity rate (Langenbruch et al., 2018).

Induced seismicity in Oklahoma came to the forefront of public awareness after a large M 5.6/5.7 earthquake in 2011 occurred near Prague, Oklahoma (Keranen et al., 2013; Keranen et al., 2014). By analyzing search trends over time, Grigoli et al. (2017) demonstrated that public interest in induced seismicity quadrupled in the days following the event (Choi, 2014, Grigoli, 2017). The M_w 5.1 Fairview earthquake in February 2016, followed by the M_w 5.8 Pawnee earthquake in 2016, caused additional public interest. This led to the Oklahoma Corporation Commission, reducing industrial injections by 40% (Langenbruch and Zoback, 2016).

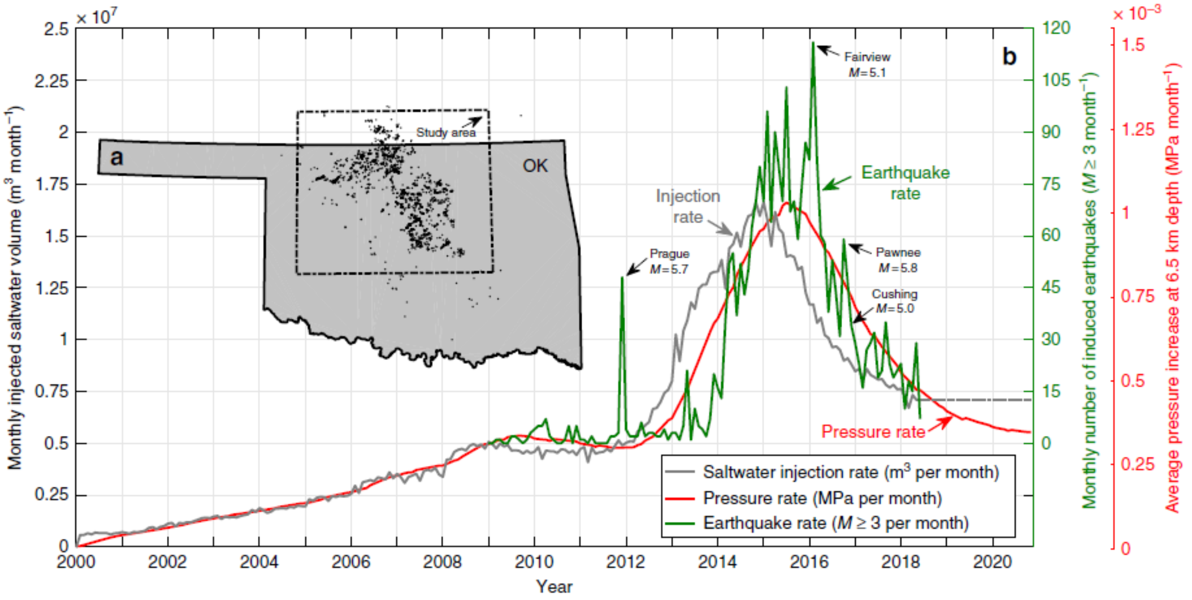

Figure 1-2: In central/northern Oklahoma and southern Kansas injection rate (grey curve) and modeled pressure rate (red) tie to seismicity rate (green) (from Langenbruch et al., 2018).

Monitoring networks in the region indicate that seismic activity peaked in 2015 with 947 events M > 3 in Oklahoma and Kansas (USGS NEIC). While a majority of the research and public focus has been on Harper and Sumner County in southern Kansas, where earthquake rates are currently becoming less frequent, large events are still occurring, including an M4.5 on January 19, 2020, near Hutchison, Kansas, and an M4.6 west of Plainsville in north-central Kansas on June 22, 2019 (USGS NEIC). These earthquakes may not be related to activity in southern Kansas, but currently lack a causal mechanism.

1.4 CO_2 Sequestration in Wellington, Kansas

The Kansas Geological Survey (KGS), Berexco, and partners, pursued a pilot CO_2 sequestration project at Wellington oil field with funding from the Department of Energy (DOE) (DE-FE00006821). The field site had been in production since 1929, producing over 20 million barrels of oil. The goal of the project was to monitor, verify, and account, via *in situ* and indirect means, for changes due to CO_2 injected in the Mississippian reservoir for enhanced oil recovery. Coring, wireline logs, well tests, 2D seismic surveys, and a 3D seismic survey were conducted to understand the Mississippian reservoir and Arbuckle saline aquifer. The CO_2 plume was monitored and estimates of CO_2 leakage were calculated.

Approximately 20,000 metric tonnes of CO_2 were injected into the Mississippian carbonate reservoir resulting in an average of 68% increased oil production with no to minimal CO_2 leakage, but 18% CO_2 produced back. This study provided a strong case for the safe storage of CO_2 in a deep carbonate reservoir in Kansas (Holubnyak et al., 2017).

1.5 Establishment of a Seismic Network in the Wellington oil Field

The Wellington Seismic Monitoring Network was established in conjunction with the DOE CO_2 monitoring project, and produced a majority of the earthquake data presented herein. The Wellington Network (IRIS network code ZA) consists of 15 Sercel L-22 three-component short-period seismometers, along with three Nanometrics Trillium Compact Posthole Seismometers which were utilized intermittently for additional data. The Wellington Network has recorded continuously since May of 2015 and it has detected approximately 4000 earthquakes in Sumner County and southern KS. Instrumentation has been regularly relocated to provide a better assessment of earthquake activity in Sumner County. The original station locations were all within the Wellington oil field. This seismometer network is now inside Sumner County, except for two stations, but some stations of the USGS temporary network (GS) and one station of the USGS NetQuakes array (NQ), in southern Kansas (Rubinstein, Ellsworth, and Dougherty 2018a), available through IRIS, were used to supplement the Wellington Network (Figure 1.3).

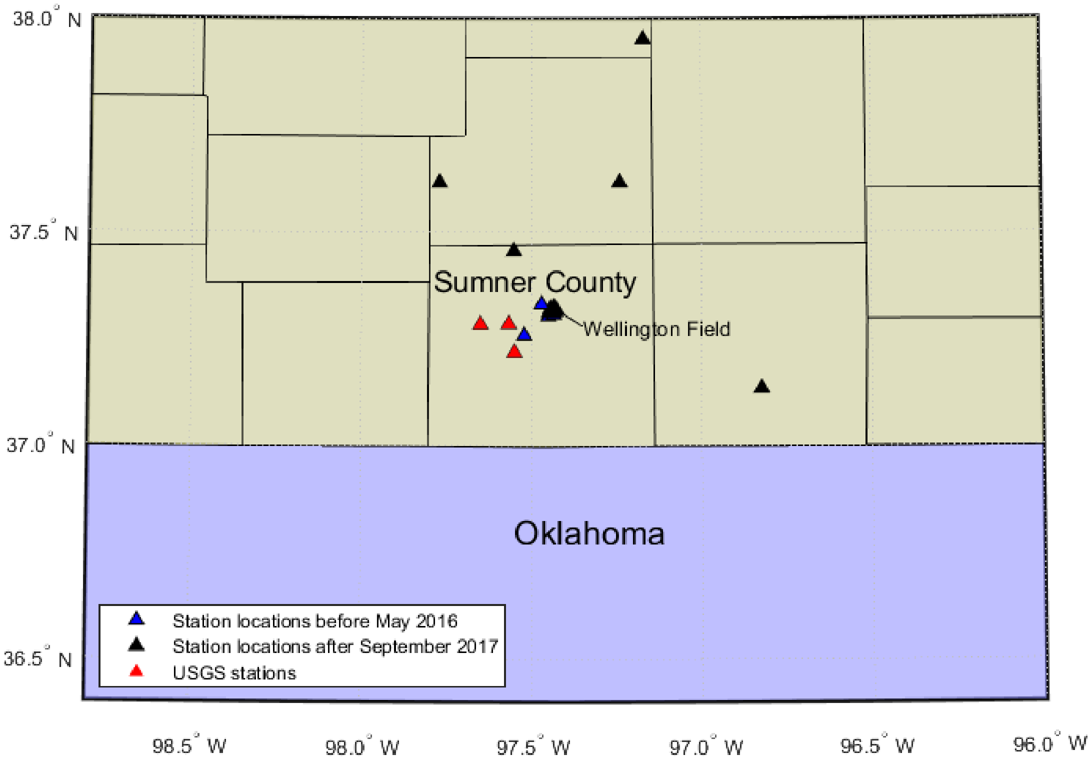

Figure 1-3: Map of seismometer stations in the Wellington Earthquake Monitoring Network and the location of Wellington field.

1.6 Dissertation Outline

The dissertation presents ~6 years of detailed earthquake monitoring from the Wellington network in Sumner County, KS. From the peak of seismicity in 2015-2017 to present when activity has declined. The dissertation consists of six chapters. The first chapter, the introduction, provides background on induced seismicity historically and in the U.S. Midcontinent. Chapters 2-5 are the main body of research regarding induced seismicity in Kansas, followed by chapter 6, a discussion, and future directions. Chapter 2 presents the Wellington Earthquake Catalog from 2015-2020. This catalog is used to identify previously unknown faults as well as earthquake migration northward into Kansas. It shows the full cycle of seismicity, before the peak in 2017 to the decline in earthquake rate through 2020. It provides the catalog information that is part of all other chapters as well. Chapter 3 is an investigation into an additional waveform arrival that is determined to be an S to P direct converted wave. A new method is presented that takes advantage of this additional arrival to better constrain earthquake depth and prove earthquakes are not occurring in the sedimentary section as well as provide additional insight into the Vp/Vs ratio in the sedimentary section. Chapter 4 is a detailed analysis of Shear-wave anisotropy in very local earthquakes using an automated methodology. This analysis shows temporal changes in shear-wave splitting parameters that correlate with pore fluid pressure change. Chapter 5 provides insights on designing and operating a temporary local earthquake monitoring network with a case study in western Kansas.

This work presents a novel catalog of earthquakes for analysis and identifies previously unknown faults in south-central Kansas. This catalog is particularly unique in that it shows the entire cycle of induced seismicity from increasing earthquakes to return towards baseline. This is the first time an S to P direct converted wave has been identified in local earthquakes. The identification of S to P direct converted waves has enabled the use of novel location mechanisms, used here to constrain earthquakes to the shallow basement. Novel automated shear wave anisotropy analysis codes were developed and used to evaluate very local induced earthquake shear wave splitting parameters, resulting in a deeper understanding of sources of anisotropy in south-central Kansas. This work reveals observations of temporal change in anisotropy and it examines mechanisms on how changes in pore fluid pressure can impact anisotropy. The code used here was written by the author as is the first code that can directly access Seisan data, enabling novel automated processes with reduced work hours.

Chapters 2-5 have been prepared for submission to peer reviewed scientific journals and are included in the dissertation in publication format.

Chapter 2 Observations of induced seismicity in southern Kansas and identification of reactivated faults

2.1 Abstract

The US midcontinent has experienced an unprecedented increase in seismic activity over the last decade attributed to increased wastewater injection into the Arbuckle carbonate saline aquifer, directly above the granitic basement. We present local earthquake monitoring from 2015 to 2020 at Wellington field in Sumner County, south-central Kansas, USA. Despite the absence of nearby large volume injection wells, the Wellington Seismic Network has identified over 3,800 local earthquakes ranging in magnitude from 0.4 to 3.6 at depths of 1 to 12 km. Earthquakes occur in spatial-temporal swarms over time scales of a few hours to weeks. Individual swarms do not exhibit consistent earthquake sequence patterns in time of occurrence, depth or magnitude. These earthquakes have delineated previously unknown faults, with the seismicity being the first data on these reactivated faults in the upper basement. This seismicity has progressively occurred further north, away from distant large injection wells to the south and southwest of the site, indicating a changing regional pore fluid pressure regime. This study presents a detailed account of the spatiotemporal behavior of local seismicity in Sumner County, Kansas, and offers insight to far-field effects of fluid injections in the region.

2.2 Introduction

High rates of seismicity have been common occurrence in Kansas and Oklahoma over the last decade. The increased seismicity is caused by massive increases in wastewater injection (Ellsworth, 2013; Ellsworth et al., 2015; Nolte et al., 2017). In Kansas and Oklahoma, injection occurs primarily in the Arbuckle Group, which sits directly above the Precambrian basement (Franseen, et al., 2004). Recent studies suggest that the Arbuckle is in fluid communication with the fracture network in the basement (Keranen, et al., 2013;

Keranen, et al., 2014) and that basement faults penetrate up into the Arbuckle, (Schwab, et al., 2017). Pre-existing, critically stressed faults can be reactivated by small changes in pore fluid pressure at depth (Hornbach, et al., 2015; Keranen et al., 2013). However, very little is known about the reactivating basement faults in southern Kansas (Baars, 1995).

The ancient fault systems in Kansas are better understood in the northern parts of the state, where they outcrop or are near enough to the surface that some information can be gained from oil and gas exploration data (Merriam, 1956). However, in Sumner County, these basement fault systems are below the ~1.5 km thick sedimentary section and are mostly unknown (Schwab, et al., 2017; Franseen, et al., 2004).

Historically, Kansas has been seismologically inactive due to its stable formation (Merriam, 1956). From 1867 – 1972, 41 earthquakes were felt across the entire state (DuBois and Wilson, 1978). From 1973 – 2012, 29 earthquakes were detected by the USGS Advanced National Seismic System Comprehensive Catalog, 15 of these were M > 3 (Rubinstein, 2018). Most seismic activity in Kansas has historically taken place on the Nemaha ridge/Humboldt fault zone, along the midcontinent geophysical anomaly (Hildebrand et al., 1988).

Sumner County, KS, sits at the southern end of the Midcontinent Rift System (MRS), as well as the Nemaha Ridge and Humboldt Fault Zone (Lee and Merriam, 1954; Merriam, 1963; Baars, 1995). These combine to create a system of conjugate north-northeast and northwest-trending wrench faults (Lee and Merriam, 1954; Baars, 1995). Gravity and magnetic data analyses support the presence of such basement fault lineaments in northern Oklahoma and southern Kansas (Elebiju et al., 2011). The MRS is a continental scale feature and can be identified for hundreds of kilometers, but the smaller faults within it are relatively unknown. The major tectonic features have been shown to have a significant impact on the stratigraphy of Kansas, through previous episodes of reactivation (Baars and Watney, 1991), making it very likely they could reactivate once again. With the migration of earthquakes into Kansas, understanding the orientations and relative locations of these fault systems could play a significant role in assessing induced earthquake hazard risk.

2.2 Wellington Earthquake Catalog

The Wellington Seismic Network (IRIS network code ZA) was established in spring of 2015 as seismicity started increasing in southern Kansas. The seismic network has recorded data continuously from May of 2015 and it continues as of October 2020. It consists of 15 Sercel L-22 three-component short-period seismometers, recording at 200 samples per second, along with three Nanometrics Trillium Compact Posthole Seismometers that record at 250 samples per second. Instrumentation has been relocated over the monitoring period to provide a better assessment of earthquake activity in Sumner County. The original station locations were within the Wellington oil field. This seismometer network is mostly inside Sumner County, but some stations of the USGS temporary Network (GS) and one station of the USGS NetQuakes Network (NQ), in southern Kansas (IRIS, Rubinstein, et al., 2018), available through IRIS, are used to supplement the Wellington Network (Figure 2.1). Data are telemetered in real-time to the Kansas Geological Survey at the University of Kansas and are available through the IRIS data repository.

Earthquake compressional wave (P-wave) and shear-wave (S-wave) arrivals are manually identified in all the available data in SeisAn (Ottemoller et al., 2016). This waveform arrival information is then used in HypoInverse (Klein, 2014) to calculate a location for the earthquake. Efforts were made to relocate earthquakes using HYPPODD (Waldhauser, 2001), but the station geometry created unrealistic relocations. Earthquake moment magnitude (M_w) is calculated in

SeisAn from the corner frequency of a Brune Spectrum model (Brune, 1970) fit to the earthquake spectrum.

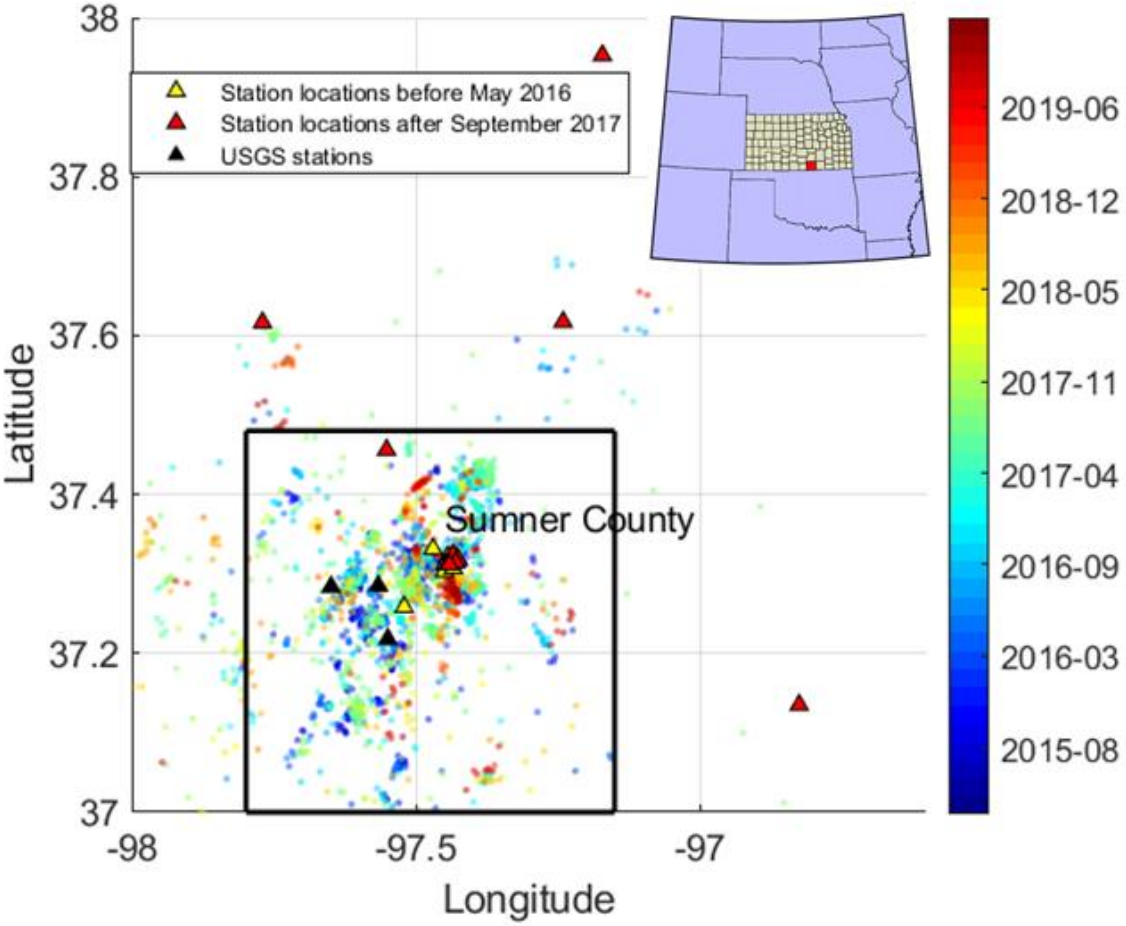

Figure 2-1: Station and earthquake locations color coded by time of occurrence.
Sumner County is outlined in black and shown as red square in the US map insert. The Wellington Earthquake Catalog contains 3,868 earthquakes in southern Kansas and Northern.

The Wellington Earthquake catalog contains 3,452 earthquakes in Sumner County from May 2015 through July 2020. Earthquake locations in and around Sumner County within approximately 40 km from Wellington field are shown in Figure 2.1. In Sumner County earthquakes range in magnitude from 0.4 to 3.7. They have a depth range of 1 to 18 km with 92% of all earthquakes estimated with HypoInverse to occur between 1 and 12 km in depth. The catalog has a magnitude of completeness of 1.6 Mw in Sumner County with a b-value of 1.1 (Figure 2.2).

The Wellington network captured the onset of increased local seismic activity in 2015 detecting 855 earthquakes over the first eight months. It detected 979 events in 2016, 1027 events in 2017, 300 events in 2018, 182 events in 2019 and 117 over 7 months in 2020, in Sumner County (Figure 2.3). The observed earthquake activity in Sumner County shows an increasing trend through the middle of 2017 followed by a sharp decline in late 2017, early 2018. Seismicity decline in northern Oklahoma and southern Kansas started in 2016 (Figure 1.2) and it is attributed to regional injection rate declines after reaching a peak in 2015 (Langenbruch et al., 2018). The same regional injection rate decline appears to have influenced the Wellington network seismicity approximately one year later than northern Oklahoma, where the maximum earthquake rate occurs in 2016. This could be due to a lag in pressure effects as Sumner County is at the edge of the modeled region in Langenbruch et al. (2018) or a difference in detection threshold.

2.3 Fault Identification from Earthquake Clusters

Clusters of earthquakes were identified using the algorithm DBSCAN (Kalami Heris, 2015) to look for tightly grouped earthquakes in space. DBSCAN identifies clusters using a radius and a minimum number of connecting points that are within the radius.

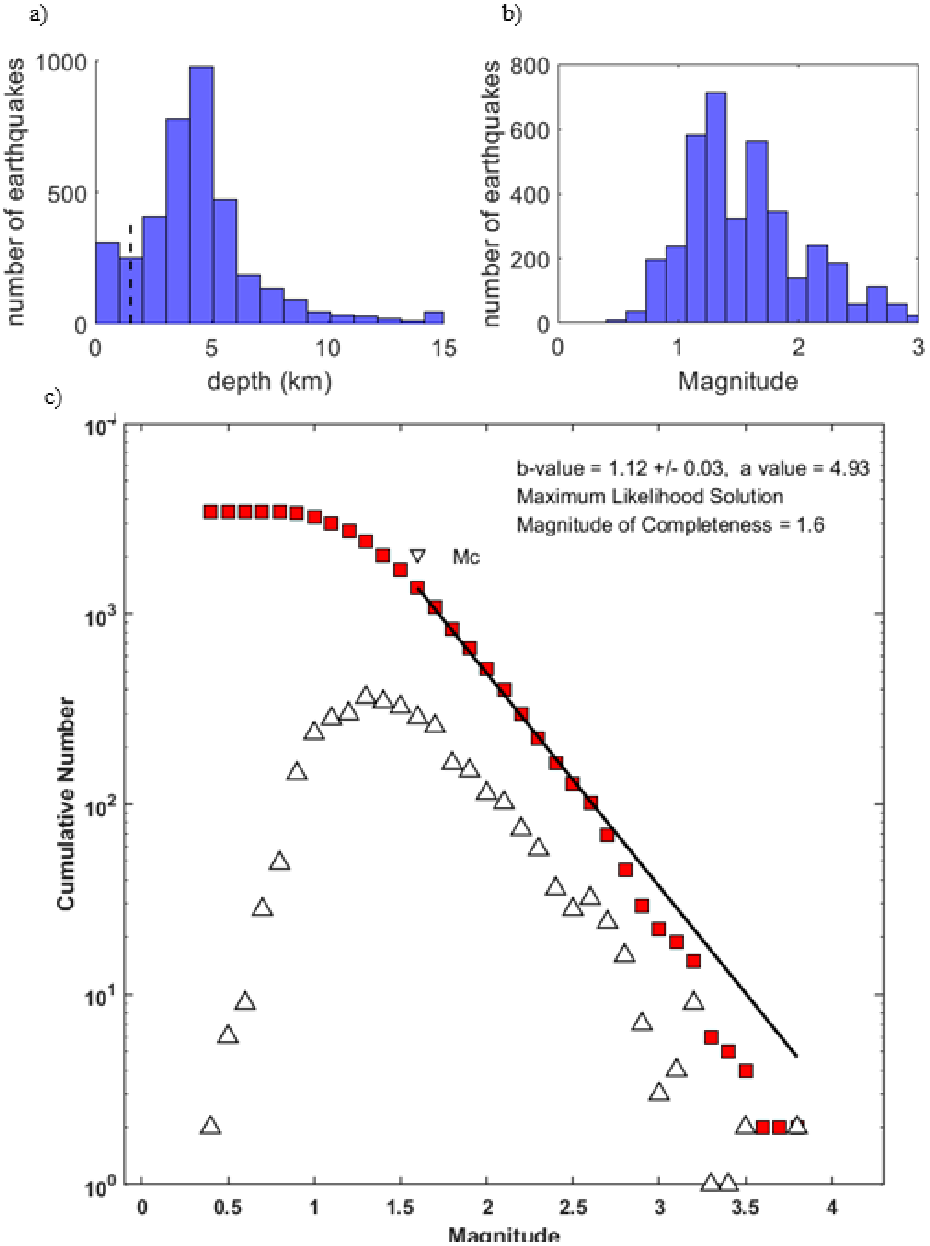

Figure 2-2: Earthquakes by depth and magnitude.

(a) Histogram of depth of earthquakes in Sumner County. Dashed line marks the depth to basement at 1.55 km. b) Histogram of magnitudes for earthquakes in Sumner County, Kansas. (c) Chart showing the Magnitude of Completeness of the earthquake catalog (modified from GISMO). The magnitude of completeness for Sumner County is 1.6 at p95. White triangles show number of earthquakes of a given magnitude, red squares show cumulative number of earthquakes of a given magnitude or larger. The line shows the fit of the b value and the Magnitude of Completeness is marked at the end of the line.

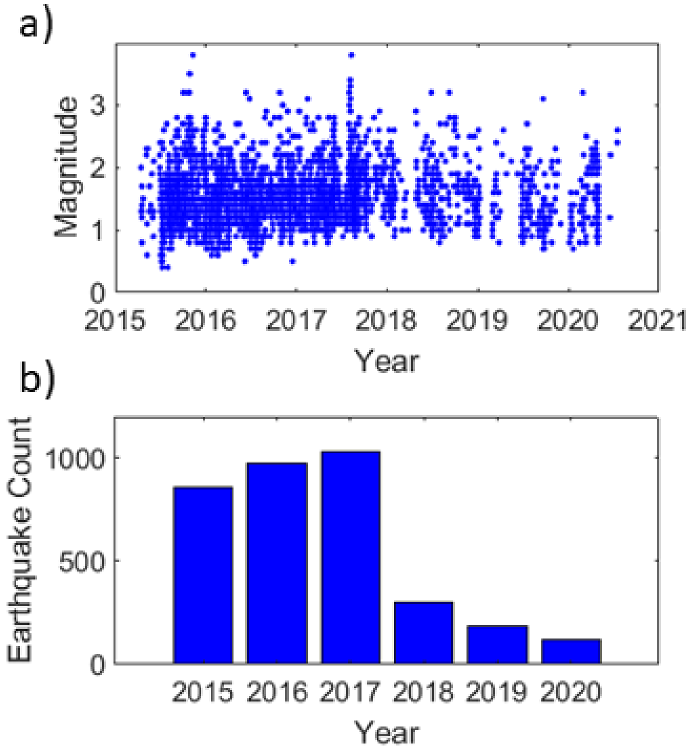

Figure 2-3: Earthquakes by magnitude.
a) Plot of earthquake magnitude vs time in Sumner County, Kansas, from May 2015 through July 2020. b) Histogram number of earthquakes per year.

The algorithm searched for earthquakes within 400m of each other and a minimum of 10 connecting points. This analysis was performed on all earthquakes in Sumner County. Near the monitoring stations, a radius of 300m was used due to the higher density of low magnitude earthquakes detected. Using this algorithm, 37 clusters of earthquakes satisfied these requirements. Clusters ranged in size from 600 earthquakes to 10 earthquakes, with 75% of earthquakes placed in clusters (Figure 2.4a). Faults through the clusters can be inferred by using the ratio of eigenvalues of the cluster for linear clusters (Schoenball and Ellsworth, 2017).

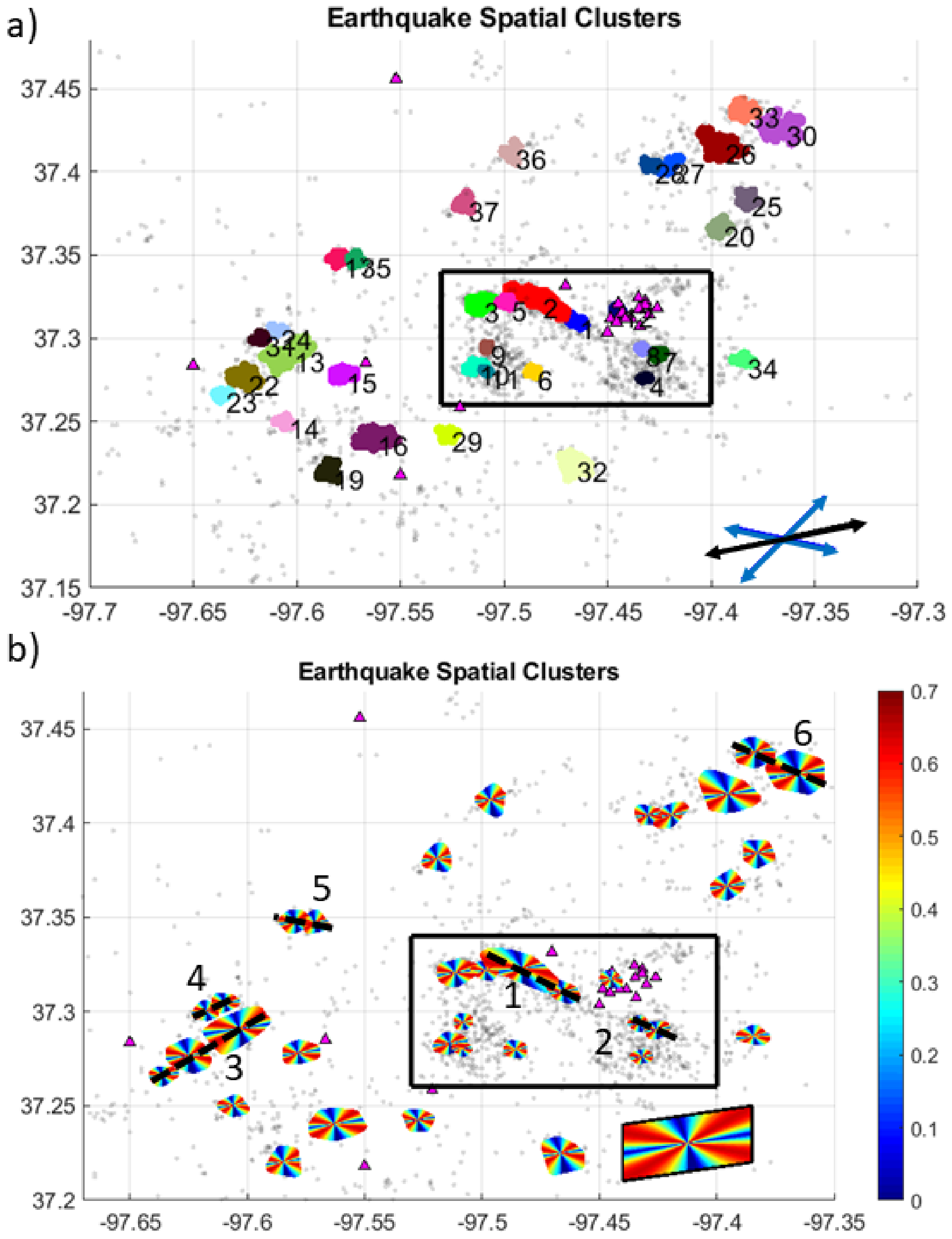

Figure 2-4: Earthquake clusters.

a) Map of central Sumner County showing the 37 earthquake clusters identified by DBSCAN spatial clustering with epsilon 400m and a minimum of 10 connecting points. Within the black box epsilon of 300m with 10 connecting points were used due to the greater number of low magnitude earthquakes being detected near the dense part of the network. Station locations are shown as pink triangles. b) The orientation of the maximum horizontal stress calculated from borehole breakouts in the Wellington Field of 77° is used to calculate the slip potential at each cluster. Six possible faults, numbered and shown by dashed lines, are inferred by the alignment of clusters and slip potential

Although many clusters identified by the seismic activity are short, they are longer than the location uncertainty, allowing their determination with some confidence. However, the cluster length is likely not representative of the activated fault length due to the poor geometry of the network. To increase the confidence in the identification of these faults, information from the known stress regime in this region was added to the analysis. Utilizing the borehole constrained orientation of the stress regime in the region (Alt and Zoback, 2017; Schwab et al., 2017) and using Andersonian fault theory (Anderson, 1951) helps constrain the potential orientation of the reactivating faults; faults that are slipping will orient closely with the expected orientation of failure. The maximum horizontal stress direction has been well-constrained both in Oklahoma (Alt and Zoback, 2017) and Kansas (Schwab et al., 2017). All sources suggest a maximum horizontal stress direction between 70° and 90° throughout the region. We use 77° as an estimate of the average horizontal stress direction in southern Kansas, according to Schwab et al., (2017). Here we use the average stress magnitudes at 5 km depth of maximum stress of 201 MPa, vertical stress of 155.3 MPa, and minimum stress of 103 MPa (Schwab et al., 2017). Schwab et al., (2017) estimate that basement faults located at 5 km depth are in failure equilibrium, so faults can be at slight angles to the optimal failure orientation and still be re-activated due to the anthropogenic increase in pore fluid pressure. Using this information, we can estimate likely fault orientations in the clusters and combine clusters with matching trends into larger faults. Figure 2.4b plots the potential for slip of each cluster and six possible faults inferred by the alignment of clusters and slip potential.

In our catalog, two faults are very clear using this technique. Fault 1 (Figure 2.4b) trending NW-SE and fault 3 (Figure 2.4b) trending NE-SW. The reactivated sections of faults identified here are 2-10 km long;

these faults would be classified as small faults along the Nemaha Ridge. Very little is known about specific faulting along this ridge, particularly at the resolution seen here. Based on projections of how the earthquake clusters connect, some faults identified here may continue for up to 20 km. These faults are in very similar orientations to the expected orientations of basement structures (Lee and Merriam, 1954; Baars, 1995; Elebiju et al., 2011).

2.4 Spatiotemporal Earthquake Migration

The Wellington Network earthquake catalog contains nearly five and a half years of local seismicity data. Earthquake occurrence has evolved over time. It is hypothesized that earthquakes in Kansas are caused by a combination of far-field pressure effects from larger rate injections in northern Oklahoma and southern Kansas, and local injections (Rubinstein et al., 2018). The lack of large-scale injections near the observed seismicity provides evidence to far field effects (10s of kms), in line with observations from Peterie et al., (2018). Sumner county has limited injection as compared to Harper County (Rubinstein et al., 2018) and Oklahoma (Langenbruch et al., 2018)).

Spatiotemporal analysis of earthquakes is done on events $M \geq 2$, as the Magnitude of Completeness of the catalog for Sumner County is 1.6, ensuring that there is very little chance the locations of M2+ earthquakes are an artifact of the ability of the network to detect the events. In 2015, 59% of earthquakes M2+ occurred within 20 km of the Oklahoma border, with only 1% occurring 45 km north from the Kansas/Oklahoma border. In 2016, only 21% of earthquakes M2+ were identified within 20 km of the Kansas/Oklahoma border, with 15% occurring 45 km north. By 2017, 20% of events M2+occurred more than 45 km from the border (Figure 2.5). After 2017, the rate of M2+ earthquakes decreased significantly, but earthquakes continued to occur in Sumner County at all latitudes. Not only have these larger earthquakes moved further north over time, but the total number of them had nearly tripled from 2015 (88) to 2017 (245).

However, since 2017 the rate of earthquakes has declined in the region presumably due to reduced industrial activities and fluid injection rates (Langenbruch et al., 2018; USGS NEIC).

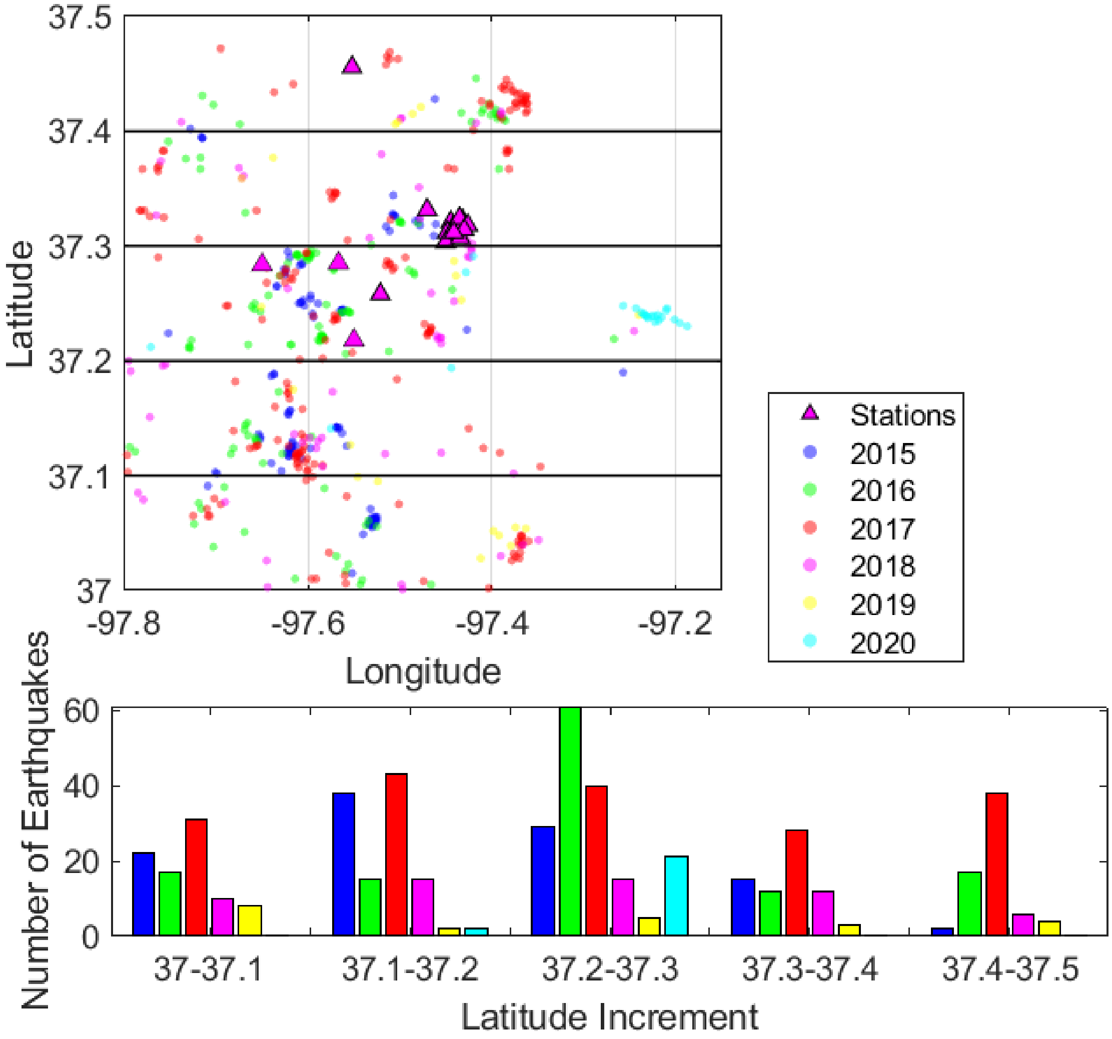

Figure 2-5: Earthquake M2 or greater.
a) Map of Sumner County showing earthquakes M2 or greater. Earthquakes are shown as circles color coded by year.
b) Graph showing the number of M2 or greater earthquakes color coded by year occurring in each increment of latitude, starting at 37 and moving north, shown in the map view.

The northward movement of these earthquakes over time suggests a northward advancing pore pressure mediated reactivation of faults along the Nemaha Ridge, which runs approximately North-

Northeast/South-Southwest. In this study, we have identified a cluster of faults activating approximately 45 km from the Oklahoma border. The Nemaha Ridge system runs across Kansas and through Nebraska. Given the reactivation of these faults observed over the last five years, a resurgence of high-rate fluid injections may heighten future risk in Kansas even in regions further to the north.

2.5 Earthquake swarms

A notable facet of the earthquakes that are occurring on these newly reactivated faults is the propensity for earthquake swarms. Earthquake swarms were identified within spatial clusters by DBSCAN this time, having four or more events within 36 hours in the same spatial cluster. Because the clusters were already evaluated for spatial relation, this analysis was done only for time in the vicinity of the largest fault 1, incorporating spatial clusters 1, 2, 5 and 3 in Figure 2.4a. Twenty-one swarms were identified ranging in duration from about ten minutes up to seven days. The time between clusters was as short as two days and as long as four months. The number of earthquakes in the 21 temporal clusters ranged from 4 to 115 (Figure 2.6).

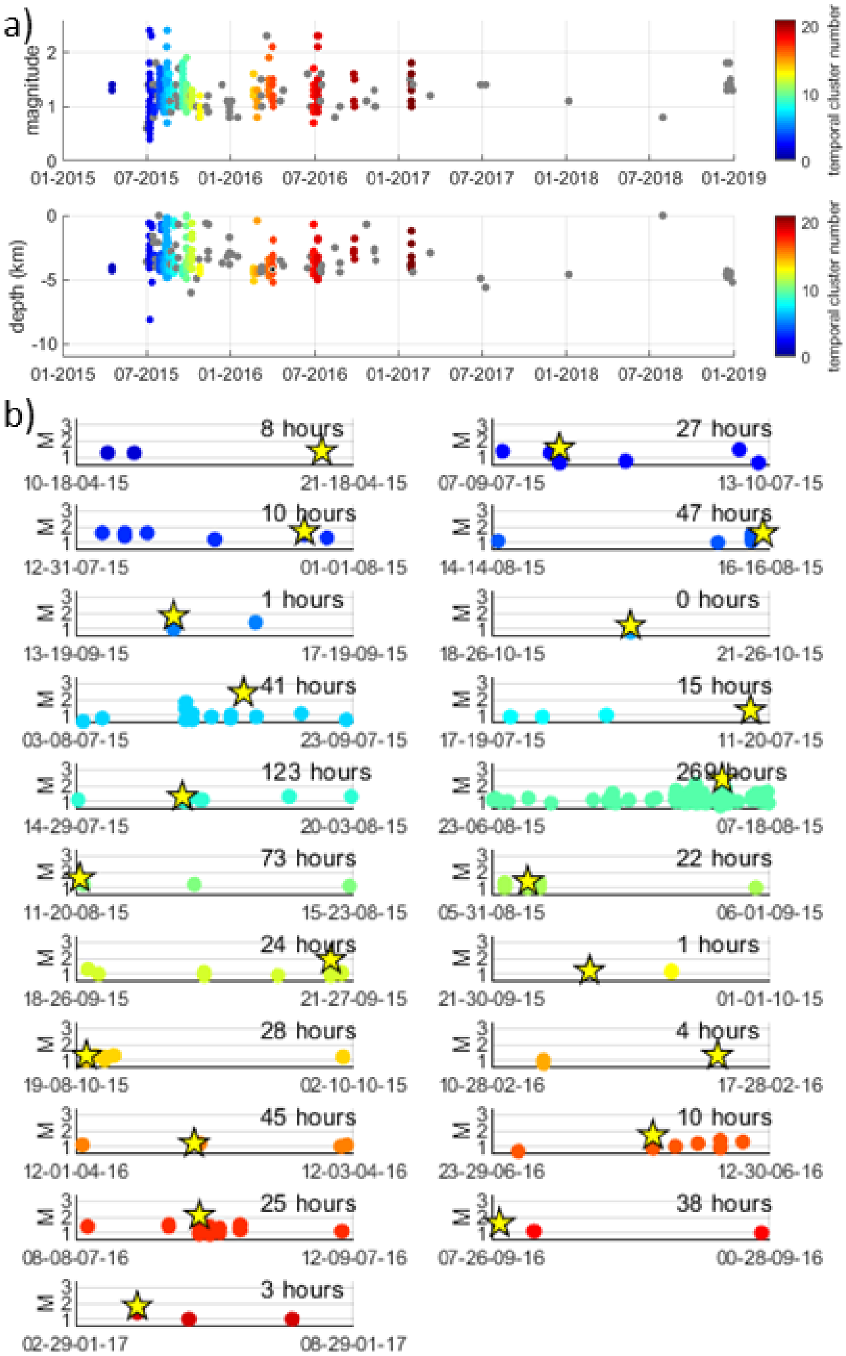

Figure 2-6: Earthquake swarms.
a) Earthquake magnitude and depth vs. time for events identified in spatial clusters 1,2,3 and 5 from **Figure 2.4a.** Color identifies the temporal cluster. b) Plots of individual swarm (temporal cluster) magnitude vs. time. Yellow stars denote the largest earthquake in each swarm. The length of time shown in each window is provided.

The earthquakes on this fault show major characteristics of swarm like behavior indicative of induced earthquakes (Skoumal et al., 2015). The main or largest event is not significantly larger than other events in the swarm and this event does not occur in the pattern of foreshock/mainshock/aftershock. There could even be multiple earthquakes of the same maximum magnitude. Instead, the largest magnitude earthquake can occur as the first, last, or somewhere in the middle of the swarm, as denoted by the gold star in Figure 2.6b. Earthquakes within each temporal cluster occurred in the upper 5 km of the subsurface with no evident depth pattern. The behavior of swarms of mainshocks has also been identified in other fields in which the earthquakes are suggested to be of induced origin (Schoenball and Ellsworth, 2017).

Although the fault in Figure 2.6 has reactivated multiple times with different swarms, there has not been a swarm since mid 2017, when seismicity in the region declined sharply, although occasionally individual earthquakes do occur.

2.6 Discussion and Conclusion

Earthquake observations in this study show that seismicity in Sumner County has advanced northward, but that the rate of seismicity has been declining since late 2017. Seismic activity in the region has been linked to increased regional pore fluid pressure (Keranen et al., 2013; Langenruch et al., 2018; Rubinstein et al., 2018; Dempsey et al., 2019), despite the lack of high-rate injection wells in Sumner County. This indicates that the increased seismicity has likely been influenced by more distant injection wells in the region. This study has identified earthquakes M2+ that have spread north across most of Sumner County in under two years.

Although some earthquakes had depths that would place them in the sedimentary section (figure 2.2a), these are likely location errors. It is theorized that all seismicity has occurred occurring in the shallow basement. A new method developed to constrain local earthquake depths using this catalog, presented next in chapter 3, confirms that these earthquakes—initially located in the sedimentary section—have poorly constrained depths and are most likely occurring in the basement (Nolte and Tsoflias, 2020 *in review*).

Earthquake monitoring at the Wellington Seismic Network in Sumner County has revealed previously unknown faults that appear to fit into the Nemaha Ridge system. These faults are oriented at ~45° and ~105°, which is in line with previous study estimates of potential failure orientation based on the stress regime of the region (Alt and Zoback, 2017; Schwab et al., 2017) and align with regional gravity and magnetic basement lineaments (Elebiju et al., 2011). Faults are continuous between the basement and sedimentary section, providing fluid pressure communication paths. Schwab et al. (2017) mapped faults in the sedimentary units within the Wellington oil field, a location where many seismometers for this study were installed, that do not line up with the faults proposed in the basement here. Because these basement faults are part of the older Nemaha Ridge, it is expected that the faults would not be continuous into the sedimentary section. However, the faults in the sedimentary units continue into the shallow basement (Schwab et al., 2017). These shallow faults are not optimally oriented for failure and no earthquakes are expected to occur on them (Schwab et al., 2017). While these shallow faults have not been mapped to the depths of the newly identified re-activated fault network, the potential for these shallow faults to provide fluid connection between the sedimentary section and the granitic basement should be considered when interpreting how injection volumes affect reactivation of basement faults.

Earthquakes in this fault system exhibit swarming activity. When looking at the events temporally, one fault segment will activate, and nearly all of the observed activity in the field occurs along that fault. When that fault goes quiet, a new fault, usually further north, becomes active for a period of time. Once a fault is active, temporal swarms can occur on that segment after a period of inactivity. It cannot be determined if earthquakes on individual faults reactivate in any spatial pattern due to location accuracies of earthquakes.

While the mechanism of pore pressure induced earthquakes is poorly constrained at focal depths, recent studies have identified this swarming activity to be characteristic (Skoumal et al., 2015). This study in Sumner County bolsters the hypothesis that induced earthquakes cannot be expected to exhibit standard mainshock sequences. These earthquake swarms do not exhibit temporal patterns in depth or magnitude, despite being both temporally and spatially related. The lack of depth pattern may be unidentifiable with the location accuracy due to less-than-optimal station arrangement.

Chapter 3 Identifying direct SP converted waves constrain local induced earthquake depths

3.1 Abstract:

Seismicity in southern Kansas and northern Oklahoma in the past decade has been tied to fluid injections. In south central Kansas, the Wellington Earthquake Catalog is primarily composed of local, low magnitude earthquakes. A waveform was observed arriving between the direct P wave and direct S wave with particle motion similar to the P wave and amplitude of 50 to 200% of the P wave. This intermediate wave was identified as an S to P conversion (SP wave) occurring in the sedimentary rocks instead of the hypothesized basement to sedimentary section transition. Here, we exploit these converted waves to develop a new method for improving the depth accuracy of shallow earthquakes and to constrain Vp/Vs. The revised depth calculations further confirm that these local induced earthquakes are occurring in the shallow crystalline basement, below the sedimentary section where fluids are injected.

3.2 Introduction

The central United States began to see a historically unlikely surge in earthquakes in 2009, with particularly high areas of activity in northern Oklahoma and southern Kansas (Ellsworth, 2013; Ellsworth et al., 2015; Walsh and Zoback, 2015; Rubinstein et al., 2018). Seismicity in this area peaked in 2017, with the largest earthquake in Pawnee reaching an M5.8 (USGS NEIC Catalog).

The unprecedented increase in seismic activity is believed to be anthropogenic in origin, from the development of oil plays in the US Midcontinent. Multiple papers have suggested that the reinjection of wastewater is responsible for the local and regional rise in earthquakes

(Ellsworth, 2013; Keranen et al., 2013; Rubinstein and Mahani, 2015; Nolte et al., 2017; Rubinstein et al., 2018). Langenbruch et al., (2018) demonstrated that injection volumes correlated closely to the pore fluid pressure increase required to trigger induced earthquakes in central Oklahoma and southern Kansas. Similar occurrence of fluid injection induced seismicity associated with industrial operations has been observed across North America from North Texas (e.g., Frohlich, 2012) to Alberta Canada (e.g., Bao and Eaton, 2016).

In southern Kansas the majority of earthquakes occur in the shallow basement (less than 10 km), as is common with injection induced seismicity (Rubinstein et al., 2018; Nolte and Tsoflias, 2019). In this region, the near-surface rocks are nearly horizontally layered sedimentary strata, consisting of thick carbonates and shales with interbedded thin sandstones above a granitic basement (Merriam, 1963). Within these layers are the Mississippian and Arbuckle, both important to the oil industry as the primary play for hydrocarbon production and primary unit of wastewater disposal respectively (Evans and Newell, 2013). In southern Kansas the Arbuckle lies unconformably over the granitic basement at approximately 1700 m depth below surface (Walters, 1953, 1958; Carr et al., 1986). Faults and fractures allow fluid communication between the Arbuckle and basement facilitating the triggering of shallow earthquakes (Walsh and Zoback, 2015; Schwab et al., 2017; Langenbruch et al., 2018). Depth of local earthquakes is the most challenging location degree of freedom to constrain given the tradeoff between depth and origin time (Gomberg et al., 1990). This can be especially problematic when stations are not spaced azimuthally around the epicenter, an issue that is common among passive local monitoring networks with tight station spatial distribution, such as the Wellington Earthquake Monitoring Network presented in this study (see Data and Resources). Therefore, calculating the earthquake depth using a method that does not involve the tradeoff between origin time and depth can be valuable for obtaining accurate depth estimates for local earthquakes. Here we present how converted shear to compressional (SP) waves, when observed in local earthquakes, can constrain event locations.

3.3 Background

Converted sP waves that arrive between the P wave and S wave were observed by Umino et al., (1995) in north-eastern Japan. In that study, converted shear to compressional waves were identified in shallow earthquakes (<50 km) at relatively close epicentral distances (~150 km). These sP waves were reflections from the earth's surface, not direct arrivals. The sP wave was seen on the vertical channel with the direction of approach similar to the P wave. Additionally, the velocity and predominant period of sP wave was between the velocity of the S wave and P wave with an amplitude of 50-200% of the P wave. Umino et al., (1995) used sP depth phases in the shallow earthquakes to constrain earthquake depths. In shallow earthquakes, depths are commonly hard to define to a high degree of certainty due to significant geometrical barriers to calculation (Gomberg et al., 1990).

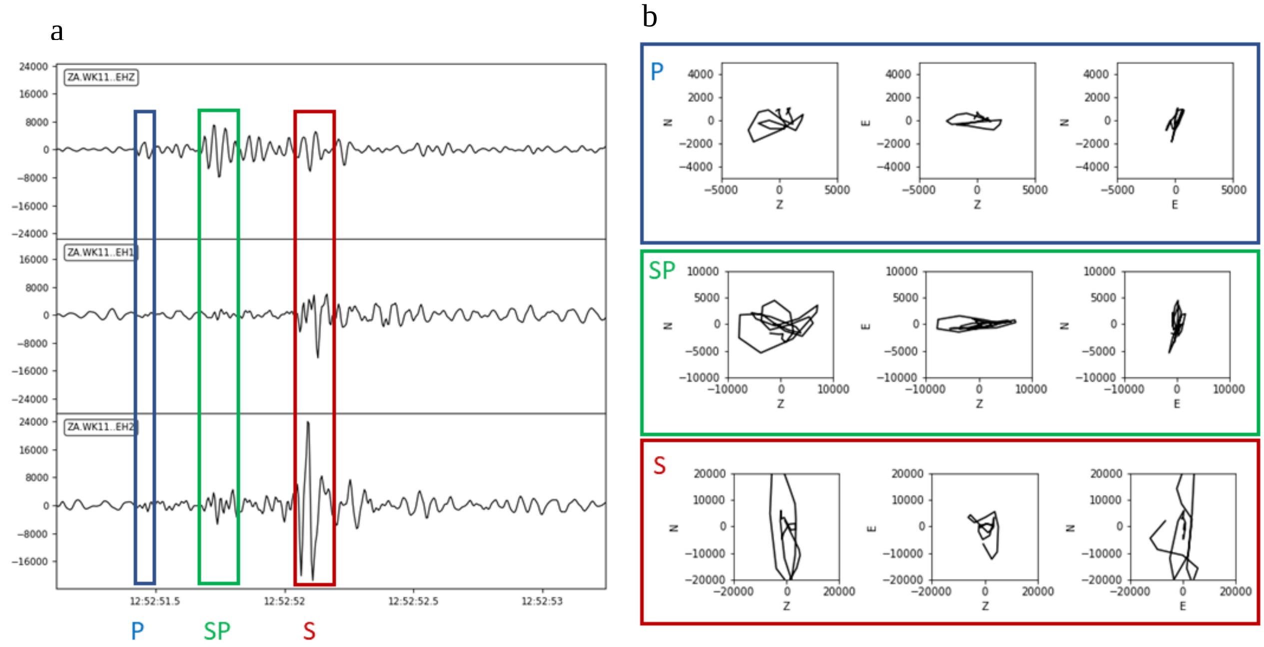

Figure 3-1: Example of a local Mw 0.8 earthquake approximately 5 km away from recording station WK 11 at the Wellington oil field network.
a) Three component waveforms: vertical (top), NS (middle), EW (bottom). The P wave can clearly be seen in the blue box (left) and the S wave can be seen in the red box (right). The green arrival (middle) is interpreted as a direct S-to-P converted wave. b) Particle motion crossplots for P, SP and S arrivals. The SP wave (middle) particle motion has similar particle motion to the P wave (top) and is therefore interpreted to be a P wave at the station.

In this study we present observations of S- to P wave conversion from very shallow (<5 km), local (epicentral distances <8 km) injection induced earthquakes recorded at the seismic monitoring network at Wellington Oil Field in southern Kansas. Approximately 4000 earthquakes have been cataloged since 2015 when the network was established. A subset of seismograms exhibit a wave arrival between the direct P and S waves with particle motion similar to the P wave and amplitude of 50 to 200% of the P wave (Figure 3.1), similar in appearance to a sP converted wave described in Umino et al., (1995). However, we interpret our SP arrival as a direct arrival converting at an interface below surface. Earthquakes in the Umino et al., (1995) study were exceptionally deeper and further away compared to the earthquakes investigated here. The converted waves observed here cannot be depth phases. Since the S wave is a direct wave, for these arrivals to be depth phases the S to P converted wave would likely arrive after the direct S wave.

We propose a new method that uses direct SP waves to improve earthquake depth constraint by providing a pseudo depth phase. Here, it is necessary to first determine where the wave conversion is occurring on, then a depth from the conversion interface to the earthquake hypocenter can be calculated. For earthquakes occurring in the shallow basement, it is unlikely that wave conversion occurs within the granitic basement rocks. Potential conversion surfaces can be the interface between the granitic basement and overlying sedimentary section, at approximately 1,550 m depth at Wellington, and/or contrasting rock properties in the heterogeneous sedimentary section. We use well log data available from the Wellington oil field and earthquake P, SP and S wave observations in a ray tracing approach to estimate the depth of the conversion interface, followed by the hypocentral depth of the earthquake estimation.

3.4 Methodology

We consider a two-segment travel path for each earthquake; from the hypocenter to the conversion interface and from the conversion interface to the surface. The earthquake depth calculation from the SP arrival is illustrated in Figure 3.2 using a conceptual schematic of two right-angled triangles. The upper triangle accounts for the travel distance above the conversion interface (ray segment f) and the lower triangle accounts for the travel distance below the conversion interface (ray segment c). Travel paths of local earthquake P, S and SP converted waves can be assumed to be nearly identical due to small epicentral distances and small incidence angles to interfaces.

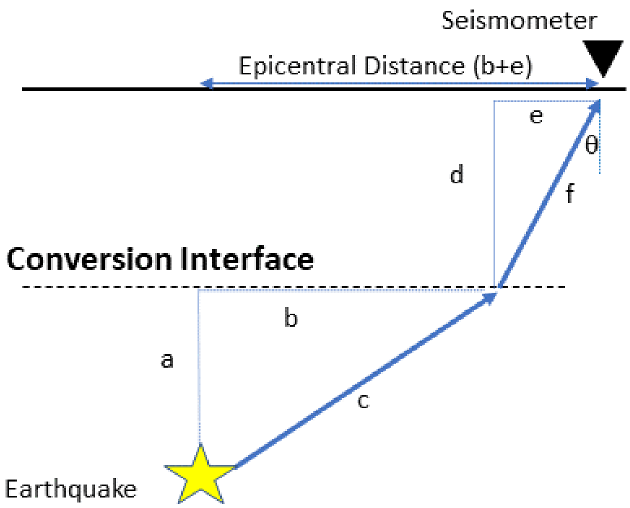

Figure 3-2: Schematic of earthquake raypath geometry from the hypocenter to the surface.
(c+f) illustrated by two triangles separated by the SP wave conversion interface (at depth d).The depth to the hypocenter is d+a.

Estimation of depth to the conversion interface

The arrival time difference ($\Delta t_{SP/S}$) between the converted SP wave and the direct S wave arises from the difference in travel times of the SP wave (T_{SP}) and the S wave (T_S) along ray segment f, since both waves originate by a direct S wave impinging to the conversion interface.

$$T_{SP} - T_S = \Delta t_{SP/S} \qquad (1)$$

Travel time can be converted to travel distance along ray segment f over velocity (V_u), where P and S subscripts denote corresponding waves

$$\frac{f}{V_{uP}} - \frac{f}{V_{uS}} = \Delta t_{SP/S} \qquad (2)$$

and

$$f = \frac{\Delta t_{SP/S}}{\left(\frac{1}{V_{uP}} - \frac{1}{V_{uS}}\right)} \qquad (3)$$

In our study the velocity structure of the upper triangle section is well constrained from borehole measurements. In the case where subsurface data is not available, regional velocity information for basement and sedimentary rocks can be used. The angle of incidence of the raypath (θ) is estimated from velocity ray tracing (Margrave, 2013). Angles of incidence for local earthquakes are typically between 15° and 35°. This angle (θ) and the length of the raypath (ray segment f computed in equation 3) are used to calculate the depth to the conversion interface (d) and the epicentral distance (e) to the pierce point of the ray from the station.

Estimation of hypocentral depth

Since the converted SP and direct P waves travel from the conversion interface to surface as P waves, this part of the raypath will be similar for close epicentral distances and it can be assumed that it does not contribute to the difference in arrival time of the two waves. Therefore, the difference in arrival time ($\Delta t_{P/SP}$) between the direct P wave and the SP converted wave is the difference of the travel times of the S wave (T_s) and the P wave (T_p) from the hypocenter to the conversion interface along ray segment c.

$$T_P - T_S = \Delta t_{P/SP} \qquad (4)$$

Travel time is converted to travel distance along ray segment c over velocity (V_l), where P and S subscripts denote corresponding waves

$$\frac{c}{V_{lP}} - \frac{c}{V_{lS}} = \Delta t_{P/SP} \qquad (5)$$

and

$$c = \frac{\Delta t_{P/SP}}{\left(\frac{1}{V_{lP}} - \frac{1}{V_{lS}}\right)} \qquad (6)$$

For each earthquake the epicentral distance (b+e) is calculated using a fixed epicenter, in this study calculated in Seisan (Havskov and Ottemoller, 1999) through Hypoinverse (Klein, 2007).The epicentral distance of the lower triangle (side b) is the total epicentral distance from station to earthquake minus the distance the pierce point is away from the station (side e). For this triangle the hypotenuse (ray segment c) is well constrained as it is the travel distance of the ray calculated by equation 6. With the two sides of the lower triangle (c and b) known the earthquake depth below the conversion interface can be calculated (side a), then added to depth d to obtain the hypocentral depth of the earthquake.

3.5 Field Application

In this study we examine earthquakes from the Wellington local earthquake monitoring network from January 2018 to July 2020, totaling 804 events (Nolte and Tsoflias, 2019). A total of 177 earthquakes had identifiable SP converted waves. On average, they ranged in magnitude from M 0.7 to 3.2, most located in the shallow basement and few in the lower sedimentary section. Initial earthquake depths determined by Seisan (Havskov and Ottemoller, 1999) ranged from 1 to 6 km.

Figure 3.3 shows a map of earthquakes with identifiable SP waves. Earthquakes with clear SP waves were located within 5 km of the seismic network with no clear directional bias. Ray tracing shows that a significant velocity change occurs in the sedimentary section of the pathway above the granitic basement interface. This indicates that the SP wave is not converting at the top of the basement, but within the sedimentary section likely at the top of the Arbuckle.

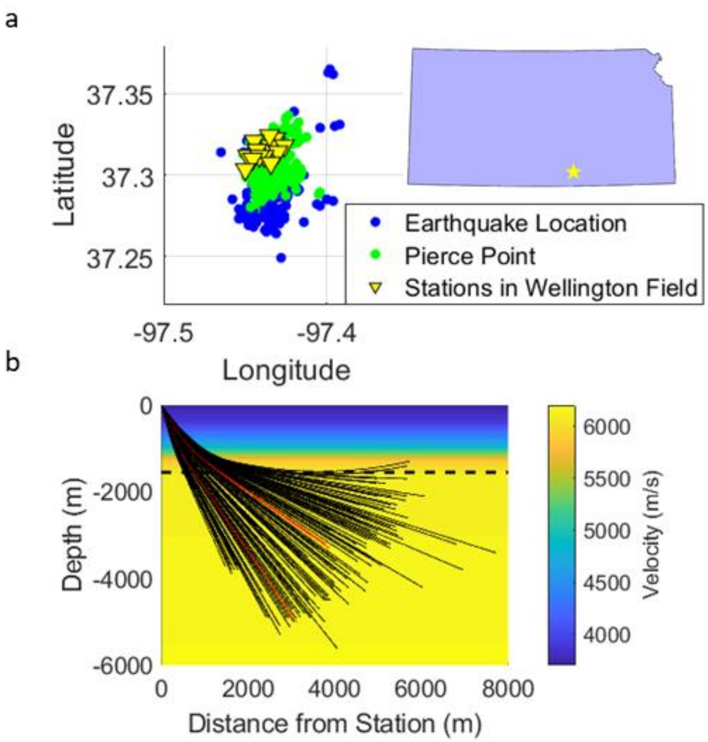

Figure 3-3: Map of earthquakes with SP waves and their raypath.
(a) Map of earthquakes that have an identifiable SP wave are shown in blue and the approximate locations where raypaths cross the conversion interface are shown in green. Seismic stations are shown in yellow triangles. The location of Wellington field in Kansas is marked by a yellow star. (b) Velocity ray tracing for earthquake depths determined in Seisan (Havskov and Ottemoller, 1999) as related to their distance from stations. Dashed line marks the top of granitic basement at approximately 1550 m depth. A sharp velocity contrast creating the conversion interface occurs shallower in the sedimentary section at the top of the Arbuckle. The velocity model shown here is the 1D model used in Seisan (Havskov and Ottemoller, 1999) for earthquake location. Red ray traces mark the ray paths with angles of incidence of 20° and 30°.

This result is supported by borehole velocity measurements and seismic reflection data at Wellington field (figure 3.4). The P wave velocity of the sedimentary section and the upper 25 m of the granitic basement was obtained from two well logs in the Wellington field and blocked into three velocity units (Figure 3.4a). Deeper P wave velocity in the shallow basement was estimated from limited velocity log data and from other studies in the region (Rubinstein et al., 2018). S wave velocity was calculated using a Vp/Vs ratio of 1.73 in the shallow basement.

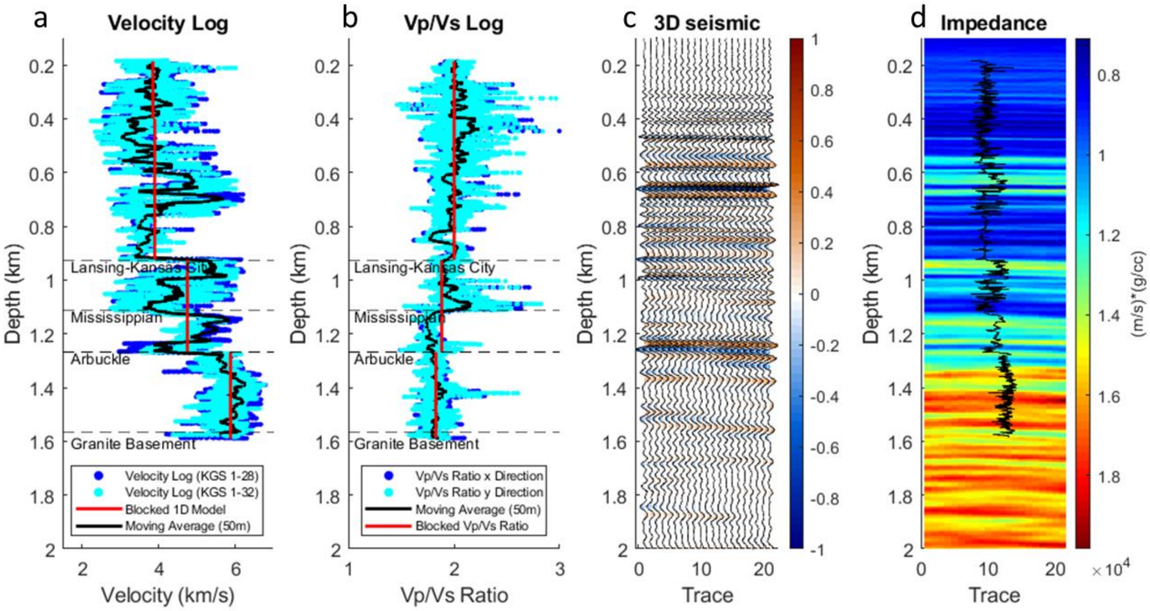

Figure 3-4: Wellington field borehole and reflection seismic data shown along with formation tops of the Lansing-Kansas City, Mississippian and Arbuckle.

(a) Velocity logs from wells KGS 1-28 and KGS 1-32. The red line is the blocked velocity model used in Seisan for earthquake location and the black curve is a 50 m moving average. (b) Vp/Vs ratio log from well KGS 1-28, showing both orthogonal horizontal shear components. The black curve is a moving 50m average and the red line is the blocked log used in calculating the near surface Vp/Vs ratio as well as the depth of the conversion surface. (c) Active source reflection seismic traces at the KGS 1-32 well. High reflectivity is observed at the top of the Arbuckle but there is very little contrast at the base of the Arbuckle into the basement. (d) Inverted acoustic impedance of the reflection seismic and computed impedance (black curve) at the KGS 1-32 well. The impedance section shows contrasting properties near the top of the Arbuckle but little change at the Arbuckle/basement interface.

Next, an estimate of the angle of incidence can be taken from velocity ray tracing, although the angle of incidence in this case has little effect in the raypath, as the difference in travel distance from the station to the piercing point is not affected significantly in the angles of incidence determined here (~15-35°). The difference in travel distance of a ray at an angle of 15° vs a ray at an angle of 35° is under 250m. However, when using equation 3 to solve for the depth to the conversion interface we obtained an unrealistic solution, placing the interface deeper into the granitic basement where no velocity contrast is known to exist (Figure 3.5). This occurs because the S wave velocity is calculated from a Vp/Vs ratio of 1.73 which is accurate in the basement rock but does not hold true in the sedimentary section. Thus, we recalculated the Vp/Vs ratio from the velocity logs available in the field (Figure 3.4b). The resulting average Vp/Vs ratio for the sedimentary section is 2.0 from a depth of 185m to 1550m. A value for the upper 185m where well log measurements are not available must then be chosen. For the ray to convert at the basement/sedimentary section interface a value of 2.85 is needed for the upper 185m. However, there is little impedance difference between the granitic basement and the dolomitic Arbuckle, as can be seen in Figure 3.4d. Thus, it is very unlikely that the wave is converting here. The next likely surface is the top of the Arbuckle. For this to be the conversion interface a Vp/Vs ratio of 3.48 is needed in the upper 185m. This value is well within reason for the uppermost sedimentary section, including unconsolidated sediments (Anno, 1986; Cary and Eaton 1993). Values as high as 8-9 can be possible in certain very shallow conditions (Bailey et al., 2013). A value of 3.48 then provides an average Vp/Vs of 2.185 for the sedimentary section down to the top of the Arbuckle.

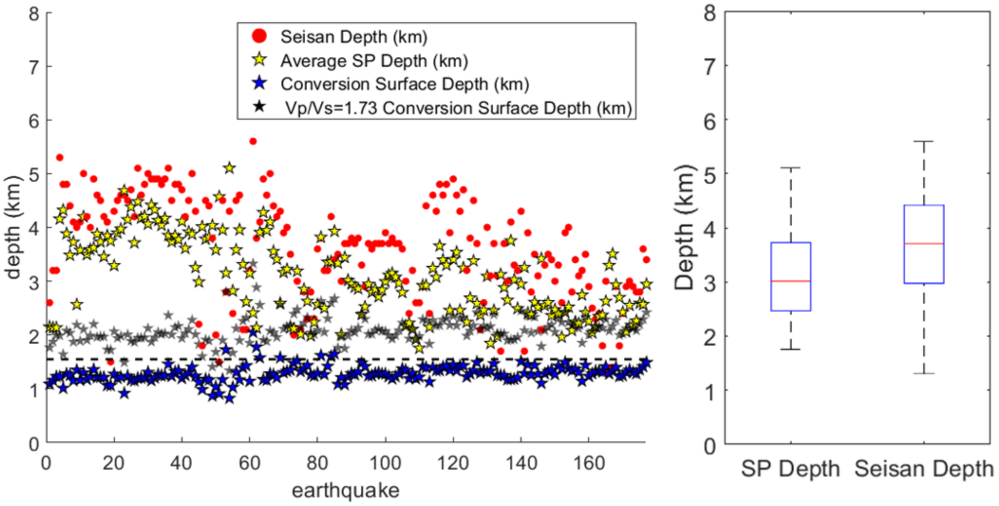

Figure 3-5: Depth corrections using the SP wave.
(left) Graph showing the original Seisan calculated depths in red circles and the new depth calculation from the SP waveform as yellow stars. The calculation for the depth of the conversion interface is shown in blue. The original conversion interface depth estimate without correcting the Vp/Vs ratio is shown in grey. The black dashed line is the depth to the granitic basement. (right) Box and whisker plot comparing the original earthquake depths calculated in

Seisan and the depths calculated from the SP wave method. The red line shows the median of each, the blue box the 25th to 75th percentile and the black line the maximum and minimum.

Using this velocity ratio causes the Arbuckle depth to be an average of 1,270 m from surface which agrees with depths determined through well logs. This calculation assumes a linear raypath above the conversion interface. This assumption is valid, given that ray tracing suggests the ray is 1.01x longer than the direct distance between the estimated piercing point and the station. The use of a near-surface Vp/Vs ratio estimate for the shallowest 185m as well as a high impedance contrast directly above the Arbuckle provide strong evidence that this is the conversion interface.

Earthquake depths as calculated by Seisan (Havskov and Ottemoller, 1999) are shown in Figure 3.5 (red circles) and they are compared to earthquake depths calculated using the SP wave method (yellow stars), assuming that the conversion surface is the top of the Arbuckle. SP converted wave depth estimates result in a better constrained depth range with less variation than Seisan depths (Figure 3.5). All SP converted wave depth estimates are in the shallow basement, eliminating the highly improbable few initial estimates in the sedimentary section. Importantly, the calculated depths of the SP conversion surface conforms to the depth of the top of the Arbuckle.

3D seismic data supports the top of the Arbuckle as the inflection point for converted SP waves. Impedance from the lower sedimentary section, as well as 3D seismic at the KGS 1-32 well indicate a large contrast of acoustic properties in the upper Arbuckle, extending through the Mississippian and the top of the Lansing-Kansas City units (Fadolalkarem, 2015). However, there is very little contrast at the base of the Arbuckle into the basement. This is further evidence, from the active source 3D seismic, that the conversion surface is likely in the sedimentary section. The most probable candidate is the Arbuckle below the Mississippian/Simpson, which exhibits a strong reflector in the 3D seismic and a sharp impedance change (Figure 3.4).

3.6 Discussion

In this study we exploit the presence of direct SP converted waves in local, shallow earthquakes to constrain earthquake depths. An important element of the method presented in the determination of the depth at which the S to P conversion occurs. It is notable that only very local events, with epicentral distances of 6 km or less, exhibit the SP converted arrivals. This results in low angles of incidence (~15-35°) and comparable travel paths between the P, S and SP waves of each earthquake. Ray tracing modelling (Figure 3.3b) suggests the ray is converting off of the top of the Arbuckle based off of the velocity model derived from well logs (Figure 3.4) and the estimate of Vp/Vs from the well log, and assuming a reasonable Vp/Vs value for the upper 185m.

Geologic intuition would suggest a significant velocity contrast at the top of the Granite basement and the base of the sedimentary section. However, well data reveal that the largest impedance difference is actually carbonate to sandstone in the sedimentary section. The velocity of the Arbuckle dolomite is 5.9 km/s and the granitic basement is 6.1 km/s. Granite density is 2.65-2.75 g/cm3 and dolomite is 2.8-2.9 g/cm^3. This is further shown in Figure 3.4, with data from the 3D seismic, showing next to no reflection at the sedimentary-basement contact but a very strong reflection at the top of the Arbuckle. However, the difference between the Simpson sandstone at the top of the Arbuckle is very obvious in acoustic properties as well as the 3D seismic. Sandstone has an average density of 2.6 g/cm^3 and the Simpson has a velocity of approximately 4 km/s. This provides for a strong reflector in the reflection seismic (Figure 3.4c) and a clear transition for a converted wave to occur at. In addition, the overlying Mississippian limestone exhibits further decrease in impedance compared to the Arbuckle dolomite (Figure 3.4d) and it may be contributing to the SP conversion.

In the midcontinent, SP waves can serve as additional confirmation that earthquakes are occurring in the shallow basement and not in the sedimentary column where fluid injection takes place. Earthquake locations can be fundamentally dependent on the efficacy of locations and on the accuracy of the network. Multiple methods of depth constraint, including measurements based on SP waves, can reduce the risk of error. In studies where the conversion surface depth can be determined with confidence, as within the Wellington field in which the Arbuckle depth is well defined, the SP conversion wave can be used to constrain the Vp/Vs ratio in the sedimentary section. This can improve shear wave models and refine constraint on velocity models.

When earthquakes occur close to the monitoring stations, SP waves will be most useful. Herein, SP waves were useful in depth constraining at an epicentral distance of 6 km. This should not be considered a maximum useful distance. However, earthquakes closer to the stations will be more reliable.

This method presented has two potential limitations. First, if shallow earthquakes (< 5 km) occur beyond ~10 km from the monitoring network, a two component linear raypath cannot be assumed. A bent raypath below the conversion interface and potentially above requires significantly more complex modeling. The theory for the calculation of the depth from the direct ray will no longer be valid as well. Second, the method we present assumes that epicentral distances can be determined accurately and used for the calculation of earthquake depth. While earthquake epicentral distance determination is typically better constrained than hypocentral depth, it may still not be accurate. However, even when the epicenter location contains error, the SP wave constrained earthquake depth will have less error than the initial hypocentral depth.

3.7 Conclusions

Herein, S to P converted waves in very local earthquakes were identified in the Wellington Earthquake catalog. These waves are similar in appearance to those identified in Umino et al (1995) but they differ in that they are converted waves that arrive at the station as direct waves. A new method using S to P converted waves was developed to better constrain depths of local earthquakes. According to figure 3.5 the depths are better constrained to the shallow granitic basement. The average depth is shallower and the range of depths is more limited compared to conventional earthquake location approach, which must solve for latitude, longitude, depth, and time based off of only P and S arrival times (e.g. Hypoinverse). Previously depths ranged from ~1.2-5.5 km, even placing a small number of earthquakes in the sedimentary section which is atypical based on large number of induced earthquake observations in the region. The new depth estimates using the SP arrivals range from ~1.7-5.2 km. This indicates that earthquakes are further constrained to the upper basement where they are expected to occur on reactivating faults, due to fluid injection in the Arbuckle, directly above the basement. The converted waves were also used to calculate very shallow Vp/Vs ratios passed over by standard logging techniques. In addition, the method allowed to back calculate the depth of the conversion interface, which in this study it was known from independent observations at Wellington oil field.

Chapter 4 Induced Earthquake Shear-wave Splitting Parameters

4.1 Abstract

The US midcontinent has seen a large increase in seismicity over the past decade. Spatiotemporal correlations of earthquakes and wastewater injections as well as pore pressure fluid models have been used to relate induced seismicity to high-rate wastewater disposal wells and hydraulic fracturing. Here, we examine the link between changes in shear-wave anisotropy and induced seismicity. Shear-wave analysis shows, for the first time, that the anisotropy in central Sumner County, south-central KS has significantly changed from 2015 to 2017, which coincides with the time period of high earthquake activity and wastewater disposal in the region. The analysis of distant (>10 km) earthquakes for anisotropy identified changes (flips) in the orientation of the fast shear wave (ϕ) from along maximum horizontal stress to an oblique orientation. This change has been shown in other settings to be linked to rocks with critically stressed pore fluid pressure. Further monitoring into 2020 shows the changes in S-wave anisotropy remain, indicating an elevated pore fluid pressure. We present changes in S-wave anisotropy, which aligns temporally with *in situ* pressure monitoring in the Wellington oil field. We conclude that temporal changes in S-wave anisotropy in Sumner county provide evidence of critically pore pressure stressed subsurface. The methods presented here may be used to identify remotely critically pore pressure stressed regions that are at risk of experiencing induced earthquakes.

4.2 Introduction

The US midcontinent has experienced a dramatic increase in earthquake occurrence since 2012 (Ellsworth, 2013; Langenbruch and Zoback, 2016). Most studies have correlated earthquake increases to pore fluid pressure increases caused by high-rates of injection of wastewater

(Ellsworth, 2013; Keranen et al, 2013; Keranen et al, 2014; Ellsworth et al, 2015; Walsh and Zoback, 2015; Langenbruch and Zoback, 2016; Rubinstein et al., 2018; Dempsey et al., 2019). Recent studies also showed that hydraulic fracturing is causing seismicity in Oklahoma (Skoumal et al., 2018). However, little is known about fluid flow and pore pressure diffusion pathways in the shallow basement (Keranen et al., 2013; Dempsey et al., 2019). Finding a means to detect elevated pore fluid pressure *in situ* without costly drilling or equipment would provide near real time information on the current status of increased pore fluid pressure. This would help inform decisions on injection volumes and locations.

Shear-wave splitting occurs when a wave travels through an anisotropic medium (Crampin, 1985; Crampin and Zatsepin, 1997; Crampin, 1999; Crampin et al., 2004; Crampin and Peacock, 2005) such as faulted and fractured shallow basement rocks in the U.S. midcontinent (Baars, 1995). Wave propagation oblique to the anisotropy causes the S-wave to split into two components: a fast S-wave polarized parallel to the fast axis of the anisotropy (e.g. along the maximum horizontal stress (SH_{max})) and a slow S-wave polarized obliquely to the fast axis (Crampin, 1985; Crampin and Zatsepin, 1997; Crampin, 1999; Crampin et al., 2004; Crampin and Peacock, 2005). The difference in the arrival times between the two S-waves is δt, and ϕ is the azimuthal angle of the fast S-wave orientation (Figure 4.1) (Crampin, 1985; Crampin and Zatsepin, 1997; Crampin, 1999; Crampin et al., 2004; Crampin and Peacock, 2005).

The build-up of critical pore fluid pressure allows for natural fault systems to slip (Crampin and Zatsepin, 1997; Zinke and Zoback, 2000; Crampin et al., 2000). The first observation of induced critical pore fluid pressure change evidenced by S-wave splitting occurred while monitoring the injection of CO_2 in a fractured reservoir using time-lapse 3D reflection seismic

(Angerer et al., 2002). In that study, prior to injection, the fast S-wave orientation lined up with the maximum horizontal stress as expected in natural systems. Following the injection, which raised reservoir pore fluid pressure by 6.4 MPa (928 psi), the fast S-wave orientation flipped ~90° aligning with the minimum horizontal stress (SH_{min}).

Shear-wave splitting analysis of naturally occurring earthquakes has been used to identify critically pressured zones from pore fluid through observation of orthogonal, approximately 90° flips in the fast S-wave orientation, causing it to align with the minimum horizontal stress (Crampin et al., 2004; Crampin and Peacock, 2005; Zinke and Zoback, 2000). Flips in ϕ orientation from SH_{max} to SH_{min} are seen when the raypath travels a greater distance in elevated pore fluid pressure zones than in normally pressured rock (Crampin et al.,, 2004). Change in travel path ratio of critical fluid pressure to normal fluid pressure can have a significant impact on the range of time delays (δt), with up to an 80% scatter in values (Crampin et al.,, 2004). Shear wave splitting is capable of detecting three sources of velocity anisotropy in shallow earthquakes. The types of anisotropy can be broken into two categories. Vertical transverse isotropy (VTI) and Horizontal transverse isotropy (HTI) (Figure 4.2). VTI refers to anisotropy between horizontal isotropic sheets. An upgoing S-wave would not detect VTI whereas a horizontally propagating shear-wave would detect VTI. There are two types of HTI. Stress-induced HTI exists where the SH_{max} causes small fractures to open, creating fracture anisotropy along SH_{max} (Figure 4.2, b). In stress-induced HTI, the fast S-wave will align with the maximum horizontal stress direction whereas the slow S-wave will be orthogonal to the maximum horizontal stress direction. Structure-controlled HTI occurs where anisotropy is dominated by a fault or fault zone (Figure 4.2, c). In structure-controlled HTI, the fast shear-wave will align with the fault system.

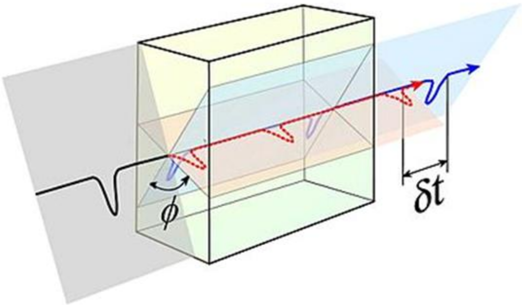

Figure 4.1-1: Schematic of shear wave splitting in anisotropic media (Garnero, 2017). The incident S-wave (black) enters an anisotropic medium (yellow block). The S-wave splits to a fast S-wave polarized parallel to the the anisotropy (blue), and a slow S-wave polarized obliquely to the fast axis (red).

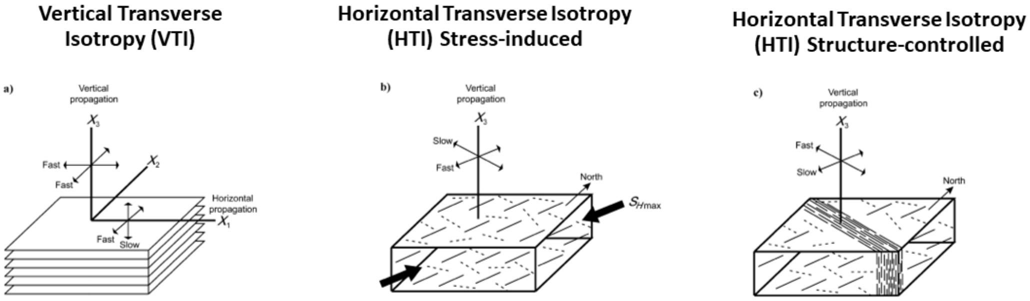

Figure 4.2-2: Common types of anisotropy detected through sheer wave splitting (Boness & Zoback, 2006).

The most common type of anisotropy detected through shear wave splitting is HTI. The shallow basement of the midcontinent is highly fractured and faulted (Baars, 1995). These fractures and fault systems are subvertical, and can be sources of HTI anisotropy, along with the maximum horizontal stress. As described in chapter 2.3, the orientation of the major tectonic structures in south-central KS are approximately NNW (310°) and NNE (30°) (Lee and Merriam, 1954; Baars, 1995; Elebiju et al., 2011). Since fractures occur in nearly all directions, the dominant source of anisotropy from factures is expected to be from those that are parallel to the maximum horizontal stress and are therefore open because of their orientation within the stress field.

However, in the sedimentary section the open fractures are those at 30° (Schwab et al., 2017). The maximum horizontal stress in the region of study is between 75° (Schwab et al., 2017) and 80° (Alt and Zoback, 2016). The orientation of potential sources of S-wave anisotropy in south-central Kansas are shown in figure 4.3.

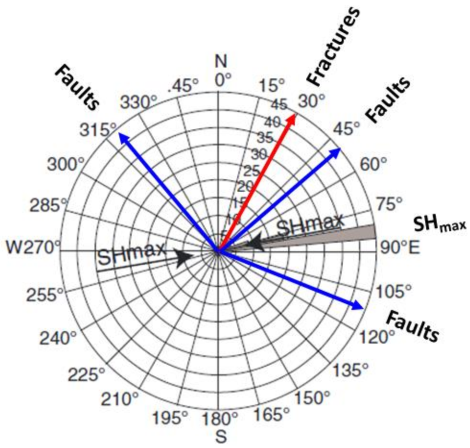

Figure 4-3: Orientation of potential sources of shear-wave anisotropy in south-central Kansas.
Data compiled from Baars (1995), Schwab et al. (2017) and Alt and Zoback (2016).

4.3 Background

Anisotropic analysis was conducted on a catalog from the Wellington Earthquake Monitoring Network. Seismometers were deployed in 2015 to monitor increases in local seismicity. Approximately 4,000 earthquakes were detected between 2015 and 2020 while the network was active. The magnitude of completeness is 1.6 for Sumner County, the area of interest. Larger earthquakes were detected for the region as well. For a full review of the catalog please see Chapter 2.

Shear-wave splitting analysis has been used extensively in natural faulting environments, but a recent pilot study by the Principal Investigators (Nolte, 2017; Nolte et al., 2017) is the first to apply the analysis to induced earthquakes. Previous studies have used shear-wave anisotropy analysis to identify temporal changes in stress from natural activity. Anthropogenic stress changes are likely much smaller than natural changes, but the techniques described here have shown capability in detecting small stress changes by monitoring induced seismicity.

A recently completed pilot study focused on shear-wave anisotropy analysis of earthquakes in southern Kansas with a few more distant earthquakes in Oklahoma (Nolte et al., 2017). Nolte et al., (2017) demonstrated that this method is capable of detecting changes in shear wave anisotropy, which was interpreted to be caused by pore fluid pressure changes. Seismic anisotropy analysis of 150 earthquakes confined over a relatively small area of south-central Kansas and northern Oklahoma, was evaluated over seven years starting in 2010 and ending in 2016. Earthquakes were analyzed for δt, and ϕ using a handpicked window technique along with the methodology of Silver and Chan (1991). Consistent flips in ϕ orientation and δt scatter were observed over the seven year time period (Figure 4.4). This analysis provided evidence of temporal change in the anisotropy of the basement. Nolte et al. (2017) attributed the S-wave anisotropy change observations to the increase in pore pressure that had occurred in the region over the same time period. However, due to the lack of dense earthquake coverage, this initial work could not assess with confidence potential effects on S-wave anisotropy due to varying raypaths, i.e. differences in wave travel distance and azimuth from the hypocenter to the monitoring stations. Having added four years of observations and thousands of additional earthquakes in the database, this study expands the initial work by Nolte et al. (2017) by examining clusters of seismicity, presumably from earthquakes occurring on the same or neighboring (similarly oriented) faults, and thus eliminating uncertainty in the anisotropy analysis that can be introduced when raypaths vary in distance and azimuth. The focus now is on observing very local earthquake S-wave splitting, to avoid these sources of potential error.

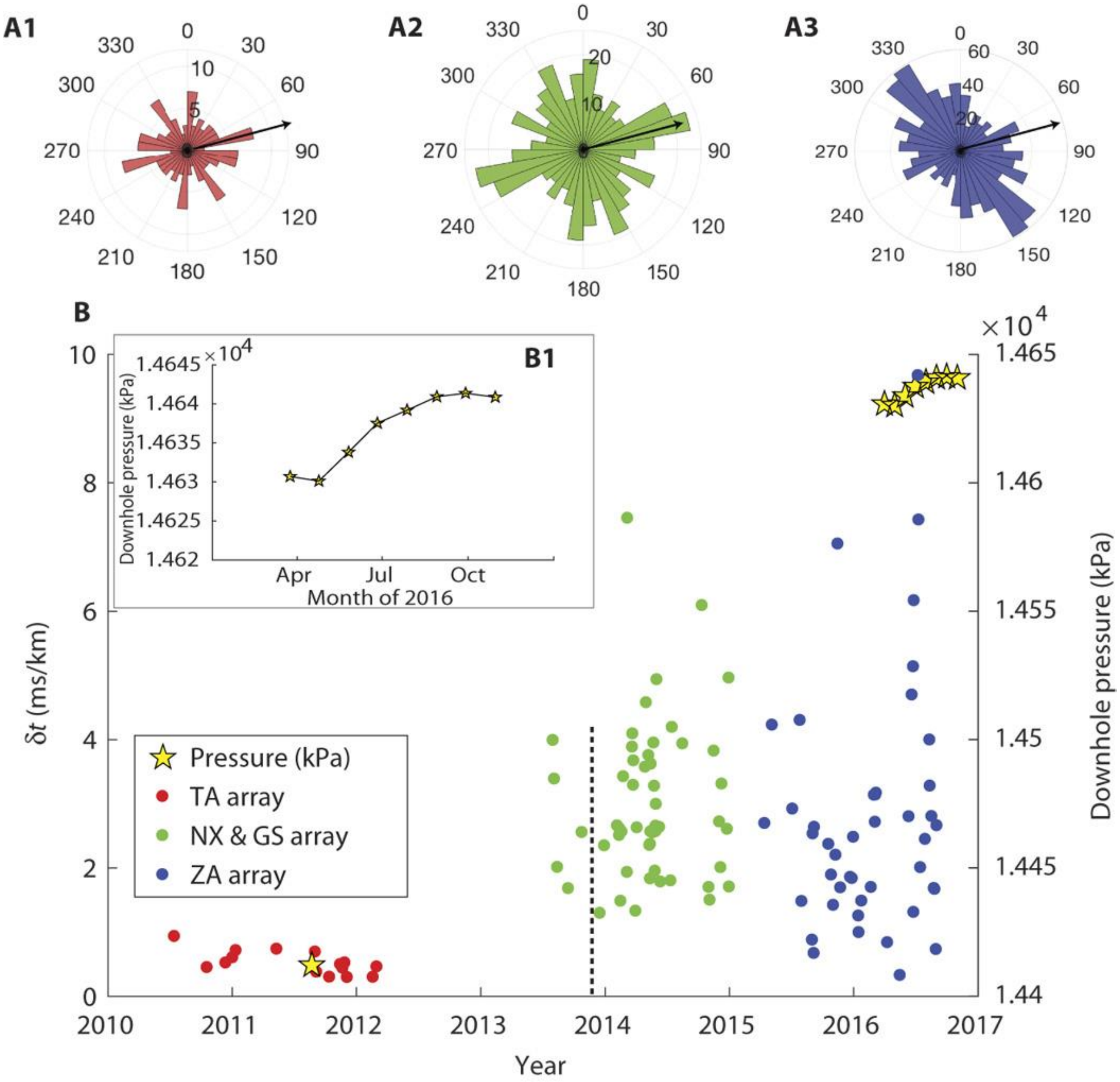

Figure 4-4: Temporal observations of ϕ and dt, and downhole pressure at Wellington.
(A1) Polar histogram of ϕ from earthquakes in 2010-2012 (red). (A2) Polar histogram of ϕ earthquakes in 2013-2015 (green). (A3) Polar histogram of ϕ from earthquakes in 2015-2016 (blue). (B) Average dt/km of earthquakes from 2010-2016. Yellow stars correspond to average monthly pressure observations in well KGS 1-28 at Wellington Oil field. The initial pressure measurement in August 2011 was obtained when the well was drilled (dashed line). Inset B1 is an expanded view of monthly average downhole pressures from April to November 2016 (from Nolte et al., 2017).

4.4 Methodology

The methodology used in Nolte et al. (2017) is difficult to scale up to a large number of events, as it requires each shear-wave to be manually identified and the SC91(Silver and Chan, 1991) algorithm applied to the correct arrival. Performing shear-wave splitting analysis on a large data set requires a more automated technique. Here, we propose automating the shear-wave analysis based on the methods developed by Teanby et al. (2004) and Savage et al. (2010). These automated methods apply the SC91(Silver and Chan, 1991) technique. The Teanby et al. (2004) method can be easily applied, but it lacks quality control in solutions as compared to the Savage et al. (2010) method. This analysis has been proven to work in a wide array of anisotropy environments; however, the results can be significantly affected by the window length chosen, as well as the frequency of the data (Savage et al., 2010). Figure 4.5 shows a manually picked shear wave from the Wellington Earthquake Catalog in the transverse and radial components, showing a separation in the arrival time of the transverse and radial shear wave which indicates the presence of anisotropy.

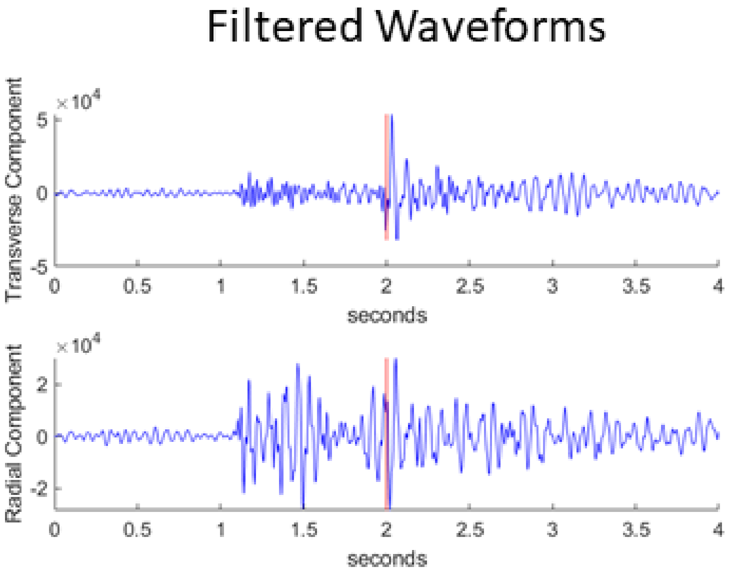

Figure 4-.5: Filtered waveforms in transverse and radial components.
Shear wave arrivals are picked manually at the red line. Pick on Transverse component can be seen at shear wave arrival (at ~2.0 seconds), whereas the shear wave arrives well before the red line on the radial component (at ~1.8 seconds).

However, manually picking radial and transverse S-wave arrivals introduces potential user-bias and it is labor intensive. The proposed method identifies the shear-wave arrival by hand and uses the computer to find the best window around the arrival, thus eliminating the user-bias associated with handpicking the window and reducing the amount of manual processing. Automatic window picking is performed by a grid-search method, where the computer tries a wide range of windows and selects the best solution from them (Teanby et al., 2004).

The window size for local earthquakes is often very short. The use of short windows helps to eliminate cycle skipping, where the solution jumps by an integer number of half wavelengths. Eliminating cycle-skipping while maintaining a long enough window to ensure accurate results requires a good shear-wave pick and effective window lengths. The windows used in this study ranged from 0.02 to 0.1 seconds before the s-wave arrival and from 0.02 to 0.4 seconds after the arrival, by increments of 0.02 seconds. This gives 225 unique time windows to calculate the SC91 algorithm (Figure 4.6). The number of windows is directly related to processing time since each window is fully processed regardless of whether it is the correct solution.

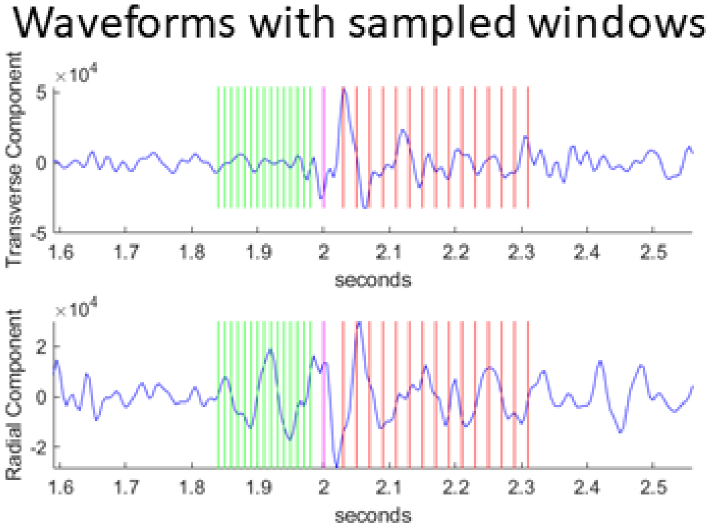

Figure 4.6: A shear wave arrival showing window edges of automated methodology.
Green signifies the start of a search window and red lines are the end of the search window. The magenta line is the manually picked shear wave arrival.

Other studies also use bandpass frequency filtering over small frequency windows (~1-5 octaves) to return earthquakes with a high signal-to-noise (S/N) ratio (Savage et al., 2010). Since the Wellington network earthquake data has high S/N ratio and a wide range in dominant frequencies (due to distance from the stations), we use a wide bandpass filter. Initial analysis has been successful with a bandpass filter from 2-25 Hz (~3 octaves), as it still provides high S/N (Savage et al., 2010) without compromising the waveform.

The filtered data is then processed by the SC91 technique, returning a ϕ and δt value for each window, as well as an error for both variables. The ϕ and δt for each window need to be searched for the most accurate solution. This is performed by a cluster analysis of the variable values (Teanby et al., 2004). The two cluster analyses used are those of Calinski and Harabasz (1974) and Duda and Hart (1973), replaced here by an optimized version of Duda and Hart called the Gap method, already coded into MatLab (The Mathworks, Inc). Figure 4.7 shows the 11 clusters identified by the automated methodology in ϕ and δt space.

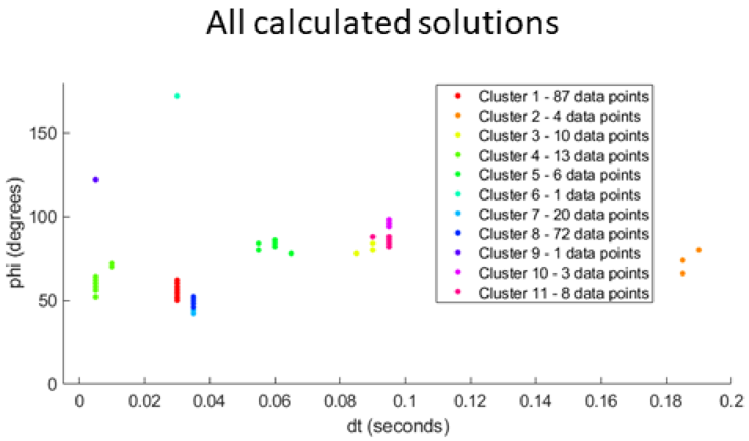

Figure 4.7: All calculated solutions from the automated windows in ϕ and δt space.
Solutions from the waveforms in Figure 4.5 and 4.6.

Calinski and Harabasz (1974) finds the number of clusters that maximizes between cluster variance to within-cluster variance. Duda and Hart (1973) and the Gap method uses a ratio of within-cluster variance between two clusters as compared to the within-cluster variance of the two clusters combined into one cluster. Once the data is separated into the optimum number of clusters, the best cluster is chosen by the lowest within-cluster variance (Teanby et al., 2004). The cluster must also contain a minimum number of points, equal to one cycle worth of data (Teanby et al., 2004). In this case, based on one cycle of 12.5 Hz lasting 0.08 seconds, the minimum number of points is 8. The best solution is simply the solution with the smallest variance from the best cluster (Figure 4.8) (Teanby et al., 2004).

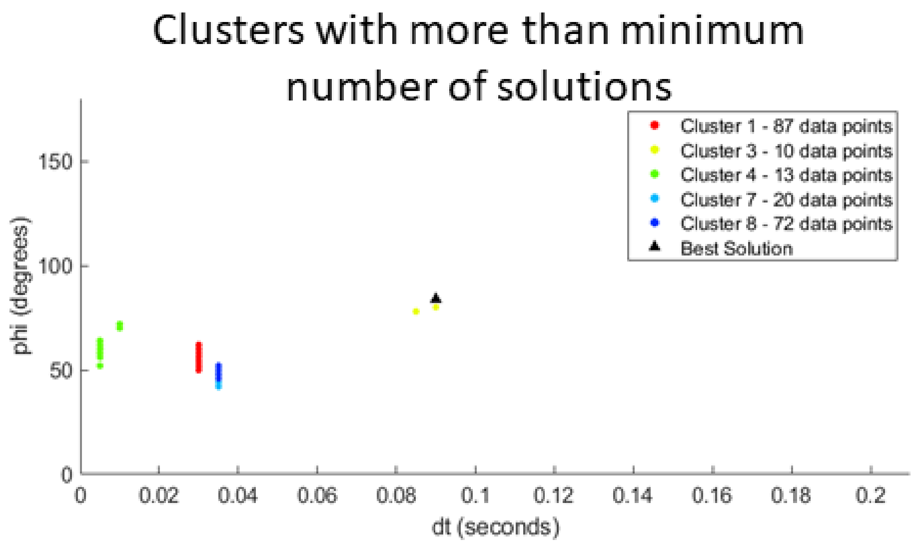

Figure 4.8: Clusters calculated from the automated methodology with a minimum of eight points.

This methodology provides a robust solution, but does not provide a comparison of the solution quality, which is very common in shear-wave splitting analysis. These automated results are computationally expensive but eliminate the need for human oversight. This allows for shear-wave analysis to be performed on all available data that is of high enough quality. Since this automated technique provides less quality control than manual techniques, poor solutions may be given, but this is offset by the larger volume of data that can be processed.

4.4 Results

Following the study of Nolte et al. (2017), analysis focused on observing very local earthquake S-wave splitting. This was expected to reduce errors associated with azimuthal anisotropy as well as differences in velocity along the raypath, not associated with shear-wave splitting. The comparison of very local earthquakes could also limit free surface and surface wave effects with the arriving shear-wave.

4.5.1 Results from Teanby et al., 2004 Method

We established a methodology based on Teanby et al., (2004) to evaluate earthquake clusters for regional differences in temporal changes in shear wave anisotrpy. Figure 4.9 presents polar histograms of S-wave anisotropy analysis of two clusters of earthquakes, referred as the north cluster the south cluster. The locations of the two clusters are identified by black boxes in figure 4.9. Earthquakes within each cluster have comparable azimuth and distance to the monitoring stations. In relation to each other, the two clusters are separated by10 km in an approximately north-south direction. In addition, as shown in chapter 2, seismicity in the region advanced from south to north presumably due to an advancing pore pressure front, and therefore, the two clusters may experience different temporal changes to the local stress field. There are 141 earthquakes in the northern cluster and 253 earthquakes in the southern cluster.

The north cluster (Figure 4.9, upper) during years 2015 and 2016 shows ϕ orientations that are in line with the structural trends in southern Kansas, trending ~30° and ~310° as identified by the blue and red arrows, as well as a number oriented along SH-max. Although neither 2015 nor 2016 has a large data set because of the lower seismicity to the north of Wellington field as presented in chapter 2, combined they provide compelling evidence that the ϕ orientation was aligned with structure during that time period. Then, in 2017, nearly all ϕ orientations rotate to be aligned with the maximum horizontal stress direction (75°-80°), identified by the black arrow.

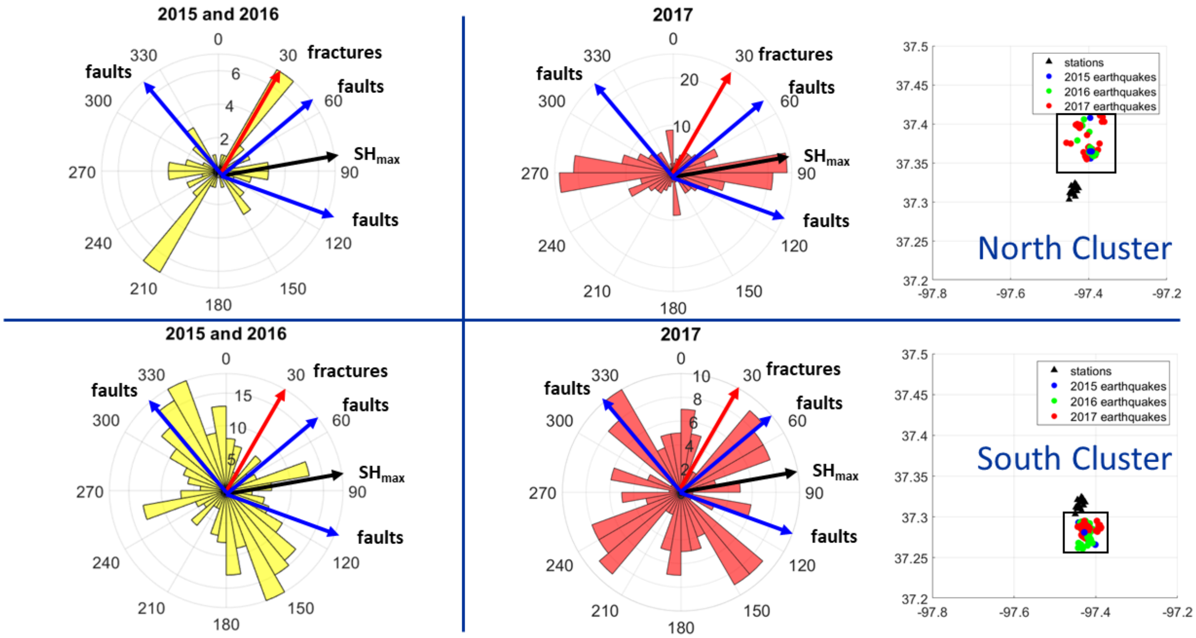

Figure 4.9: Polar histograms of S-wave anisotropy orientation (ϕ) from the North (upper) and South (lower) earthquake clusters.

Arrows indicate the orientation of potential sources of anisotropy in southern Kansas from figure 4.3. Map view (right) of earthquake locations color coded by year. S-wave anisotropy shows temporal changes over the monitoring period 2015 to 2017. Results are shown for two clusters of earthquakes at differing distances from major injection wells to the south of the study area.

The southern cluster (Figure 4.9, lower) shows a distinctly different behavior in the ϕ orientation when compared to the north cluster. In 2015 and 2016 the majority of the ϕ orientations are nearly perpendicular to the maximum horizontal stress direction (black arrow) and along structure (~310° blue arrow). A smaller number of events is along SH-max. In 2017, the southern cluster shows mixed ϕ orientations predominantly along structure (blue arrows) and some along SH-max.

Observations of S-wave anisotropy in naturally occurring earthquakes in volcanic settings suggests that change in ϕ orientations (flip from SH-max) indicates that the shear-wave has traveled through rock that is critically stressed by pore fluid pressure (Crampin et al., 2002). At

Wellington field we have independent observations of pore fluid pressure change from downhole monitoring in the Arbuckle at a depth of 1150 m, approximately 30 m above the granitic basement. Figure 4.10 shows pressure data from the KGS 1-28 well which is located in the center of the study area. The initial pressure data point was from the completion of the well in 2011. The 2016 data was from real time pressure monitoring in the well. The pressure increased 30 psi (200 kPa) since the well was completed in late 2011. This pressure seemed to reach a maximum in late 2016 before beginning to decrease. Other pressure models of this region suggest a similar timing for reaching the maximum pressure (Langenbruch et al., 2018; Figure 1.2), followed by a decline in pressure related to regional reduction in injection rates imposed by state regulatory agencies.

In the southern cluster, the 2017 data shows ϕ orientations that are mixed between flipped and in line with the maximum horizontal stress direction and along structure. This change compared to 2015-2016 indicates that the critical pore fluid pressure change is no longer occurring in 2017 at the magnitude of 2015-2016 that may have caused homogeneous flips. We interpret this as a transition period. This transition period could indicate that there is still sufficient elevated pore fluid pressure to cause the maximum horizontal stress to not be the only source of detectible anisotropy.

The cluster to the north shows ϕ orientations that are in line with predominantly structural control in southern Kansas in 2015 and 2016. Then in 2017 ϕ orientations are nearly all in line with the maximum horizontal stress direction. This change most probably indicates that in 2015-2016 the region had undergone an increase in pore fluid pressure great enough to reduce the effects of the maximum horizontal stress on shear wave anisotropy, but not large enough to cause 90°

flips in ϕ. In 2017, pore pressure reduction yields the expected ϕ orientation for the region along maximum horizontal stress.

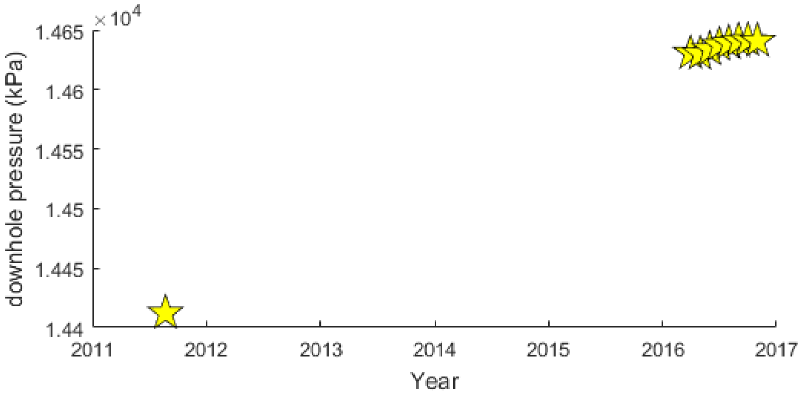

Figure 4.10: Arbuckle pressure measured in KGS well 1-28.

4.5.2 Applying S-wave Anisotropy Analysis Method on Very Near Earthquakes

While the Teanby et al. (2004) method showed clear flips in anisotropy (Figure 4.9), the lack of quality control mechanisms resulted in data that was highly variable with significant spread. Thus we moved to the methodologies establisehd by Savage et al. (2010). We first evaluated the local earthquakes in the Wellington earthquake catalog (comprising 5,714 earthquake-station solutions processed) utilizing these new methods (presented in section 4.4), shown throughout the rest of the chapter.

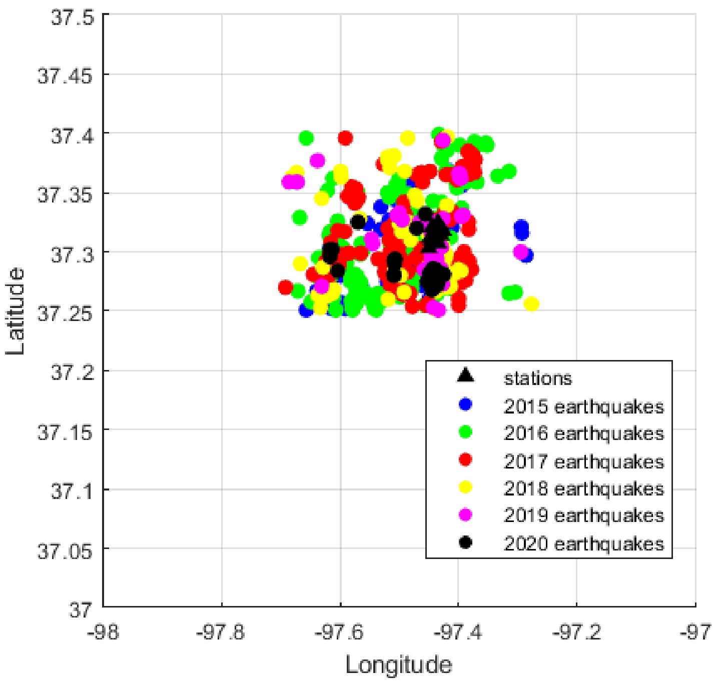

Figure 4.-5: Map showing stations in black triangles and earthquakes color coded by year of occurrence. Earthquakes shown here were used in analysis of very local earthquakes, totaling 5,714 earthquake-station measurements

Local earthquakes that fulfilled the criteria of the method in the Wellington Oil Field are shown from 2015 to 2020. These criteria are a S/N >3, Angle of Incidence less than 45°, and the ϕ orientation being at least 15° from the earthquake back azimuth, which are similar to Savage et al. (2010). Here we included a cutoff for maximum anisotropy at an unrealistically large anisotropy value (>10% velocity difference) to eliminate erroneous values. As detailed in chapter 2, earthquakes began increasing from 855 in 2015 (Figure 4.11, blue), to 979 in 2016 (Figure 4.11, green), peaking at 1,027 in 2017 (Figure 4.11, red). In 2018 earthquakes in the field began to decrease in number with 300 (Figure 4.11, 2018), decreasing further to 182 in 2019 (Figure 4.11, pink) and 117 in 2020 (Figure 4.11, black circle). The number of earthquakes that met the criteria are consistent with overall numbers of earthquakes in the catalog in each year, indicating that the study pool is representative. Figure 4.12 shows ϕ orientations calculated using the methodology described earlier in section 4.4.

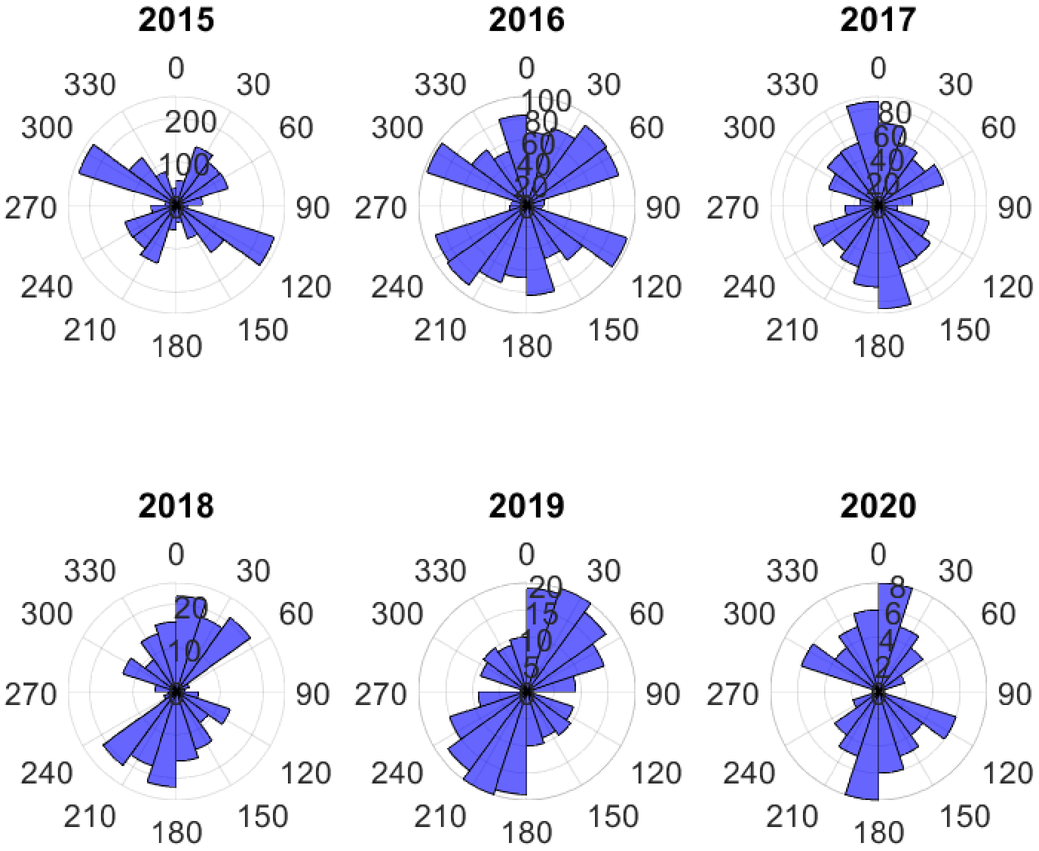
2015 2016 2017

2018 2019 2020

Figure 4-6: Φ orientations of earthquakes used in this study from 2015 to 2020.

In Figure 4.12, the dominant ϕ orientation in 2015 is approximately 300°, in line with optimally oriented fault structures in the region. Nearly orthogonal ϕ orientations (~30-50°) in 2015 also align with fault and fractures (refer to figure 4.3 for potential sources of anisotropy). The year 2016 shows a mixed behavior with structure dominated ϕ orientation trends (~300° and

~30-50°) along with a potentially flipped orientation ~345° (nearly orthogonal to SH-max of 80°). There is a sharp change in the ϕ orientation from 2015 and 2016 compared to 2017, where the ϕ orientation is nearly north-south at ~345°, orthogonal to SH-max. Change in ϕ orientations continues in 2018 and 2019 where dominant orientations shift to ~30°. In 2020, the ϕ orientation is bimodal with one peak at ~0° and a second, smaller peak along structure at ~300°.

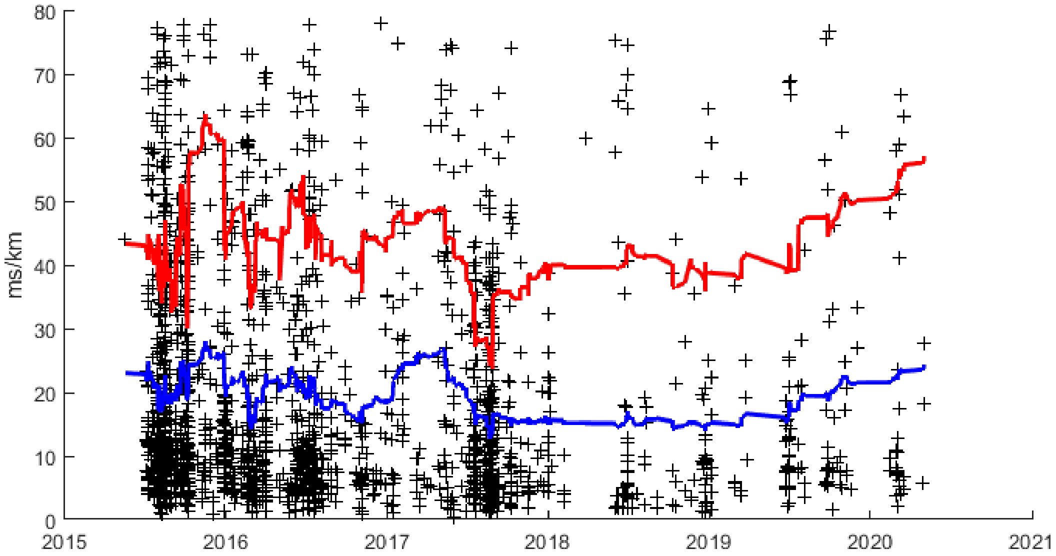

Figure 4-7: Delay time between fast and slow shear wave in millisecond per kilometer.
The moving average (100 samples) is identified (blue) and the 99% moving confidence interval shown (red).

The delay time reflects the difference between the two shear wave velocities over the length of the raypath. The delay time can be interpreted as the amount of anisotropy along that path. Delay times are presented for earthquakes from 2015 to 2020 in Figure 4.13 with the moving average of 100 samples shown in blue and the 99% confidence intervals identified in red. The delay times in these very local events are high and significantly variable.The crust has values ranging from 1.5 –

15 % anistropy (Savage, 1999), which would be as much as 25 ms/km in the US Midcontinent. The graphed average delay times is “hammock-like” in shape with highs in 2015, lows in 2018, and 2020 data growing larger.

Because these events are very local with short raypaths, variability in dt is not surprising. With short raypaths any uncertainty in location of earthquakes is magnified, creating the potential for substantial dt variability. Kansas subsurface geology and structure is not anticipated to be complex and variable enough to generate these changes over such short distances, which supports the idea of location uncertainty playing a large role in this variation. Uncertainty in location is a function of station geometry and spacing which is a problem that would need to be resolved during network design and station deployment. Throughout the study period, minor adjustments were made to network geometry to mitigate this confounding factor as much as possible (see Chapter 5 for a more thorough discussion).

4.5.3 Applying S-wave Anisotropy Analysis to Spatially Constrained Earthquake Clusters

While ϕ and dt analyses of the entire earthquake catalog show consistent trends (Figures 4.12 and 4.13), raypath distance and azimuth effects likely influence the anisotropy results and the interpretation of the observations. Analyzing the temporal anisotropy characteristics of events occurring at nearby locations, ideally on the same fault, eliminates raypath events. Earthquake clusters from chapter 2 were used to identify significant earthquake density for locating earthquakes in the same azimuthal direction from the stations, creating the southern and western earthquake clusters. Clusters were chosen as groups in the same azimuthal direction in order to reduce potential effects of azimuthal anisotropy. Additionally, a distant southern cluster was included for comparative purposes.

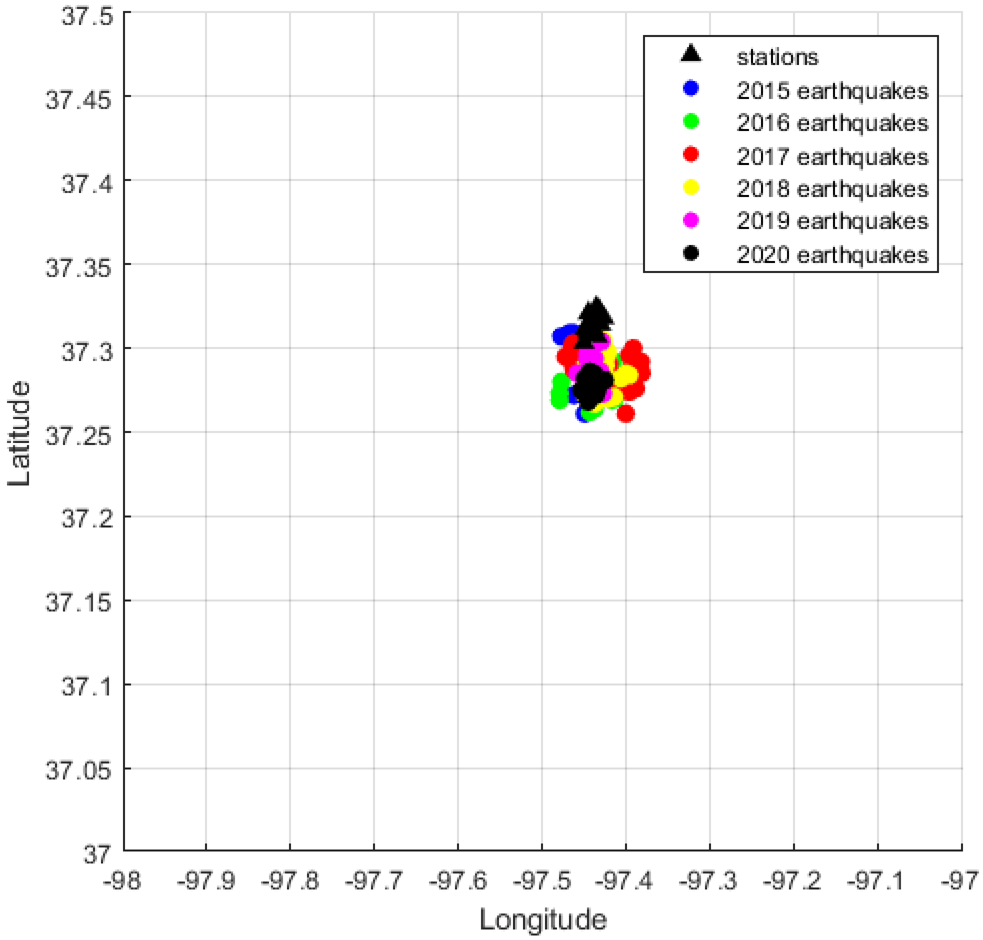

Figure 4.-8: Southern earthquake cluster coded by year of occurrence.
Stations are identified as black triangles.

The southern earthquake cluster (Figure 4.14) contains 590 measurements: 109 in 2015, 143 in 2016, 146 in 2017, 84 in 2018, 55 in 2019, and 53 in 2020. Roughly, these numbers follow the overall seismicity trend observed in the field with increases through 2017 and decreasing thereafter, making this cluster temporally representative.

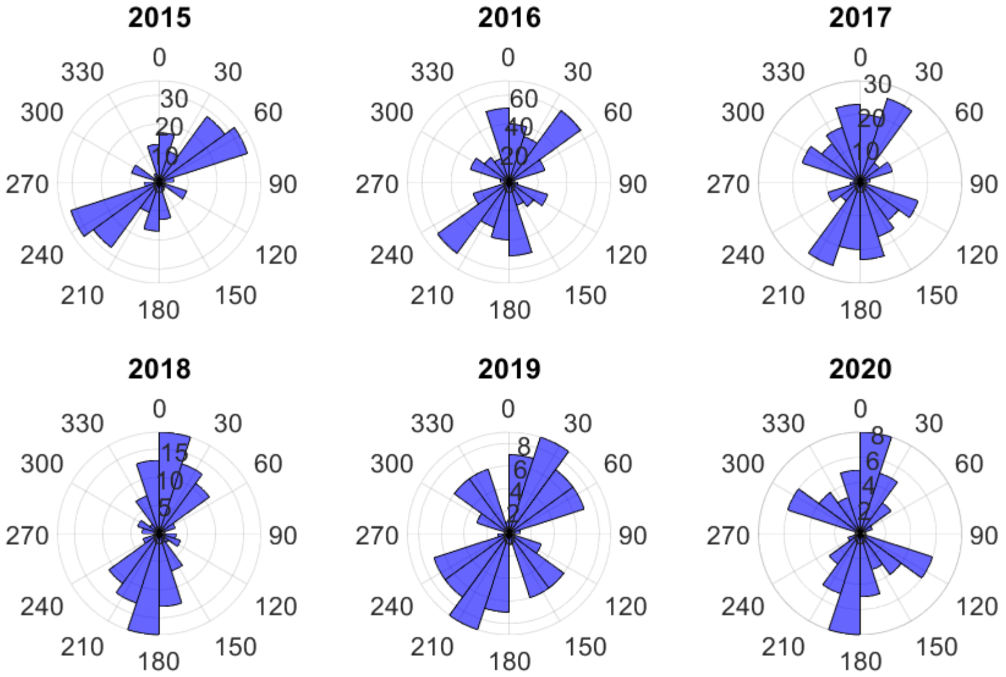

Figure 4-9: Φ orientation of the southern cluster of earthquakes from 2015 to 2020.

The dominant ϕ orientation in the southern earthquake cluster (Figure 4.15) exhibits comparable overall trends with the analysis of the entire catalog (Figure 4.12) with the exception of the absence of a dominant ~300° ϕ in 2015 and 2016 of the entire catalog. The southern cluster ϕ orientation in 2015 exhibits the structure and fracture dominated anisotropy (~30-50°). In 2016 dominant ϕ is along structure (~50°) and also exhibits a north component close to 0°. In 2017 ϕ exhibits a broader range bounded by structure components between 300 and 30°. The southern cluster in years 2018, 2019 and 2020 (figure 4.15) shows similar ϕ orientation trends to the entire catalog analysis (figure 4.12).

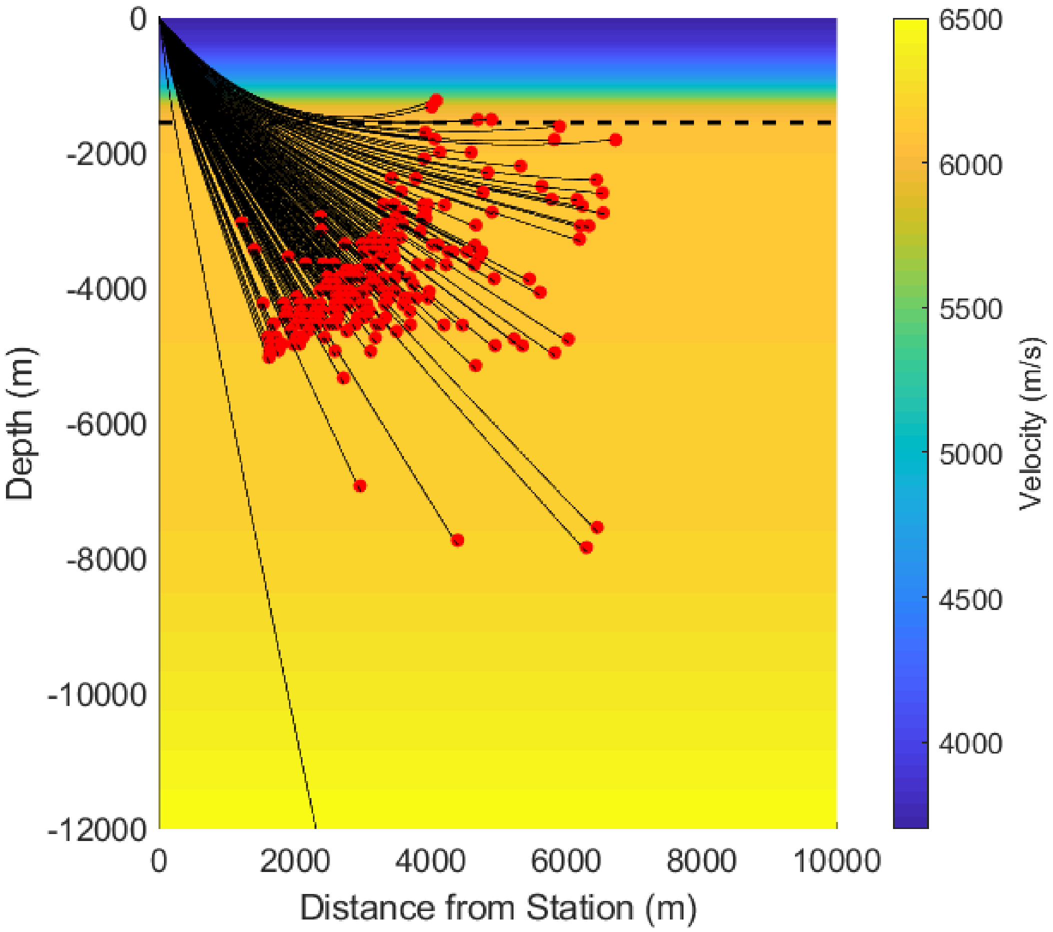

Figure 4-10: Raypaths from the southern earthquake cluster.
The dashed line marks the top of basement. Raytracing velocity model is shown in color.

Earthquakes in the southern cluster occur in the basement and the average raypath is 6.04 km long (Figure 4.16); earthquakes located shallower than the basement (dashed line) and deeper than 8,000 m are likely location errors. Earthquake depths constrained using a converted S to P phase (presented in chapter 3) place all events in the shallow basement.

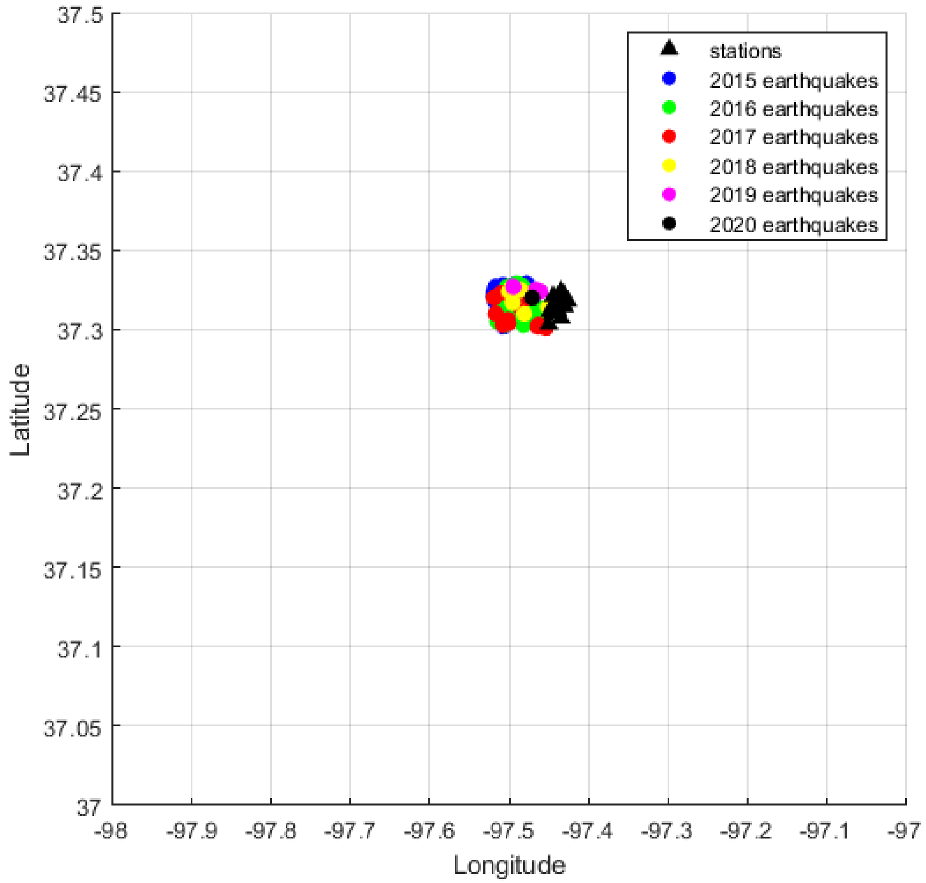

Figure 4-11: The western cluster coded by year of occurrence with stations identified as black triangles.

The western earthquake cluster (Figure 4.17) is composed of 1,200 data points which met the criteria, listed previously, for analysis: 926 in 2015, 204 in 2016, 47 in 2017, 20 in 2018, and 3 in 2019. There was no data in 2020 that met the criteria. These numbers are sufficient for analysis in early years, but are limited in later years (particularly 2018 and 2019) which limits the analysis.

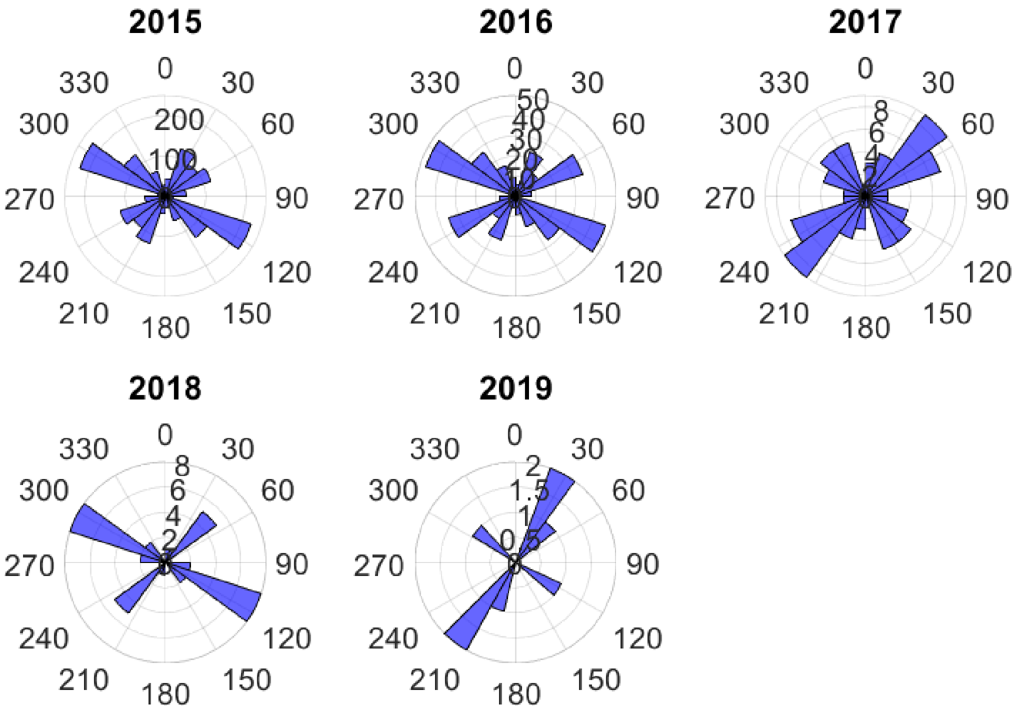

Figure 4-12: The Φ orientations of the western cluster from 2015 to 2019.

In the western earthquake cluster, ϕ orientations in 2015 and 2016 align with the faults optimally oriented for failure and the analysis of the region overall (~300°) (Figure 4.18). In addition, less dominant but still present are ϕ orientations along fractures and faults (~30-50°) as also observed in the southern cluster (Figure 4.15) and the overall earthquake catalog (Figure 4.12). In 2017, the ϕ orientations flip to ~45° along structure. Orientations seen in 2018 and 2019 are likely unreliable due to insufficient data for analysis, yet the few observations available do not deviate from ϕ orientations observed in other years. Because there is no suitable volume of earthquake data in 2020, it is unlikely that further monitoring will generate significant data to assess the active ϕ orientations of the western earthquake cluster.

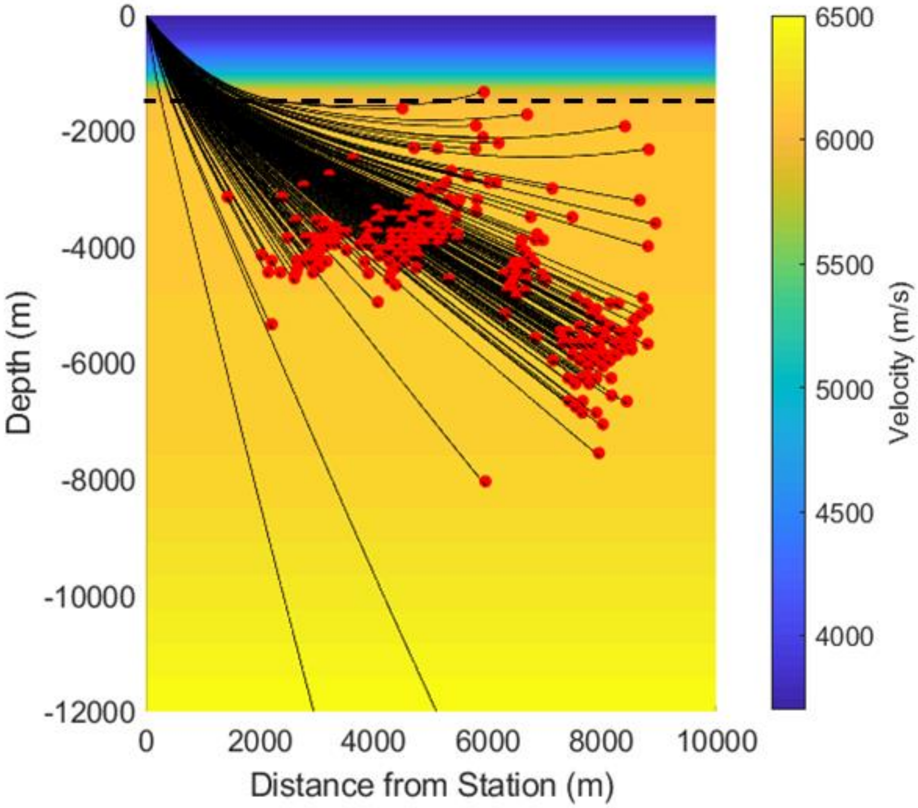

Figure 4-13: Raypaths from the western earthquake cluster.
The dashed line marks the top of basement. Raytracing velocity model is shown in color.

Earthquakes in the western earthquake cluster occurred within the shallow basement with outliers that occurred shallower than the basement or lower than ~8,000 km likely being location errors, as in the southern earthquake cluster. The average raypath of these earthquakes was 7.03 km (Figure 4.19).

Understanding the delay times (dt) and orientations (ϕ) of very local earthquakes can help detect subtle phenomena that can elucidate variations in pore pressure and anisotropy throughout the region. However, very local earthquakes are more strongly affected by location uncertainty. Thus, analyzing a distant cluster could help to increase confidence in successful methodology as well as provide insight on the limitations of interpretation.

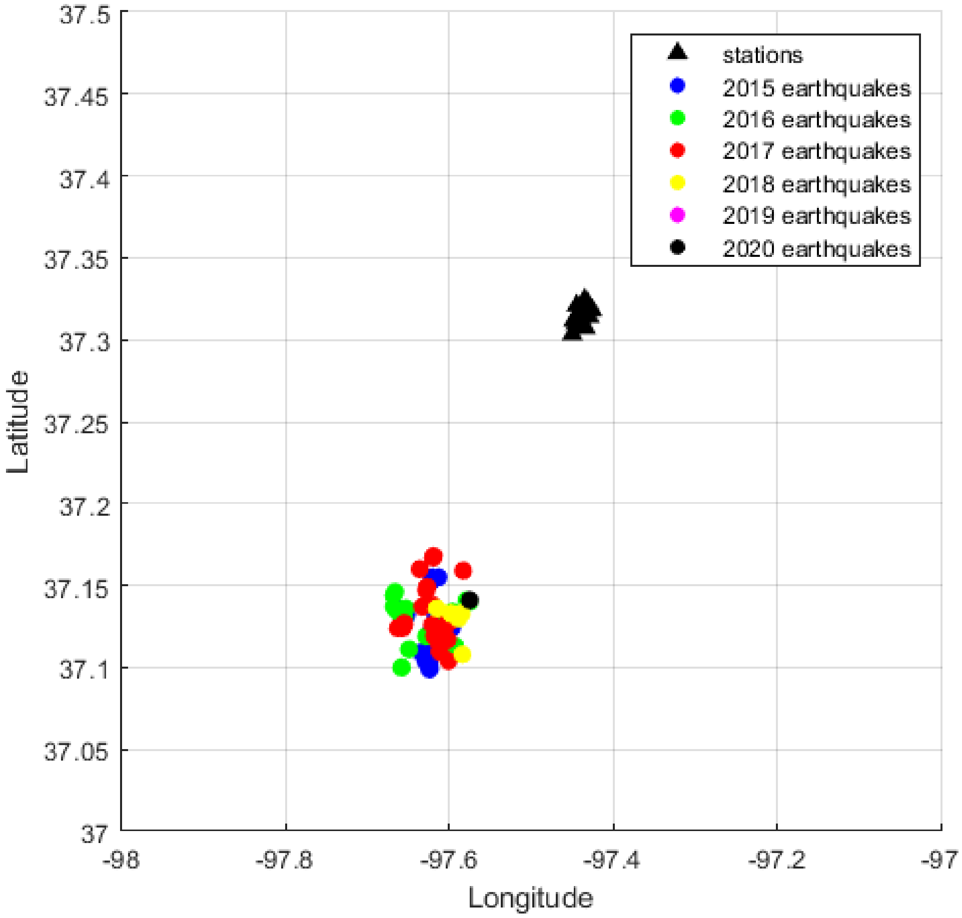

Figure 4-14: Distant southern cluster of earthquakes coded by year of occurrence with stations identified by black triangles.

Earthquakes in this cluster are significantly further (10 times further epicentrally, 3 times further hypocentrally) from the monitoring stations than earthquakes in the southern and western earthquake clusters (Figure 4.20). At this distance, the majority of the raypath travels in the shallow basement, the region of interest for increased pore fluid pressure. Further, at this distance the ray path still arrives less than 35-45 degrees of vertical, which is the limit for ensuring that the shear wave is not affected by surface waves or other near surface effects.

There were 233 measurements in this cluster that met the analysis criteria: 104 in 2015, 47 in 2016, 64 in 2017, 16 in 2018, and 2 in 2020. No data was suitable in 2019. As with the western earthquake cluster, the low number of earthquakes in 2018, 2019, and 2020 makes interpretation less reliable.

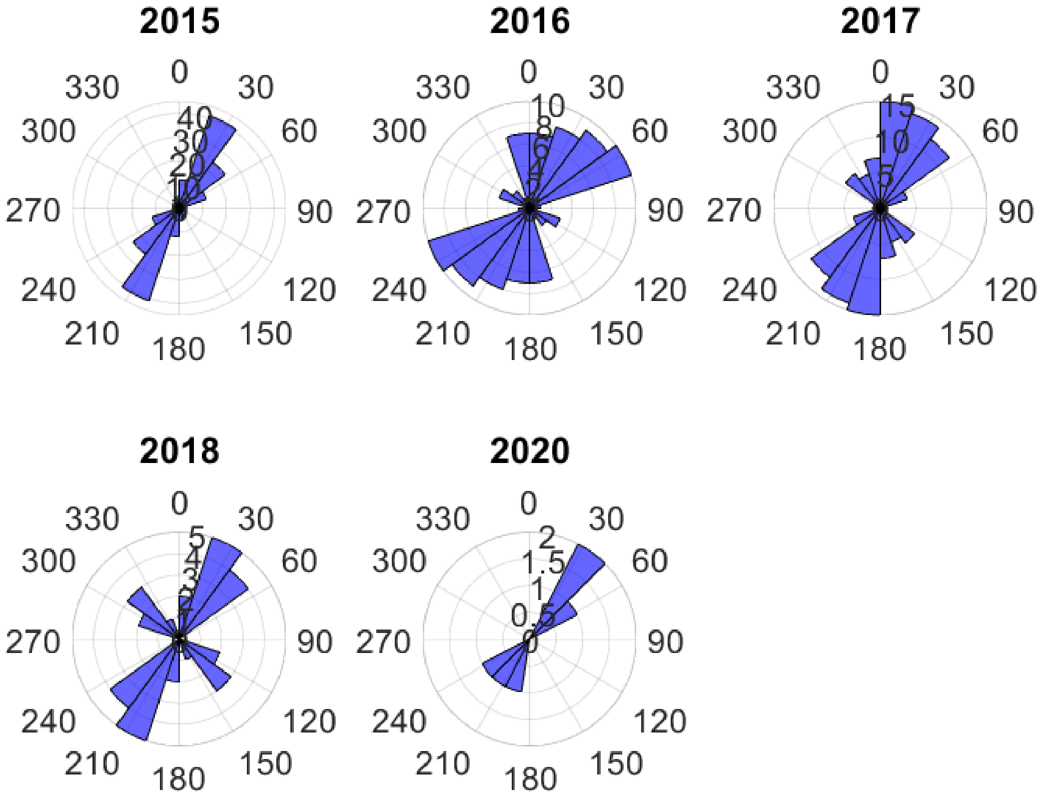

Figure 4-15: Φ orientations of the distant southern cluster shown from 2015 to 2020.

In the distant southern earthquake cluster, ϕ orientations remain consistent through the monitoring window, aligning with the ~30-45 degrees (Figure 4.21) which is inline with structure control. ϕ orientations are in agreement with observations from the southern earthquake cluster

(Figure 4.15) and with the very local events (Figure 4.12). However, in this more distant cluster, there were no earthquakes available for analysis in 2019 and only 2 available in 2020.

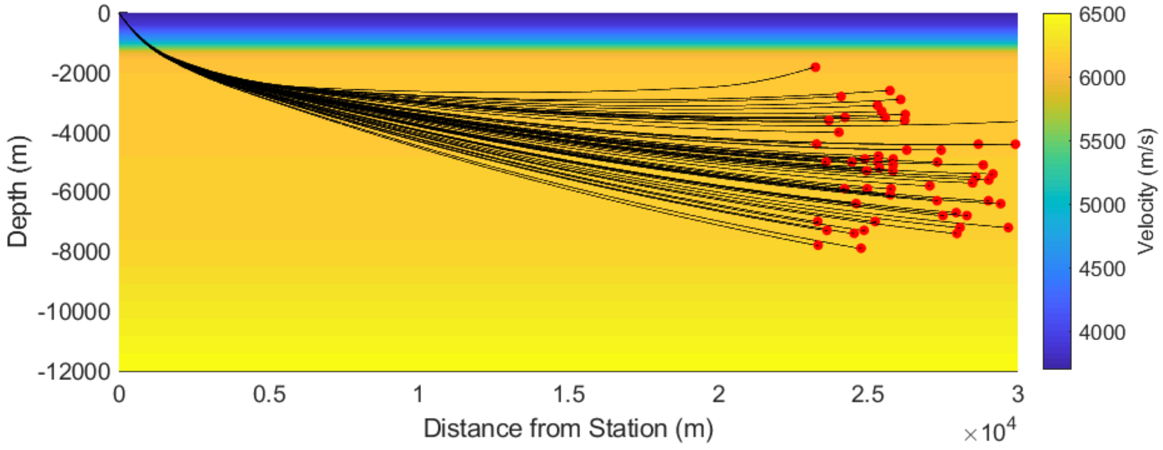

Figure 4-16: Raytracing of events in the distant southern cluster showing the raypaths and the velocity model.

Raypaths of earthquakes in the distant southern earthquake cluster are approximately 4 times the length of the very local earthquakes (Figure 4.22). The raypaths in this cluster are an average of 26.27 km. These raypaths are primarily traveling in the shallow basement (Figure 4.22), the key unit of interest for this study due to pore pressure increases in this unit.

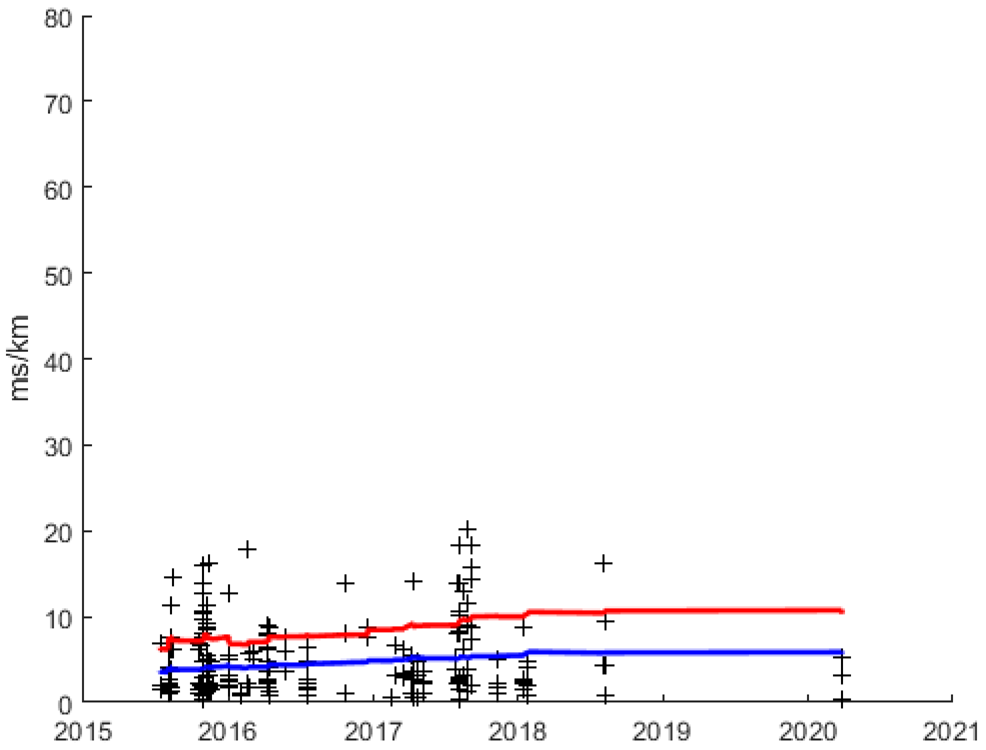

Figure 4-17: Delay times for the distant southern cluster with the 99% confidence interval shown in red (maximum) and blue (minimum).

Delay times in the distant southern earthquake cluster are significantly lower than delay times for the very local events (Figure 4.13) and exhibit significantly less variability. The very local earthquakes had unstable delay times, possibly in part due to instability of locations having an outsized effect on the length of the raypath. With these raypaths being significantly longer, this effect is minimized, increasing the stability of this data. This indicates that the data and the analysis is stable and working correctly. The delay time in the distant southern earthquake cluster is consistent with other studies worldwide with ~2-3% anisotropy as calculated from shear-wave velocity anisotropy.

4.6 Discussion

Earthquakes evaluated here are all very local to the Wellington Earthquake Monitoring Network. These were chosen in order to reduce uncertainty in the raypath azimuth as well as limiting potential effects of high angle of incidence. Because shear wave splits are highly dependent on raypath, significant variation between the paths can obfuscate results. The earthquakes included in the full analysis are not azimuthally constrained, which may introduce azimuthal anisotropy effects. This is mitigated by looking at directional clusters to the south and west, although this reduces the total number of observations.

In the full data set we identified the dominant ϕ orientations in all years with 2015 and 2016 having distinctly different dominant orientations when compared to 2017, 2018, 2019, and 2019 (Figure 4.12). Early data (2015-2016) aligns with faults optimally oriented for failure which are reactivating in the local area. Earthquakes detected in this catalog are occuring on these faults, so it is possible that during this time the anisotrpy is dominated by these fault networks. In addtion, 2016 shows a wider range of ϕ orientations which allign with potential sources of anisotropy (Figure 4.3) and are also orthogonal to SH_{max}. This wider range, also referred to as mixed ϕ response, may represent a period of transitioning between sources of dominant anisotropy due to change in subsurface pore fluid pressure. In 2017, dominant ϕ orientations are distinctly different than the two previous years (Figure 4.3), oriented nearly 90°away from the maximum horizontal stress direction, nearly north-south. This markedly change in ϕ orientations is interpreted as a result of pore pressure changes causing ϕ flips as the peak of the pore pressure front has reached the region. These flips most probably indicate that the raypath has traveled through rock that has undergone a critical change in pore fluid pressure (Crampin et al., 2002). In 2018-2020 φ is aligned more closely with the open fracture system (Schwab et al., 2017). Both are equally plausible and are likely not indistinguishable, but it is believed that a larger pressure change would be necessary to cause a flip away from the maximum horizontal stress orientation.

In the early data (2015-2016) delay time was high, but showed changes through time with lower values in 2018. Delay times appear to increase in later data (2019-2020), indicating a return to the 2015 levels. Flips in φ are often seen with reduced delay times, as the faster velocity orientation becomes the slower velocity, creating a negative delay time as compared to the original velocity orientation. However, given the amount of spread in the data, it is unclear if these values are physically constrained or rather an effect of unstable delay times, caused by location inaccuracy.

Change in ϕ orientation is clear in both tightly spaced earthquake clusters to the south and west of the monitoring network (Figures 4.15 and 4.18 respectively). In the tectonically stable US midcontinent, over the time period of this study, anisotropy change may be explained by the regional rise and fall of pore fluid pressure, due to the close temporal correlation. The cluster that shows no change is the distant cluster to the south that shows orientations north-south in all years (Figure 4.21). This orientation is unexpected based on the horizontal maximum stress at 77 degrees (Schwab et al., 2017). This could indicate this cluster is showing increased fluid pressure changes in all years of analysis, which is reasonable given the pressure increase is stronger in the south and presumed to move northward over time.

These interpretations are in line with our previous studies and modeling in the region. Our earthquake catalog identifies a northward progression of earthquakes. These results support a changing pressure gradient across Sumner County, where pressure increases occurred earlier in the south and now appear to be moving northward. The pressure increases in the north seem to be smaller than those observed at the height of pressure increases in the south, in line with models (Langenbruch et al., 2018; Ansari et al., 2019) of pore fluid pressure movement through the Arbuckle. This is in line with the hypothesis that the increased pore fluid pressure is the result of high volumes of wastewater injection in Oklahoma, south of our earthquake monitoring area.

Monitoring for changes in shear-wave splitting parameters may prove to be a useful tool for gaining *in situ* understanding of pressure changes in the shallow basement. Thus, we conclude that the use of passive seismic networks to monitor for anisotropic changes can be a valuable tool for identifying risk from wastewater injection.

4.7 Conclusion

A large body of research (Angerer et al., 2000; Crampin et al., 2002; Crampin and Chastin, 2003) has demonstrated that shear wave anisotropy is sensitive to pressure changes, but little is known about fluid injection-related pressure changes, particularly injections distant to the site of interest. In south-central Kansas, very small changes in pore fluid pressure are inducing earthquakes. Temporal analysis of S-wave anisotropy at Wellington field shows changes in alignment of shear waves with factures or faults and SH_{max}. The only temporally coincident change in the subsurface is pore fluid pressure. Because the region is not very compressive, indicated by the mix of strike-slip and normal faulting (Alt and Zoback, 2017; Schwab et al., 2017) the stress induced anisotropy can be very weak, allowing local fault or fracture anisotropy to dominate the anisotropic effects. Temporal changes in anisotropy identified in south-central Kansas largely appear to be caused by changing in alignment from one source of anisotropy to another source following changes in pore fluid pressure.

Chapter 5 Designing monitoring networks for local earthquakes

5.1 Abstract

Seismic networks are essential for monitoring local earthquakes in connection to industrial activities, including wastewater injection and CO_2 sequestration. Because these networks are typically deployed for short periods of time at specific sites, it is beneficial to develop best practices for efficient and effective installation and monitoring. Such standards are available for regional earthquake and microseismic monitoring, but not readily available for local scale (10s of km scale) monitoring. Here we present a new model for designing these local networks. Key parameters for establishing a network are available monitoring station locations, site noise, and site utility. This new model utilizes available parameters and models earthquake detectability based on minimum locatable magnitude events from a similar deployment. Using the model, a map of minimum locatable events can be created to design network monitoring locations. Also presented is a workflow chart for future local seismic network design and installation. Herein, a network was established at the Patterson and Hartland Oil Fields in western Kansas in association with a US Department of Energy CarbonSAFE carbon capture and sequestration research project. We employed observations from an analogue local network, the Wellington Earthquake Monitoring Network in south-central Kansas, to assess site noise and estimate earthquake detection thresholds for the Patterson and Hartland fields. Noise from oil production facilities was evaluated, concluding that oil lease sites are suitable for monitoring small local earthquakes (M1-M3). Using the new model, the network was designed to have a magnitude of completeness of M1 while using station locations on existing field operator leases. Fifteen months of continuous network operation validates the new model, demonstrates reliable

and efficient local earthquake monitoring and provides best practices recommendations for similar operations.

5.2 Introduction

Anthropogenic activities are known to induce local earthquakes. In recent years the injection of fluids in the subsurface, such as the disposal of wastewater from industrial operations, enhanced geothermal power generation and CO_2 geologic storage, have been associated with the triggering of earthquakes, but many of these earthquakes are not felt (Evans, 1966; Rutqvist, 2012; Kim, 2013). Seismic networks are routinely used to monitor injection sites for assessing and mitigating earthquake risk, but there is a gap in the published literature on best practices and case studies of establishing local earthquake monitoring. While there are published resources on regional network setup (Bormann, 2012; Kraft et al., 2013; Tiira et al., 2016) and microseismic monitoring (Warpinski 2009; Maxwell et al., 2010), literature is sparse on local seismicity monitoring of a few km to 10s of km distances as well as short term monitoring. Here we use a case study in Kansas to present planning considerations and implementation steps that can serve as a road map for local earthquake monitoring networks. This work is motivated by the evaluation of a west Kansas site for carbon capture and sequestration (CCS) and it can be implemented at other local earthquake monitoring sites.

Injection of CO_2 in deep geologic formations for enhanced oil recovery has a well-established and proven history, making adoption of CCS as an industry wide practice more likely (Herzog, 2011). However, there are significant challenges that must be addressed prior to the commercial utilization of CCS. One major concern is the identification of secure, long-term geological storage for CO_2. The Integrated Midcontinent Stacked Storage Carbon Hub (IMSCS HUB) led by Battelle Memorial Institute, University of Kansas, Kansas Geological Survey, and

Energy and Environmental Research Center (IMSCS HUB) builds on lessons learned from the US Department of Energy (DOE) National Energy Technology Laboratory's (NETL) Regional Carbon Sequestration Partnerships (RCSPs). This program is the first large-scale project for the midcontinent and represents an important step forward in storage scale, exceeding the 50 million tonne (Mt) safe storage objective. Of primary importance to a secure geologic storage site is low natural seismicity and low likelihood of triggering injection induced earthquakes that can disrupt commercial and residential activity near the sequestration site.

To establish the history of seismicity of an area, most CCS applicants will rely on USGS data in the United States, or potentially State and other government data; however, if the available regional network does not provide sufficient local coverage, it is possible that projects may be asked to provide early monitoring. If this review concludes that there is a history of seismicity near the injection site, or potential for seismicity, a passive earthquake monitoring network and an emergency and remedial response plan will be necessary. Passive monitoring is considered by the EPA as a method to reduce and manage risks from CO_2 injections (EPA, Office of Water). The EPA is concerned about earthquakes that exceed a M1, so networks should be designed with this magnitude threshold in mind. In addition, projects seeking permitting for CCS must prove financial responsibility for the life of the project. Continuous earthquake monitoring is a substantial undertaking that may prevent the adoption of CCS unless an economical model of seismic monitoring is developed.

The Kansas Geologic Survey, in partnership with the Department of Energy, Berexco LLC, and other stake holders identified regions throughout Kansas that might be suitable for long term sequestration of CO_2 (Watney at al., 2015). The presence of the Arbuckle Group, a thick (~300 m), regionally prevalent, highly permeable dolomite aquifer, deeply seated over granitic basement rocks offers a favorable setting for CCS operations. The Patterson and Hartland Oil Fields in west Kansas (Figure 5.1) were identified as prime candidates due to existing oil extracting operations, available facilities and operational expertise by the project industrial partner, Berexco LLC (Holubnyak et al., 2018). Well log and 3D seismic information is available for the two fields, in addition to what is already known about the geology of the region. Three potential injection formations, the Osage, Viola, and Arbuckle (Figure 5.2), made of limestone, dolomite, and dolomite respectively, spread over 130 km^2, are good CO_2 storage candidates (Holubnyak et al., 2020). The installation of a local earthquake monitoring network at Patterson and Hartland fields was undertaken as part of the assessment of the suitability of the two oil fields for long-term geologic storage of CO_2.

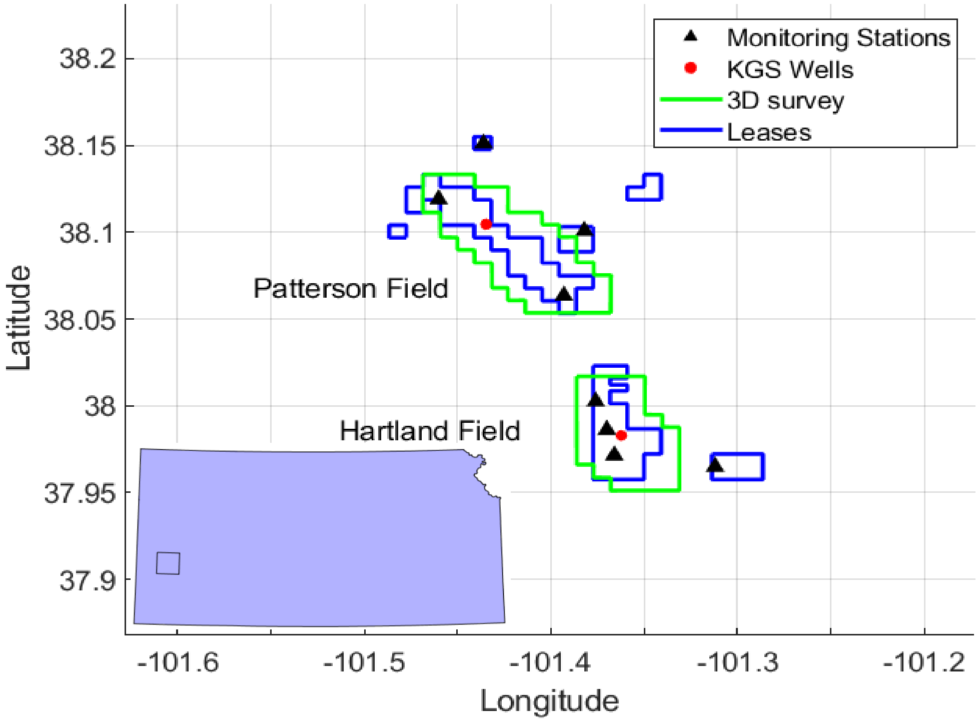

Figure 5-1: Location map of the Patterson and Hartland fields in Kearny County, KS.
Berexco leases are shown in blue. Two new wells (shown in red) were drilled for reservoir characterization associated with potential CCS. The local earthquake monitoring network station locations are shown as black triangles. 3D seismic surveys are outlined in green, showing the approximate area of interest for monitoring. Inset map of Kansas shows the area of interest in the black square.

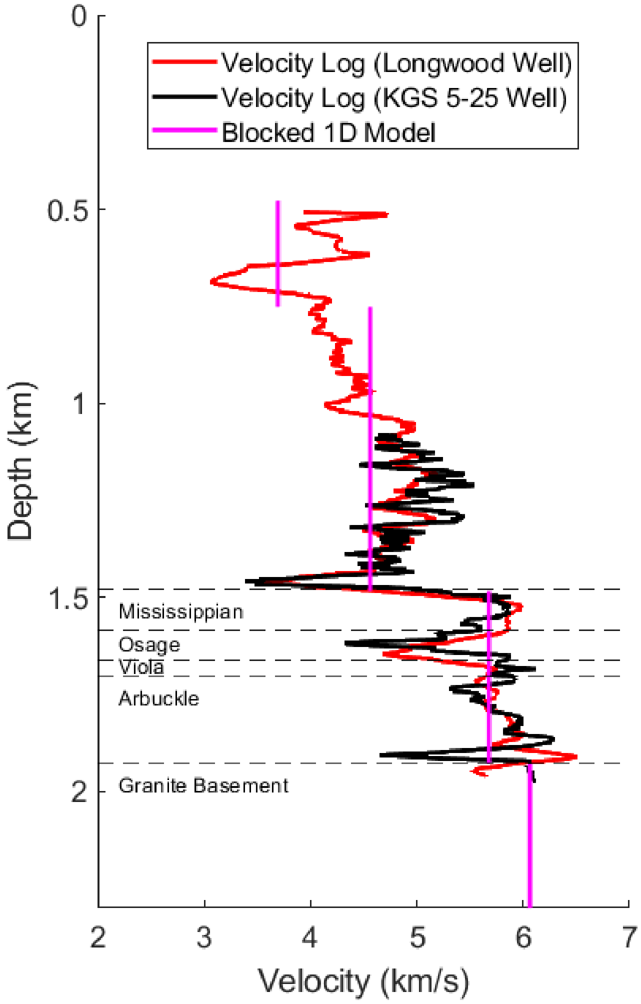

Figure 5-2: Velocity model used for local earthquake location.
Magenta is the blocked 1D model used to nearly 2km depth obtained from well data. The red curve is a 30m (100ft) averaged velocity from a sonic log in the Longwood well in Hartland field and the black is 30m (100ft) averaged velocity from a sonic log in the KGS 5-25 well in the Patterson field.\

5.3 Background

In designing a seismic network, many diverse parameters must be considered. The geographic region of interest, as well as the seismo-geological conditions, will drive the fundamental design. Surface topography and accessibility will be defining factors. Often less considered, seismic noise sources in the region, evaluated herein, will affect data quality and final conclusions; understanding the risks that seismic noise poses to a field site is essential in designing a network that can overcome these shortcomings. Data transmission options, electric power access (including solar power availability), and land ownership will have a significant impact on network design. As a secondary consideration, climatic conditions may need to be evaluated, but no special considerations had to be taken here. Finally, this all must be balanced with the cost of the network. The New Manual of Seismological Observatory Practice (Bormann, 2012) provides comprehensive information in designing regional networks but can't be thoroughly followed due to stations in local networks being in much closer proximity and often deployed for much shorter periods of time than stations in regional networks.

Establishing the network requires an understanding of the minimum number of stations needed for effective monitoring and the approximate locations available for station installations. This information is going to be strongly affected by the investigative goals of the project as well as project funding, both of which must be well established prior to network design. Once established, the final seismic station locations can be chosen. Because the goals, and network design to achieve those goals, will be strongly affected by the seismicity and geology of the region, it is important that set up be established by someone familiar with the region and equipment (Bormann, 2012).

In many cases, for monitoring near a CO_2 sequestration site, partnering with an oil and gas operator can allow seismic stations to be installed in the lease areas of the operator. If there is no partner with leases in the area, then separate leases or agreements with private landowners or government entities may be needed. However, partnering with operators is extremely beneficial, as they have personnel in the field regularly who can help maintain equipment, and it reduces the need to obtain permissions from multiple landowners separately. Yet, while avoiding land access hurdles, this approach limits available station locations to that operators' acreage (Figure 5.1). It can also restrict site options to very noisy locations near oil and gas operations. Here we show that although these sites are not optimally quiet, they are still able to provide quality earthquake monitoring in the field area.

Road access will affect where within the available lease's stations can be placed. Station components including seismometers, batteries and solar panels can weigh well over 100 lbs. (45 Kg) even for temporary deployments. Placements near roads makes deployment more logistically feasible but increases risks due to visibility and traffic noise. One strategy is to choose sites on oil and gas operator's access roads which are rarely traveled, reducing traffic noise and reducing public interactions with equipment. However, oil and gas access roads have well site noise.

Telemetry-based deployments in which cellular service is used to transmit data from the field to the office site are often simpler. Telemetry-based networks can be monitored for station health remotely, preventing the need for service runs. Cellular access also prevents the need from regular trips to the field for data collection. Cellular service coverage can be verified during early site evaluations or through discussions with site operators. Major carrier websites are also a resource for identifying zones with cellular coverage.

Temporary deployment stations are designed to run on deep-cycle marine batteries and solar panels, preventing the need for on-site power access. This set up is efficient and effective for temporary usage. However, the most identifiable portion of the network set up is the large solar panel; in areas where stations may draw unwanted notice, batteries may be the best choice. For long term networks, integrating into the well site a power system would provide reliable, long term options.

5.4 Methods

5.4.1 Establishing the West Kansas Patterson and Hartland Network

In many local networks, especially in Kansas, seismo-geological conditions will be reasonably consistent throughout the study site; however, conditions between study sites may pose comparative confounders. For the networks here, the geology is characterized by nearly horizontal ~2 km thick sedimentary strata overlying granitic basement (Merriam, 1963), therefore the conditions for limited subsurface velocity anomalies are the same throughout the study area. Although faults are seen in 3D seismic data, there are no significant velocity anomalies to distort a 1D velocity model significantly (Figure 5.2). There is one major fault that bounds the western edge of the fields, but its throw is most significant in deeper units of similar velocity (Mississippian and lower) and would not affect earthquake locations significantly, as earthquakes were expected to be in these units and deeper in the basement.

Here, we use eight seismometers on loan from the Incorporated Research Institutions for Seismology (IRIS) and Portable Array Seismic Studies of the Continental Lithosphere (PASSCAL). The Sercel L-22 short period seismometer is optimal for local earthquakes with a frequency range of 1-100 Hz.

For the Patterson project, the KGS partnered with Berexco, LLC, enabling the placement of stations on Berexco well site leases (Figure 5.1). Access roads were already built on the well sites and were used for accessing station sites. The Patterson and Hartland Fields are well within a major cellular provider network which was used for telemetry. Stations were powered by deep cycle marine batteries and a single solar panel.

5.4.2 Selecting Station Spacing

After available station locations are identified, the geometrical design and spacing of the network will depend mostly on the size of the area being monitored, the number of stations available, and the anticipated depth of earthquakes for the local site. Locating earthquake depths is more accurate when the distance between the earthquake epicenter and the closest station is less than the focal depth (Gomberg et al., 1990). At Patterson and Hartland fields, sedimentary units suitable for storage of CO_2 are between 1 and 2 km depth, and it can be assumed that earthquakes would occur near the injection intervals and in the underlying shallow basement rocks (Figure 5.2). Therefore, stations should be spaced approximately twice the focal depth for the most accurate depth determination so that a station is always within one focal depth of the earthquake. At the Patterson project, spacing of approximately 4 km will provide the most accurate depth assessments, with the limitation that stations can only be placed on available leases (Figure 5.1).

Seismic networks will return accurate epicenter locations within the seismic network but are unlikely to yield data on earthquakes occurring outside of the network without large location errors. In cases where the azimuthal gap between stations, with respect to the epicenter, exceeds 180^o, large errors should be expected (Bormann, 2012).

James et al., (1969) used a least-squares inversion to solve for hypocenter solutions and concluded that eight earthquake signal arrival recordings were necessary for accurate event location determination. Ideally, several of these arrivals would be s-waves; location accuracy generally increases with the number of S waves, limited by the ability of the picker. S wave picks are among the most important steps in earthquake location; “bad” picks can create stable, yet inaccurate, results (Chatelain, 1980).

Using both P and S wave arrivals can help to reduce uncertainty in hypocentral location (Gomberg et al., 1990; Bondar et al., 2004). Less dense networks directly impact the detection abilities of the network due to attenuation and potentially poorly constrained locations (Bormann, 2012). These issues are exacerbated when there are fewer stations as each station will be required for earthquake detection and well constrained locations. In these networks, recording S waves is of particular importance to improve constraint of the depth measurement (Gomberg et al., 1990). Recording S and P phases at a close station significantly reduces the trade-off between focal depth and origin time (Gomberg et al., 1990).

5.4.3 Estimating Detection Thresholds

For the Patterson project presented here, the geometry of the network is primarily controlled by the limited leases available, which is likely to be common when partnering with industry groups. Thus, the more controllable limiting factor is site noise. Site noise can be identified from some noise examples shown in Figure 5.3. In our study the most common source of noise is pump jack noise from oil extraction operations. Using operator leases requires stations to be in close proximity to these noise sources, limiting the lowest detection magnitude level of earthquakes. However, multi-year local monitoring at another active oil field at Wellington KS (Watney, 2014) demonstrates that at these noisy sites local networks are capable of detecting Mw 0.4 earthquakes (Nolte et al., 2017; Nolte and Tsoflias, 2019). Local site noise is significantly lower amplitude than the Mw 1.2 earthquake shown in Figure 5.3a. Thunderstorms, which are common in the area, can be larger amplitude noise sources (Figure 5.3b) but the waveforms are distinctly different than earthquake signals. Vehicles are not typically a source of seismic noise that confounds data because they do not produce a strong enough signal to be seen on multiple stations; by requiring a signal to be identified on three stations, localized sources of energy can be eliminated. Trains can create noise on all stations, but the long-time duration differentiates them easily from local earthquakes, although they could limit earthquake detection by increasing background noise.

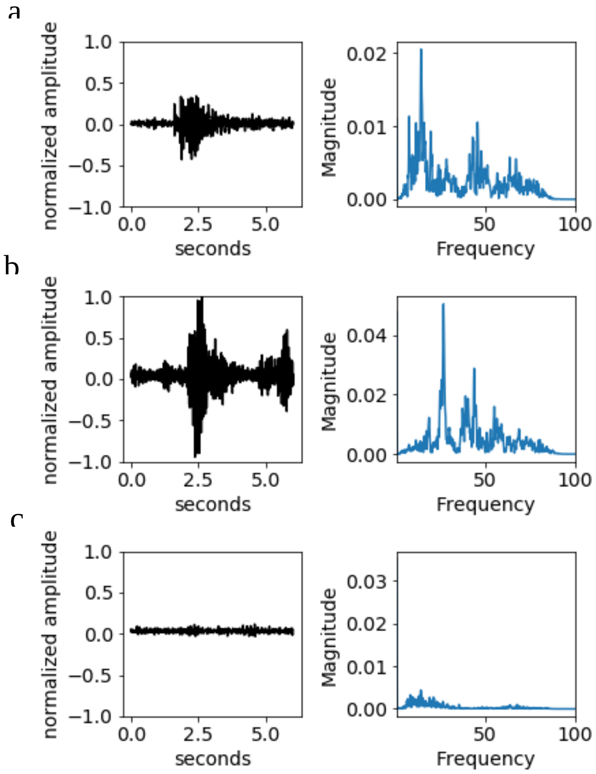

Figure 5-3: Sample seismic records and corresponding spectra from an analogue local network at Wellington Oil Field, south Kansas.

Station noise is easily identifiable when compared to the pattern of an earthquake. a) seismogram of an Mw 1.2 earthquake located less than 2 km from the recording stations. b) Recording of thunder from a storm. c) Oil field pump jack noise with a characteristic lower amplitude and low frequency content.

Of paramount importance to a new network installation is estimating the minimum detectable magnitude, which can be challenging due to the lack of prior observations. A multitude of studies have been performed using the sensitivity of the seismometers along with estimates of ground motion (Joyner and Boore, 1981; McNamara and Buland, 2004; Tiira et al., 2016). This methodology could be applied here, with high background noise. We present a new approach incorporating observations from an analogue site. A local network with similar station installation and subsurface conditions has been operating at Wellington Oil Field in southern Kansas for nearly five years, with over 4,000 located earthquakes (Nolte et al., 2017; Nolte and Tsoflias, 2019). Here we use the Wellington earthquake catalog to estimate the future capabilities of a new local network installation at the Patterson/Hartland network. This new applied field data approach can more accurately predict the site noise due to proximity to oil production since conditions at the two fields are comparable. From this catalog in southern Kansas, a magnitude vs distance relationship is calculated (Figure 5.4). Here we use the simplified ground motion equation of Tiira et al., (2016).

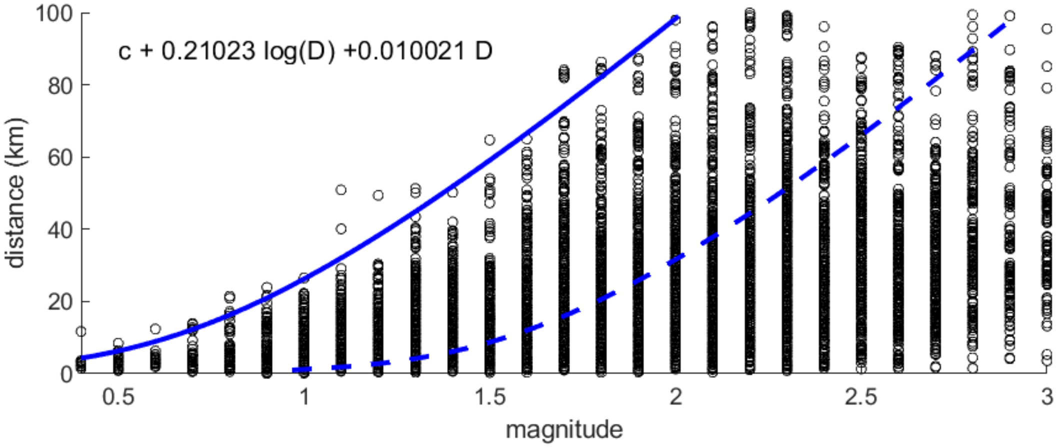

Figure 5-4: Graph showing the magnitude vs distance of earthquakes from the Wellington earthquake catalog. The dashed line shows the best fit of the simplified ground motion equation (eq. 1) to the approximately 4000 events. The solid line shows the simplified ground motion equation adjusted to align with the limit of minimum magnitudes at each distance, best estimating the minimum magnitude vs distance relationship.

The Wellington Monitoring Network has a magnitude of completion of Mw 1.6 for Sumner County (Nolte et al., 2017; Nolte and Tsoflias, 2019). All earthquakes for which P and S arrivals are recorded are shown in Figure 5.4, with their magnitude plotted against their distance (km) from the seismic station that recorded the earthquake. Here we used distance as epicentral distance, following the methodology of Tiira et al., (2016), since the expected earthquakes would be very shallow and exhibit little difference between epicentral and hypocentral distance. The simplified ground motion equation (Joyner and Boore, 1981; Liu and Tsai, 2005; Tiira et al., 2016), solved for magnitude is fitted, assuming all sites are geologically similar. The equation:

$$M=b*\log(D)+a*D + c \qquad (1)$$

is represented by the dashed line in Figure 5.4. C represents the baseline correction applied to the simplified ground motion equation. Both a and b are coefficients of anelastic attenuation and geometrical spreading, and D is the epicentral distance (Tiira et al., 2016).

However, the actual magnitude of completeness diverges significantly from this best fit line (Figure 5.4), because the best fit is for all earthquakes, not the minimum magnitude detectable at a given distance. In order to estimate the minimum detectable earthquakes in this region manual coefficient adjustments were made to equation 1 to fit the minimum magnitude of detection at a given distance. This was done by best approximating the left limit of the data, which corresponds to the smallest earthquakes at each distance.

The adjusted best fit line of the minimum magnitude of detection (solid line) is a conservative estimate of magnitude of completeness in the 5 to 35 km range, which is the range we are interested in monitoring for very local earthquakes around a potential fluid injection site. This metric is a conservative measure of the minimum magnitude of detection. There are earthquakes that fall above the fit line (solid line), indicating that this adjusted equation would predict similar seismic events as undetectable; however, they are clearly detectable since they are in the catalog. Using a conservative equation ensures that the network will perform as predicted, and no earthquakes of a certain magnitude and distance will be missed based on Figure 5.4. At distances less than 3 km the best fit equation used shows earthquakes of size less than Mw 0.4. However, no earthquake smaller than M_w 0.4 has been detected with the similar station set up and noise level at Wellington field, so M_w 0.4 has been fixed to the minimum detectable magnitude of the Patterson monitoring network.

Because the concern is CO_2 injection-induced earthquakes, the area of interest will be located near the injection wells. With the goal of having an overall magnitude of completeness of Mw 1, a network that encompassed the entire area around wells was needed. Single-well induced seismicity occurs near the wellbore (Kim, 2013; Evans, 1966). CO_2 sequestration should have similar types of seismic activity, considering there is no other large-scale fluid injection in the region.

A magnitude of completeness M_w 1 allows for the use of surface stations, fewer seismometers, and noisier sites, significantly reducing the costs compared to borehole earthquake monitoring. An M_w 1 can be detected at nearly 30 km from a station (Figure 5.4). A magnitude of completeness of M_w 1 will allow for the detection of earthquakes well below the magnitude that is usually felt at the surface (~M3) while also expanding the field sites in which these methods can be utilized.

Using the estimated detection thresholds and the proposed station locations we estimate regions of minimum magnitude earthquake detection at Patterson and Hartland fields (Figure 5.5). Three stations are necessary for an earthquake to be detected. A grid search at 50 m intervals is used to find the distance from the third closest station (Tiira et al., 2016). This is performed to ensure that the earthquake will be detectable on a minimum of three stations and will be locatable. Location accuracy is best in the region encompassed by the stations and it degrades severely when the azimuthal gap exceeds 180 degrees (Gomberg et al., 1990; Kim, 2013; Tiira et al., 2016). Station locations were optimized within existing oil and gas leases; while an ideal configuration may be created purely based on geographical location, the practicality of available leases in the geographically ideal regions is low.

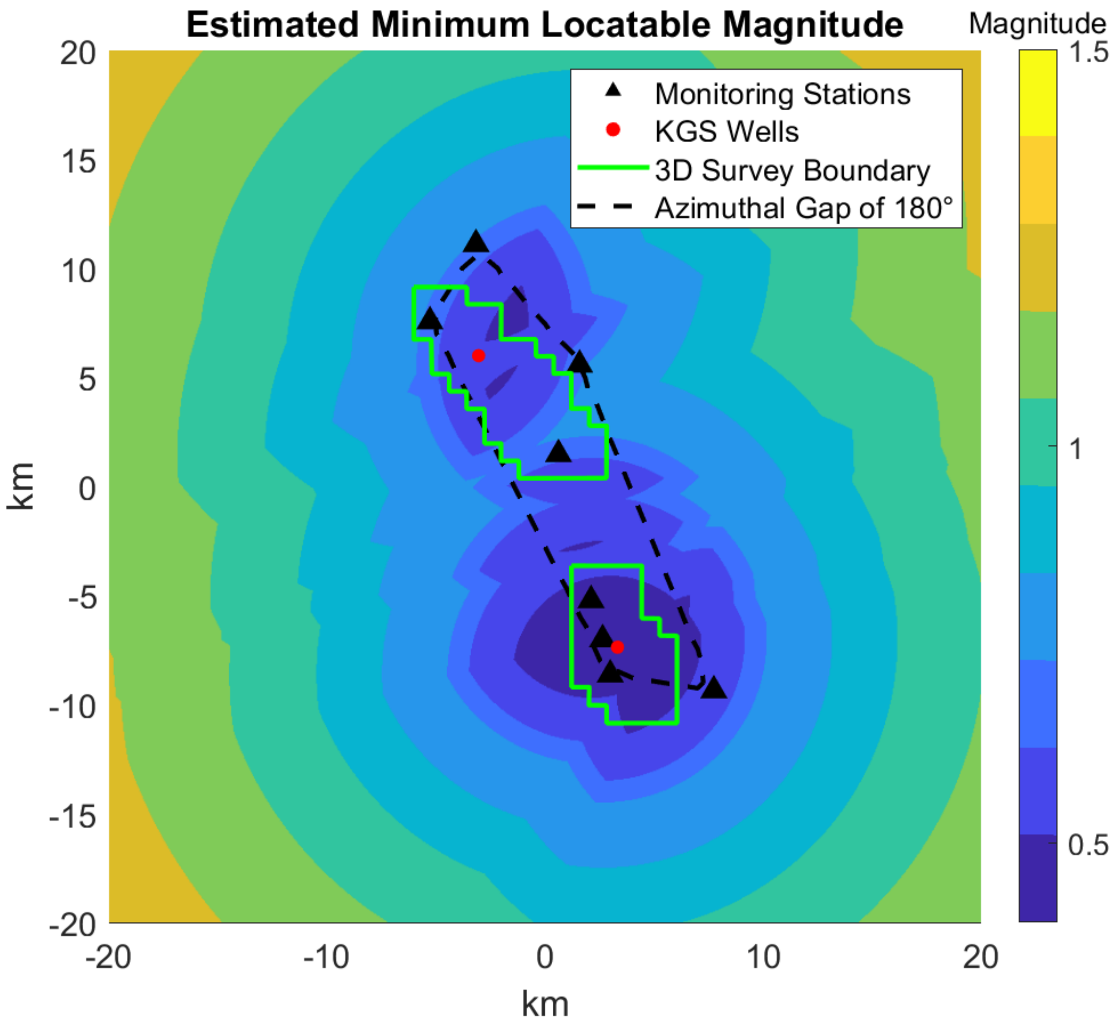

Figure 5-5: Estimates of minimum locatable magnitudes surrounding the Patterson and Hartland Field Monitoring Network.
The color shows the magnitude of detection every 50m, using three stations, so that the earthquake is locatable. The dashed line shows the region where the azimuthal gap between stations is less than 180°. The green outlines show the area of 3D seismic, which is also the area of interest for the study.

5.4.5 Data Handling

Telemetered data is directed to a server maintained at the KGS, but a local computer could be used in cases where manual data collection is utilized. Seismometers transfer data in Reftek format, and it is converted to miniseed format for processing and sharing with IRIS/PASSCAL and the scientific community. IRIS/PASSCAL workflows are employed for this conversion (https://www.passcal.nmt.edu/content/data-archiving).

Data is recorded at 200 samples/second/channel. This gives a Nyquist frequency of 100 Hz which has proven sufficient for monitoring local earthquakes at Wellington field (Figure 5.3). Local seismicity can have frequencies nearing or just exceeding 100 Hz (Bormann, 2012), but 200 SPS is a good balance between data quality and telemetry bandwidth availability.

For data processing, an STA/LTA network trigger in obspy, a library for Python, is used (Beyreuther *et al.*, 2010). A high pass filter over 10 Hz is used in a coincidence STA/LTA trigger to detect local earthquakes and eliminate noise sources in a lower frequency, often pump jacks, cars, trains, and other field noise. The script produces a file of 90 seconds around the trigger. Trigger files are then evaluated for earthquakes and if there is an earthquake, it is manually located in SeisAn (Havskov and Ottemoller, 1999).

Due to the isolation of the Patterson site, as well as its distance from network maintainers, telemetric data transfer was chosen over manual recovery. Manual recovery would be suitable for closer field sites. Data needs to be recovered from manual sites at least every two months with the current set up of 200 samples per second per channel on three-component stations.

5.5 Results

At the Patterson and Hartland fields, monitoring station locations were limited to 8 to install over a large area measuring 13x5 km and 8x5 km, with the project area of interest being the region covered by two 3D seismic surveys (Figures 5.1 and 5.5). This network design shows a minimum magnitude that can be located in the field as approximately M_w 0.5, with the full fields encompassed by a minimum locatable magnitude of M_w 0.8 (Figure 5.5). For this study, a minimum magnitude of M_w 1 in the field is the desired level of detectability.

Stations at the Patterson and Hartland Fields were installed via shallow burial, less than 0.5 m from the surface. While deep burial/borehole limits surface noise, it requires significant equipment investment as well as installation cost and time and must be balanced with budgetary considerations and monitoring objectives. Another installation tested at Wellington field employed seismometer vaults consisting of a ~2m open hole, built with corrugated steel. However, the open hole configuration is susceptible to thunder bursts as seen in Figure 3. Patterson project installations in shallow burial proved more economical, easier to deploy and less susceptible to noise from storm events.

Because the Patterson/Hartland CO_2 sequestration site is an active oil field, site noise was anticipated. Early network installation prior to the start of the monitoring period allows for additional quality analysis of station locations and movement of stations with significant noise location optimization if earthquakes occur. Data shows that noise levels are acceptable 100 meters or more from pump jacks, which can be visually identified upon arrival to the site. At the Patterson and Hartland sites only one station was affected by high noise from a nearby pump jack. However, underground pumps near oil field storage tanks can run nearly continuously and make a station completely untenable; unfortunately, pumping systems may not be well known prior to seeing them in the data, and stations may need to be moved.

5.6 Conclusions

The network designed at Patterson and Hartland fields, done according to the principles and specifications presented here (Figure 5.6), is sufficient to monitor for M1 and greater earthquakes within the vicinity of potential fluid injection operations. The network will provide accurate locations within the field, given the azimuthal gap in the field (Figure 5.5). Additionally, the number of stations within the size of the field guarantees the close proximity of at least one station for proper depth estimation.

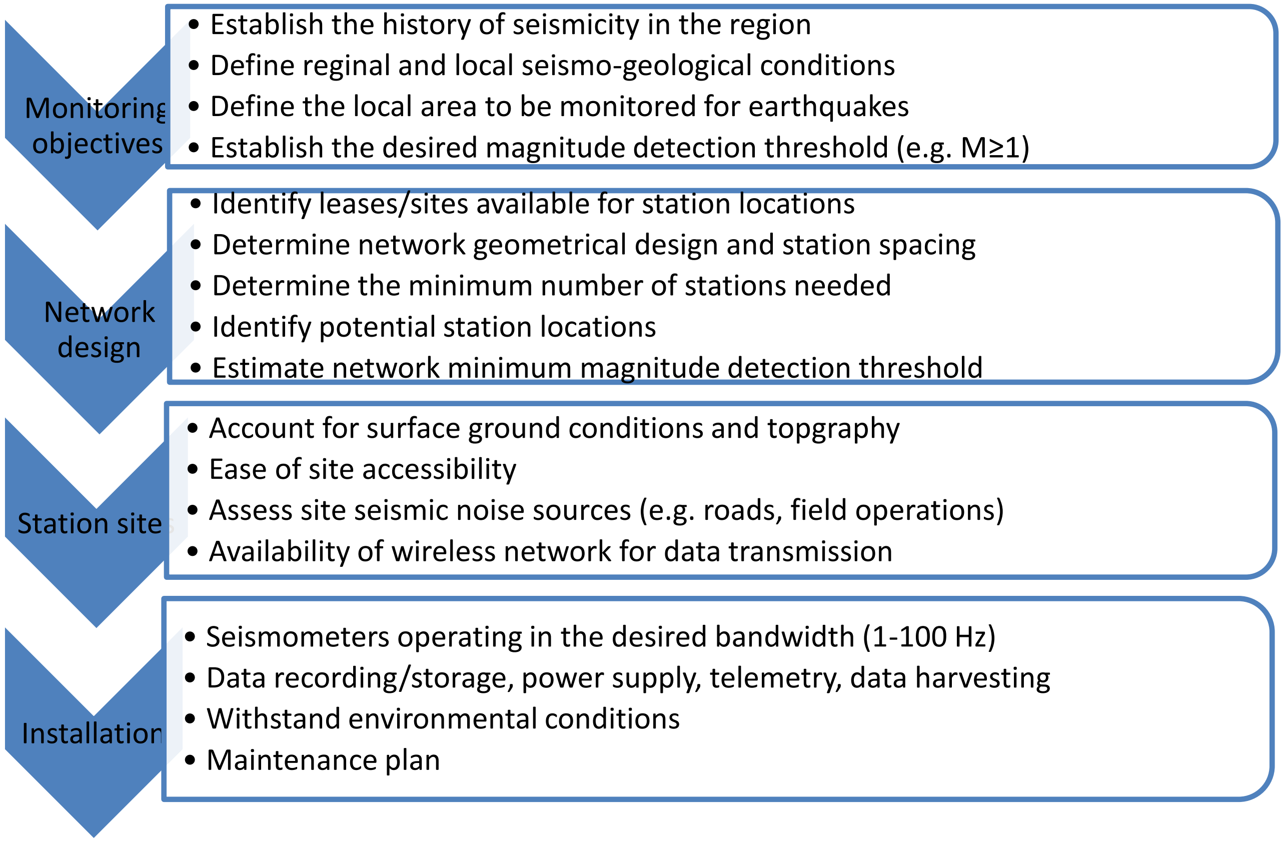

Figure 5-6: Workflow for the establishment of a rapid-deployment, temporary seismic network to monitor regions for induced seismicity near active industrial operations.

The Patterson and Hartland field network has monitored the area continuously from May 2019 until July 2020. No local seismicity has been detected which supports the project objective of evaluating sites of low earthquake risk suitable for CSS operations. The nearest earthquake detected by the monitoring network can be seen in Figure 7, showing an example of data quality from two stations. This earthquake was an M_w 2.3 approximately 100 km to the west, in Colorado. Several distant earthquakes in Colorado and Southern and Northern Kansas were detected and correlated to regional earthquakes identified by the USGS, validating that the network is working properly.

At Patterson and Hartland fields it is not feasible to define magnitude distance relationships due to the lack of local seismicity. Therefore, we use observations from an analogue monitoring network operating at the Wellington oil field in southern Kansas. The Patterson and Hartland site is exceptionally similar, seismo-geologically, to Wellington. The relationship curve derived from Wellington and applied to this study (Figure 5.4) is reasonably conservative, which are strong indicators that the results will be near the expectation. However, in more diverse site settings, the empirically derived curve may be less accurate in direct magnitude distance calculation, but can still provide insight and a helpful guideline on network design. A notable result of this work is demonstrating that local earthquake monitoring stations can be placed near oil and gas production facilities without severely limiting local seismic detection thresholds. Shallow buried seismometers in temporary stations are able to detect local seismicity and station geometry is controlled more by the expected earthquake depth and spacing of stations to accurately calculate the depth than of attenuation of the earthquake signal. It is expected that similar networks would be installed in broadly similar geologies (sedimentary basins) so assuming a 1D velocity model is still valid. Therefore, the best fit equation presented here can still be used as a preliminary assessment for station spacing.

The Patterson / Hartland network operated reliably for fifteen months without the requirement of equipment maintenance or manual data retrieval. The methods presented here for establishing a local, short-term earthquake network proved to be effective and efficient, meeting the requirements of successfully identifying and locating M1 and greater earthquakes in the field, and can be applied to industrial sites for monitoring of induced seismicity.

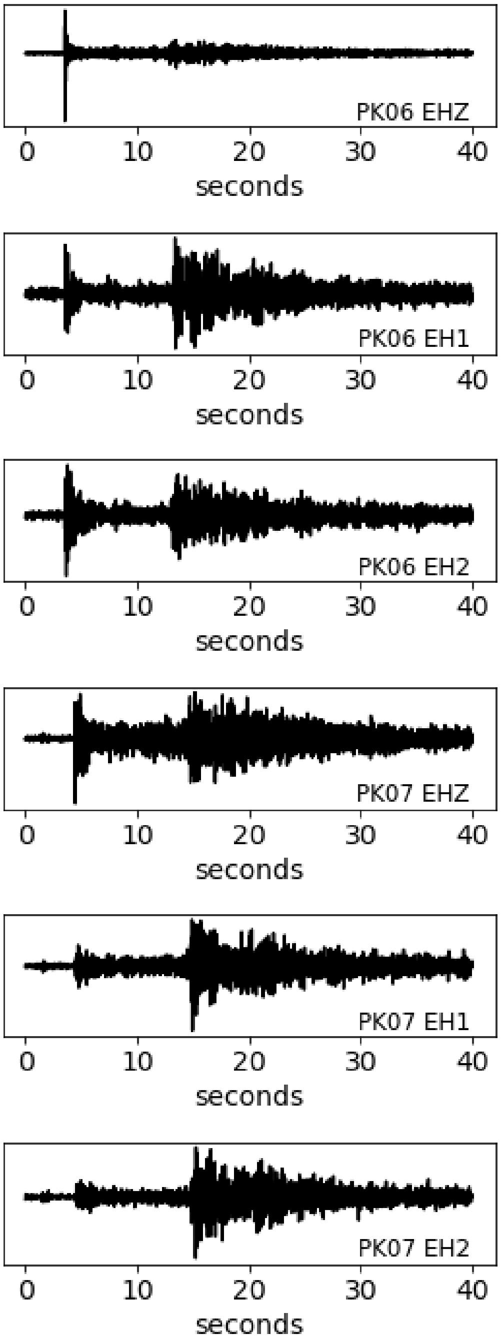

Figure 5-7: Example of an earthquake on two Patterson Network stations showing vertical (EHZ) and two horizontal components (north EH1, east EH2).

The earthquake occurred ~100 km to the west and is an M_w 2.3. P and S wave arrivals are seen clearly despite stations being located near producing facilities at an active oil field. The P arrival can be seen at ~4 seconds and the S arrival can be seen at ~14 seconds.

Chapter 6 Conclusions, Discussion, and Future Directions

6.1 Conclusions and Discussion

6.1.1 Earthquake catalog

The Wellington Oil Field Earthquake Monitoring Network collected data from 2015 to 2020. During that time period, it captured ~4,000 earthquakes in south central Kansas. These earthquakes are tied to increases in pore pressure due to fluid injections as part of oil operations in northern Oklahoma and southern Kansas. Seismicity progressively advanced to the north throughout the monitoring period. Analysis of the earthquakes including multiple re-organizations of the network allowed the identification of several previously unknown faults in this region. Earthquakes which occur on these faults have swarming behavior in which there is no clear foreshock, mainshock, aftershock sequences. In the earthquake swarms, the largest event could occur anywhere throughout the swarm which can contain 10-100s of earthquakes over a few hours to multiple days. Distant, large volume wastewater injections south and west of Wellington field peaked in 2015 with in-situ pressure monitoring at Wellington reaching maximum in October 2016 and the earthquake rate at Wellington peaking in 2017. As injection volumes decreased, due to State limits imposed the first quarter of 2015, the rate of earthquakes at Wellington decreased each year after 2017 until the end of the analysis in 2020. This timeline suggests 1.5 to 2.0 years of sustained high-rate seismicity at Wellington after curtailing distant fluid injection operations.

The Wellington Oil Field Earthquake Monitoring Network had a magnitude of completeness of 1.6 in Sumner County, indicating that the field design and analysis techniques were sufficient for industrial monitoring purposes. However, a greater number of earthquakes could delineate additional faults, improving the understanding of the regional tectonics. It is unlikely that a significant number of earthquakes will occur after 2020, given the steadily decreasing trends in earthquake numbers; unless injection volumes change, earthquake numbers are unlikely to substantially increase, although there will likely be low level seismicity in the region for the foreseeable future. Earthquake monitoring at the Wellington Network is scheduled to cease in May of 2021.

6.1.2 Network Design

As oil and gas operations expand and concern about induced seismicity increases, deploying local, temporary networks to monitor seismic activity will become more important. These networks can be successfully deployed on existing oil and gas leases despite risks of site noise. Networks can be properly designed within these constraints and still provide Mc of ~1 in the field area. Effective temporary networks can be done inexpensively and efficiently, relative to longer term monitoring installations, making them accessible.

Using the standards produced here, temporary networks can generate data with high confidence in low magnitude detection at high surface-noise sites. Generally, these networks would be sufficient to monitor any site where positive magnitudes are required to be identified. While it was expected that western Kansas would not be seismically active; we were able collect earthquake data to determine that the network was operating properly. We demonstrated that shallow burial of seismometers significantly improved signal versus installation in steel vaults, especially during storms. There are no thunder bursts detected at buried stations despite the field having significant storm and wind activity during the 15 months of monitoring. This work establishes practical guidelines for setting up temporary networks.

6.1.3 SP Wave Identification Constrains Local Earthquake Depths

SP waves were manually identified in local earthquakes in south-central Kansas. These converted waves are useful in determining earthquake depth with poor station geometry. This was of particular importance in the Wellington Oil Field where the stations were not optimally located and may continue to be important in temporary networks deployed to monitor industrial activities where ideal station geometry may not be possible.

Using this novel methodology developed herein, we proved that earthquakes did not occur in the sedimentary units in south-central Kansas, confirming that these events were limited to the shallow basement. Further, SP waves can be used to constrain the Vp/Vs ratio in the sedimentary section, reducing earthquake location uncertainty. Vp/Vs logs may not include shallow data, but SP converted waves can help to constrain analysis at this depth.

Through the Vp/Vs logs, we were able to gain insight on the impedance contrasts in the sedimentary section. We anticipated the largest impedance difference would be between the igneous granitic basement and the overlying carbonate units based on geologic intuition. However, we determined that the largest difference, which is the source of the SP conversion, is in the sedimentary section between the carbonate and sandstone units.

6.1.4 Shear Wave Anisotropy Analysis

Over five years of earthquakes were evaluated for shear wave splitting analysis. These earthquakes were subdivided into confined spatial clusters to reduce raypath differences, ensuring anisotropy results are similar in a cluster. Limiting the analysis to these clusters ensures that any potential change in anisotropy is not related to raypath effects. The S-wave split measurements are consistent with the expected sources of anisotropy in southern Kansas. However, there are temporal changes in which source of anisotropy a cluster aligns with, indicating changes in the shallow basement.

Pore pressure changes likely cause S-wave anisotropy observations to change alignment between the existing sources of anisotropy. Full flips appear harder to identify in these very local earthquakes as opposed to Nolte et al., (2017) but clear rotations are evident.

In south-central Kansas, shear-wave orientations align with preexisting fault structures and the maximum horizontal stress of the region. From 2015 to 2020 there are clear temporal changes in S-wave anisotropy that occur during a period of increased pore pressure in the shallow basement due to high-rate injections in the region.

This work developed a new code based on multiple existing methods that can improve shear wave anisotropy analysis methods. Previously, there were no codes to access Seisan databases, used extensively in the seismological community; here we devised methods to directly access Seisan databases and process that data through automated means, reducing human work time and improving efficiency.

Cycle skipping, in which automated methods misidentify wave peaks by a half cycle of the dominant shear-wave frequency, was a significant confounder in these studies. Cycle skipping can cause delay times to be less stable than the ϕ orientation, which is unchanged when a cycle skip occurs. Manual methods can avoid this problem, but bring another slate of issues, namely the inability to process large data sets. If cycle skipping could be reduced, delay times could be stabilized.

The complexity of the anisotropy caused by the structures in the field compounded with very small pressure chances create challenges in interpreting the data and understanding the source of anisotropic changes. Using an inversion to help delineate the effects would likely be similarly confounded by interfering effects of sources of anisotropy. More could be done to study shear wave anisotropy in other regions where multiple sources of anisotropy are of similar magnitude.

6.2 Future Directions for Local Earthquake Monitoring

At present and for the coming decades, until alternative energy resources become sufficient to meet societal needs, Carbon Capture Utilization and Storage (CCUS) is a viable option for industrial level sequestration of CO_2 and its removal from the atmosphere. The need to monitor CCUS sites will likely increase as more sites are identified and the technology is adapted. Future cost savings and operational efficiency could be achieved by adopting a more commercial approach and purchasing seismometers versus utilizing NSF funded equipment on loan. Although IRIS/PASSCAL equipment is free to have access to by academic and research institutions, data limitations and management add significant overhead and time to the process. Furthermore, the IRIS/PASSCAL instrument pool may not be sufficient to support multiple local networks. A more direct method for future studies could be using a system like the RaspberryShake, which is capable of detecting similarly sized earthquakes but is purchasable at a much lower price point with better data options than IRIS/PASSCAL equipment. The ability to stream data directly to a server in a conventional seismic format would eliminate the need for preprocessing and allow for streamlined automated techniques without deep computer engineering knowledge. The ownership of the equipment also eliminates cost of shipping and handling of borrowed equipment. These cost savings are not much less than the cost of purchasing this equipment outright. Other costs are unchanged given the borrowed equipment required purchase of telemetry equipment as well. Although this equipment lacks some sensitivity as compared to higher end monitoring devices, its sensitivities would not detract from identification of earthquakes in the magnitude ranges of interest for this study. Incorporating alternative instrumentation resources to the workflow presented in chapter 5 can facilitate future local seismic network design and installation operations.

Accurate earthquake location is important for assessing earthquake hazards, especially in local events when location errors of a few km can occur due to network design limitations. SP wave identification in local earthquakes and the method presented in this dissertation could be used to update shear wave velocities in the sedimentary section and allow for an independent S-wave velocity model, as opposed to the 1D velocity model with a fixed Vp/Vs ratio commonly used. Adjusted velocities would provide more accurate earthquake locations. Additionally, the depths provided in the SP calculation could be utilized to update the catalog depth statistics. The depths could also be fixed in the HypoInverse epicenter calculation, providing a more stable location in x and y as well. However, this process would have to be done iteratively, given the updated location would have to have a new depth calculated from it, since the depth calculation is dependent on the epicenter location. A minimization technique could be used here to better constrain both epicenter location and depth. The depth technique could also be tested against earthquakes with better locations due to station geometry. This would require moving stations to within a few kilometers of the field in other directions, to ensure the HypoInverse depth calculation is properly constrained by just P and S wave arrivals. This calculation could then be compared against the SP calculation, with the expectation being the two are very similar.

This dissertation tested the idea that S-wave splits in induced earthquakes are sensitive to wastewater injection-induced pore pressure changes. Observations herein are consistent, but data is limited to the natural environment. In the future, studies like this should be conducted in areas where earthquake and in-situ pressure data are available for further validation of the work. Conducting these studies under more controlled conditions could provide the necessary means to remotely monitor subsurface pore pressure and mitigate the risk of induced seismicity near industrial sites.

Chapter 7 References

Alt, R. C., II, and Zoback, M.D. (2017), In situ stress and active faulting in Oklahoma. Bulletin of the Seismological Society of America, 107(1), doi:10.1785/0120160156

Anderson, E. M. (1951). The dynamics of faulting and dyke formation with applications to Britain. Houston, TX: Hafner Pub. Co.

Angerer, E., Crampin, S., Xiang-Yang, L., Thomas, D.L., 2002, Processing, modeling and predicting time-lapse effects of overpressured fluid-injection in a fractured reservoir: Geophysical Journal International, **149**, 268-281.

Anno, P.D., 1986, Two critical aspects of shear-wave analysis: Statics solutions and reflection correlations, in Danbom, S.H., and Domenico, S.N., Eds., Shear-wave exploration: Society of Exploration Geophysicists., Geophys, Dev. Series, 1, 48-61.

Baars, D.L. (1995), Basement Tectonic Configuration in Kansas. Kansas Geological Survey, 237.

Baars, D.L., and Watney, WL (1991), Paleotectonic control of reservoir facies. Kansas Geological Survey, 233, 253-262.

Bailey, D.L., Miller, R.D., Peterie, S., Ivanov, J., Steeples, D., Markiewicz, R., (2013). Implications of Vp/Vs ratio on shallow P and S reflection correlation and lithology discrimination. Society of Exploration Geophysicists Annual Meeting extended abstract.

Bao, X. and Eaton, D.W., (2016), Fault activation by hydraulic fracturing in western Canada. Science, 354, 6318, 1406-1409.

Beyreuther, Moritz, Robert Barsch, Lion Krischer, Tobias Megies, Yannik Behr, and Joachim Wassermann. 2010. 'ObsPy: A Python toolbox for seismology', *Seismological Research Letters*, 81: 530-33.

Bokelmann, G. and Harjes, H.P., 2000, Evidence for temporal variation of seismic velocity within the upper continental crust: Journal of Geophysical Research, **105**, 23879-23894.

Bondar, I., Myers, S.C., Engdahl, E.R., and Bergman, E.A. (2004) Epicentre accuracy based on seismic network criteria. *Geophysics Journal International*. 156. 483-496.

Boness N.L., and Zoback M.D., 2006, A multiscale study of the mechanisms controlling shear velocity anisotropy in the San Andreas Fault Observatory at Depth: Geophysics, 71, 5, F131-F146.

Bormann, P., (2012). Seismic Networks, Chapter 8 of the IASPEI New Manual of Seismological Observatory Practice 2(NMSOP-2)

Brune, J., (1970), Tectonic Stress and the Spectra of Seismic Shear Waves from Earthquakes. Journal of Geophysical Research, 75, 4997-5009.

Carr, J. E., H. E. McGovern, and T. Gogel (1986). Geohydrology of and potential for fluid disposal in the Arbuckle aquifer in Kansas, U.S. Geol. Surv. Open-File Rept. 86-491.

Cary, P.W., Eaton, D.W.S., (1993). A simple method for resolving large converted-wave (P-SV) statics. Geophysics. 58, 3, 429-433.

Cesca, Simone, Thomas Braun, Francesco Maccaferri, Luigi Passarelli, Eleonora Rivalta, and Torsten Dahm. 2013. 'Source modelling of the M 5–6 Emilia-Romagna, Italy, earthquakes (2012 May 20–29)', *Geophysical Journal International*, 193: 1658-72.

Cesca, Simone, and Francesco Grigoli. 2015. 'Full waveform seismological advances for microseismic monitoring.' in, *Advances in Geophysics* (Elsevier).

Cesca, Simone, Francesco Grigoli, Sebastian Heimann, Alvaro González, Elisa Buforn, Samira Maghsoudi, Estefania Blanch, and Torsten %J Geophysical Journal International Dahm.

2014. 'The 2013 September–October seismic sequence offshore Spain: a case of seismicity triggered by gas injection?', 198: 941-53.

Chatelain, J. L., S. W. Roecker, D. Hatzfeld, and P. Molnar (1980). Microearthquake seismicity and fault plane solutions in the Hindu Kush region and their tectonic implications, *Journal of Geophysics Research.* 85, 1365-1387.

Choi, Hyunyoung, and Hal %J Economic Record Varian. 2012. 'Predicting the present with Google Trends', 88: 2-9.

Choy, George L, Justin L Rubinstein, William L Yeck, Daniel E McNamara, Charles S Mueller, and Oliver S Boyd. 2016. 'A rare moderate-sized (M w 4.9) earthquake in Kansas: Rupture process of the Milan, Kansas, earthquake of 12 November 2014 and its relationship to fluid injection', *Seismological Research Letters*, 87: 1433-41.

Crampin, C., Volti, T., Chastin, S., Gudmundsson, A. and Stefánsson, R., 2002, Indication of high pore-fluid pressures in a seismically-active fault zone: Geophysical Journal International, **151**, 2, pp. F1-F5.

Crampin, S. Peacock, S., Gao, Y., Chastin, S., 2004, The Scatter of time-delays in shear-wave splitting above small earthquakes: Geophysics Journal International, **156**, 39-44.

Crampin, S., 1985, Evaluation of anisotropy by shear-wave splitting: Geophysics, **50**, 142-152.

Dahm, Torsten, Dirk Becker, Monika Bischoff, Simone Cesca, Bernhard Dost, Ralf Fritschen, Sebastian Hainzl, Christian D Klose, Daniela Kühn, and Stanislaw Lasocki. 2013. 'Recommendation for the discrimination of human-related and natural seismicity', *Journal of seismology*, 17: 197-202.

Dahm, Torsten, Simone Cesca, Sebastian Hainzl, Thomas Braun, and Frank %J Journal of Geophysical Research: Solid Earth Krüger. 2015. 'Discrimination between induced, triggered, and natural earthquakes close to hydrocarbon reservoirs: A probabilistic approach based on the modeling of depletion-induced stress changes and seismological source parameters', 120: 2491-509.

Dempsey, D. and Riffault, J., 2019, Response of induced seismicity to injection rate reduction: Models of delay, decay, quiescence, recovery and Oklahoma: Water Resources Research, **55**.

DuBois, S.M., and Wilson, F.W., (1978). A revised and augmented list of earthquake intensities of Kansas, 1867-1977, Kansas Geological Survey, Environmental Geology Series 2.

Ellsworth, William L J Science. 2013. 'Injection-induced earthquakes', 341: 1225942.

Ellsworth, W.L., Llenos, A.L., McGarr, A.F., Michael, A.J., Rubinstein, J.L., Mueller, C.S., Peterson, M.D., Calais, E. (2015). Increasing seismicity in the U.S. midcontinent: implications for earthquake hazard. The Leading Edge, 34, 618-626.

EPA Office of Water, Geologic Sequestration of Carbon Dioxide, Underground Injection Control Program class VI Implementation Manual for UIC Program Directors. pg 64

Evans, C., and K. Newell (2013). The Mississippian Limestone Play in Kansas: Oil and gas in a complex geologic setting, Kansas Geol. Surv. Public Inf. Circ. 33, 1–6.

Evans, D.G., and Steeples, D.W., (1987). Microearthquakes near the Sleepy Hollow Oil Field, Southwestern Nebraska. Bulletin of the Seismological Society of America, 77, 1, 132-140.

Evans, D.M., (1966). The Denver Area Earthquakes and The Rocky Mountain Arsenal Disposal Well. *The Mountain Geologist*, v. 3.

Fadolalkarem, Y., (2015), Pre-stack Seismic Attribute Analysis of the Mississippian Chert and the Arbuckle Group at the Wellington Field, South-Central Kansas. The University of Kansas, Department of Geology, MS Thesis.

Foulger, Gillian R, Miles P Wilson, Jon G Gluyas, Bruce R Julian, and Richard J %J Earth-Science Reviews Davies. 2018. 'Global review of human-induced earthquakes', 178: 438-514.

Franseen, Evan K, Alan P Brynes, Jason R Cansler, Mark D Steinhauff, and Timothy R %J Midcontinent Geoscience Carr. 2004. 'The geology of Kansas Arbuckle Group': 1-43.

Frohlich, C., (2012), Two-year survey comparing earthquake activity and injection-well locations in the Barnett Shale, Texas. Proceedings of the National Academy of Sciences of the United States of America. 109, 35. 13934-13938.

Gao, Y. and Crampin, S., 2004. Observations of stress relaxation before earthquakes: *Geophysical Journal International*, ***157***, 2, pp.578-582.

Garnero, E., 2017 http://garnero.asu.edu/research_images/images_all.html

Gomberg, J.S., Shedlock, K.M., Roecker, S.W., (1990). The effect of s-wave arrival times on the accuracy of hypocenter estimation. Bulletin of the Seismological Society of America. 80, 6, 1605-1628.

Grigoli, Francesco, Simone Cesca, Enrico Priolo, Antonio Pio Rinaldi, John F Clinton, Tony A Stabile, Bernard Dost, Mariano Garcia Fernandez, Stefan Wiemer, and Torsten Dahm. 2017. 'Current challenges in monitoring, discrimination, and management of induced seismicity related to underground industrial activities: A European perspective', *Reviews of Geophysics*, 55: 310-40.

Harbaugh, JW. 1959. 'Marine bank development in Plattsburg Limestone (pennsylvanian), Neodesha-Fredonia area, Kansas', *Kansas Geological Survey Bulletin*, 134: 291-331.

Havskov, J., and L. Ottemoller. 1999. 'SeisAn Earthquake analysis software', *Seismological Research Letters*, 70.

Herzog, H.J., (2011). Scaling up Carbon Dioxide Capture and Storage: From Megatons to Gigatons, *Energy Economics*, v. 33, is. 4, p. 597-604.

Hildebrand, G.M., Steeples, D.W., Knapp, R.W., Miller, R.D. and Bennett B.C. (1988). Micro-earthquakes in Kansas and Nebraska 1977–87. Seismological Research Letters, 59(4), 159-163. http://www.dx.doi.org/10.1785/gssrl.59.4.159.

Hilpman, PL %J Survey Oil, and Gas Inves. 1958. 'Producing zones of Kansas oil and gas fields: Kansas Geol', 16: 1-10.

Holubnyak, Yevhen, Lynn Watney, Jennifer Hollenbach, Tiraz Birdie, Drew R. Schwab, Keith A Nolte, George P Tsoflias, John Victorine, Brandon Graham, John Doveton, Jason Bruns, Brett Blazer, and Dana Wreath. 2017. 'Small scale field test demonstrating CO2 sequestation in Arbuckle saline aquifer and by CO2 or at Wellington field, Sumner County, Kansas'.

Holubnyak, E., Dubois, M., Bidgoli, T., Hollenbach, J., Wreath, D., Watney, L., Stover, S., Newell, D., Fazelalavi, F., Hollenbach, A., Jennings, J., Steincamp, C., Schremmer, J., Jordan, B., Crabtree, B., Christensen, J., McFarlane, D., Doveton, J., Krishnamurthy, K., Byron, M., and Watts, K.. Integrated CCS for Kansas (ICKan) Final Technical Report. United States: N. p., 2018. Web. doi:10.2172/1491482.

Holubnyak, Y., Dubois, M., Birdie, T., and Hollenbach, J., Selecting CO2 sinks CCUS Deployment in South Mid-West USA, *Gas Injection into Geological Formations and Related Topics*, 2020, DOI: 10.1002/9781119593324.ch10

Hornbach, Matthew J, Heather R DeShon, William L Ellsworth, Brian W Stump, Chris Hayward, Cliff Frohlich, Harrison R Oldham, Jon E Olson, M Beatrice Magnani, and Casey %J

Nature communications Brokaw. 2015. 'Causal factors for seismicity near Azle, Texas', 6: 6728.

Jewett, John M, and Daniel F Merriam. 1959. "Geologic framework of Kansas; a review for geophysicists." In *Symposium on geophysics in Kansas: Kansas Geological Survey Bulletin*, 9-52.

Joyner WB, Boore DM (1981) Peak horizontal acceleration and velocity from strong-motion records including records from the 1979 Imperial Valley, California, earthquake. *Bulletin Seismological Soceity of America.* 71:2011–2038

Kalami Heris, S.M., (2015), Implementation of DBSCAN Clustering in MatLab. Yarpiz, www.yarpiz.com

Keranen, Katie M, Heather M Savage, Geoffrey A Abers, and Elizabeth S Cochran. 2013. 'Potentially induced earthquakes in Oklahoma, USA: Links between wastewater injection and the 2011 Mw 5.7 earthquake sequence', *Geology*, 41: 699-702.

Keranen, Katie M, Matthew Weingarten, Geoffrey A Abers, Barbara A Bekins, and Shemin %J Science Ge. 2014. 'Sharp increase in central Oklahoma seismicity since 2008 induced by massive wastewater injection', 345: 448-51.

Keranen, K.M., Savage, H.M., Abers, G.A., Cochran, E.S., 2013, Potentially induced earthquakes in Oklahoma, USA: links between wastewater injection and the 2011 Mw 5.7 earthquake sequence: Geology, **41**, 699-702.

Kim, W.Y, (2013) Induced Seismicity associated with fluid injection into a deep well in Youngstown, Ohio, *Journal of Geophysical Reseach: Solid Ear*th, v. 118, p. 3506-3518.

Klein, F.W. (2007). User’s guide to HYPOINVERSE-2000, a Fortran program to solve for earthquake locations and magnitudes, U.S. Geological Survey. Open file report, 02-171.

Klein, FW. 2002. 'User's Guide to HYPOINERSE-2000, a Fortran Program to Solve for Earthquake Locationsa nd Magnitudes', *US Geological Survey Open-File Report 02-171*, 123.

Kraft, T., Mignan A., Giardini, D., (2013). Optimization of a large-scale microseismic monitoring network in northern Switzerland. *Geophyiscal Journal International*. 195, 1, 474-490.

Langenbruch, Cornelius, Matthew Weingarten, and Mark D Zoback. 2018. 'Physics-based forecasting of man-made earthquake hazards in Oklahoma and Kansas', *Nat Commun*, 9: 1-10.

Langenbruch, Cornelius, and Mark D %J Science advances Zoback. 2016. 'How will induced seismicity in Oklahoma respond to decreased saltwater injection rates?', 2: e1601542.

Leatherock, Constance. 1945. 'The correlation of rocks of Simpson age in north-central Kansas with the St. Peter sandstone and associated rocks in northwestern Missouri', *Kansas Geological Survey*, 60.

Lee, Wallace. 1940. 'Subsurface Missippian Rocks of Kansas', *Kansas Geological Survey, Geology*.

Lee, Wallace, and DF Merriam. 1954. 'Cross Sections in eastern Kansas', *Kansas Geological Survey, Oil and Gas Inventory*, 12: 1-8.

Li, T., Gu, Y. J., Wang, Z., Wang, R., Chen, Y., Song, T.-R. A., & Wang, R., 2019, Spatiotemporal variations in crustal seismic anisotropy surrounding induced earthquakes near Fox Creek, Alberta: *Geophysical Research Letters*, 46, 5180– 5189.

Liu, K.S., and Tsai, Y.B., (2005). Attenuation Relationships of Peak Ground Acceleration and Velocity for Crustal Earthquakes in Taiwan. *Bulletin of the Seismological Society of America* ; 95 (3): 1045–1058. doi: https://doi.org/10.1785/0120040162.

MATLAB 2018a, The MathWorks, Inc., Natick, Massachusetts, United States.

Margrave, G.F., (2003) Numerical Methods of Exploration Seismology with algorithms in Matlab

Maxwell, S.C., Rutledge, J, Fehler, M., (2010). Petroleum Reservoir Characterization using downhole microseismic monitoring. *Geophysics*. 75, 5.

McGarr, A, David Simpson, L Seeber, and William %J International Geophysics Series Lee. 2002. 'Case histories of induced and triggered seismicity', 81: 647-64.

McNamara, D.E. and Buland, R.P., (2004) Ambient Noise Levels in the Continental United States. *Bulletin of the Seismological Society of America*. V. 94, no. 4, p. 1517-1527.

Merriam, D. F. (1956). History of earthquakes in Kansas. Bulletin of the Seismological Society of America, 46(2), 87–96.

Merriam, D. F. (1963). The geologic history of Kansas, State Geological Survey of Kansas Bulletin, (Vol. 162, p. 317). Lawrence, KS: University of Kansas.

Merriam, Daniel Francis %J Kansas Geological Survey Bulletin. 1954. 'Electrical Resistivity Studies in the Kansas River Valley': 97-112.

Moore, Raymond Cecil. 1949. *Divisions of the Pennsylvanian system in Kansas* (University of Kansas publications).

———. 1951. *The Kansas rock column* (University of Kansas Publications).

Moore, RC. 1929. 'Environment oof Pennsylvanian life in North America', *American Association of Petroleum Geologists Bulletin*, 13: 459-87.

Nixon, Earl K, Russell T Runnels, and Robert O Kulstad. 1950. *The Cheyenne Sandstone of Barber, Comanche, and Kiowa Counties, Kansas, as Raw Material for Glass Manufacture* (University of Kansas Publications).

Nolte, Keith A, George P Tsoflias, Tandis S Bidgoli, and W Lynn %J Science advances Watney. 2017. 'Shear-wave anisotropy reveals pore fluid pressure–induced seismicity in the US midcontinent', 3: e1700443.

Nolte, K.A., (2017), *Monitoring induced seismicity near the Wellington oil field, south-central Kansas.* The University of Kansas, MS thesis.

Nolte, K.A. and Tsoflias, G.P., (2019). Monitoring seismicity near a CO_2 enhanced oil recovery and sequestration site, American Association of Petroleum Geologists Midcontinent Session, Wichita, KS, October 7-9, 2019.

Nolte, K.A. and Tsoflias, G.P., (2020) Identifying direct SP converted waves constrain local induced earthquake depths, Seismological Research Letters, *in review*.

Nolte, K.A., and Tsoflias, G.P., (2019) Monitoring seismicity near a CO_2 enhanced oil recovery and sequestration site, *American Association of Petroleum Geologists Midcontinent Session Meeting*, Wichita, KS.

Parkhurst, RW. 1959. 'Surface to subsurface correlations and oil entrapment in the Lansing and Kansas City Groups (Pennsylvanian) in northwestern Kansas', *MS Thesis University of Kasnas*.

Peterie, S. L., Miller, R. D., Intfen, J. W., & Gonzales, J. B. (2018). Earthquakes in Kansas induced by extremely far-field pressure diffusion. Geophysical Research Letters, 45, 1395–1401. https://doi.org/ 10.1002/2017GL076334

Plummer, Norman Vincen, and John F Romary. 1947. *Kansas clay, Dakota Formation* (State Geological Survey).

Pratt, Wallace E, and Douglas W %J The Journal of Geology Johnson. 1926. 'Local subsidence of the Goose Creek oil field', 34: 577-90.

Rubinstein, JL, WL Ellsworth, and SL Dougherty. 2018a. 'The 2013-201 Induced Earthquakes in Harper and Sumner Counties, Southern Kansas', *Bulletin of the Seismological Society of America*, 108.

Rubinstein, Justin L, William L Ellsworth, and Sara L Dougherty. 2018b. 'The 2013–2016 Induced Earthquakes in Harper and Sumner Counties, Southern KansasThe 2013–2016 Induced Earthquakes in Harper and Sumner Counties, Southern Kansas', *Bulletin of the Seismological Society of America*, 108: 674-89.

Rubinstein, J. L., and A. B. Mahani (2015). Myths and facts on wastewater injection, hydraulic fracturing, enhanced oil recovery, and induced seismicity, Seismol. Res. Lett. 86, no. 4, 1060–1067, doi: 10.1785/0220150067.

Runnels, Russell T, and Ira M %J Kansas Geological Survey Bulletin Dubins. 1949. 'Chemical and petrographic studies of the Fort Hays Chalk in Kansas', 82: 1-36.

Runnels, Russell T, Robert O Kulstad, Clinton McDuffee, and John A Schleicher. 1952. *Oil shale in Kansas* (University of Kansas Publications).

Rutqvist, J., (2012). The Geomechanics of CO2 Storage in Deep Sedimentary Formations, *Geotechnical and Geological Engineering, 30, 525-551.*

Savage, H.K., (1999). Seismic Anisotropy and Mantle Deformation: What have we learned from shear-wave splitting? *Reviews of Geophysics*, 37,1.

Savage, M.K., Wessel, A., Teanby, N.A., Hurst, A.W., 2010, Automatic measurement of shear-wave splitting and applications to time varying anisotropy at Mount Ruapehu volcano, New Zealand: Journal of Geophysical Research, **115**.

Sawin, Liz Brosius and Robert S. 2001. 'Lead and Zinc Mining in Kansas', Kansas Geological Survey, Public Outreach. http://www.kgs.ku.edu/Publications/pic17/pic17_1.html.

Schoenball, M. and Ellsworth, W.L., (2017), Waveform-Relocated Earthquake Catalog for Oklahoma and Southern Kansas illuminates the Regional Fault Network, Seismological Research Letters, 88, 5, 1252-1258.

Schwab, D.R., Bidgoli, T.S., and Taylor, M.L., (2017), Characterizing the Potential for Injection-Induced Fault Reactivation through Subsurface Structural Mapping and Stress Field Analysis, Wellington Field, Sumner County, Kansas, Journal of Geophysical Research: Solid Earth, 122, 12.

Silver, P.G., Chan, W.W., 1991, Shear wave splitting and subcontinental mantle deformation: Journal of Geophysical Research, **96**, 16429-16454.

Skoumal, Robert J, Michael R Brudzinski, and Brian S Currie. 2015. 'Distinguishing induced seismicity from natural seismicity in Ohio: Demonstrating the utility of waveform template matching', *Journal of Geophysical Research: Solid Earth*, 120: 6284-96.

Walter H Schoewe. 1952. *Coal resources of the Cretaceous system (Dakota formation) in central Kansas*.Kansas Geologic Survey.

Teanby, N.A., Kendall, J.M., van der Baan, M., 2004, Automation of shear-wave splitting measurements using cluster analysis: Bulletin of the Seismological Society of America, **94**, 453-463.

Tiira, T., Uski, M., and Kortstrom, J., (2016). Local seismic network for monitoring of a potential nuclear power plant area. *Journal of Seismology*. 20(2):397-417.

Umino N., Hasegawa, A., Matsuzawa, T., (1995). sP depth phase at small epicentral distances and estimated subducting plate boundary. Geophysics Journal International. 120, 356-366.

Waldhauser, F., 2001, hypoDD—A Program to Compute Double-Difference Hypocenter Locations: US Geological Survey Open-File Report 01-113, 25 pp., https://pubs.usgs.gov/of/2001/0113/.

Walsh, F. R. I., and M. D. Zoback (2015). Oklahoma’s recent earthquakes and saltwater disposal, Sci. Adv. 1, e1500195, doi: 10.1126/sciadv.1500195.

Walters, R. F. (1953). Oil production from fractured pre-Cambrian basement rocks in central Kansas, AAPG Bulletin 37, no. 2, 300–313.

Walters, R. F. (1958). Differential entrapment of oil and gas in Arbuckle Dolomite in central Kansas, AAPG Bulletin 42, no. 9, 2133–2173.

Warpinski, N., (2009). Microseismic Monitoring: inside and out. *Journal of Petroleum Technology*. 61, 11.

Watney, W. L. *et al.*, 2015, Modeling CO_2 sequestration in saline aquifer and depleted oil reservoir to evaluate regional CO_2 sequestration potential of Ozark Plateau aquifer system, south-central Kansas, final report, Award Number: DE-FE0002056, submitted October 2, 2015, 4,867 p.

Watney, W.L., (2014). Wellington, Kansas CO2 Sequestration Monitoring. *International Federation of Digital Seismograph Networks*. https://doi.org/10.7914/SN/ZA_2014

Watney, Lynn. 1980. 'Cyclic Sedimentation of the Lansing-Kansas City Groups in Northwestern Kansas and Southwestern Nebreaska: A Guide for Petroleum Exploration', *Kansas Geological Survey*, 220.

Wendel, J %J Eos. 2016. 'It’s not just fracking: New database of human-induced quakes', 97.

Whitmeyer, Steven J, and Karl E Karlstrom. 2007. 'Tectonic model for the Proterozoic growth of North America', *Geosphere*, 3: 220-59.

Withers, Mitchell, Richard Aster, Christopher Young, Judy Beiriger, Mark Harris, Susan Moore, and Julian Trujillo. 1998. 'A comparison of select trigger algorithms for automated global seismic phase and event detection', *Bulletin of the Seismological Society of America*, 88: 95-106.